Towards time-independent electrical impedance tomography reconstruction

Von der Fakultät für Elektrotechnik und Informationstechnik der Rheinisch-Westfälischen Technischen Hochschule Aachen zur Erlangung des akademischen Grades eines Doktors der Ingenieurwissenschaften genehmigte Dissertation

vorgelegt von Jöran Rixen, M.Sc., M.Sc. aus Kiel, Deutschland

Berichtende: Univ.-Prof. Dr.-Ing. Dr. med. Dr. h.c. Steffen Leonhardt
Prof. Dr.-Ing. habil. Uwe Pliquett
Univ.-Prof. Dr.-Ing. Anke Schmeink

Tag der mündlichen Prüfung: 10.12.2025

Diese Dissertation ist auf den Internetseiten der Universitätsbibliothek online verfügbar.

I acknowledge that some sections of this thesis were refined using language processing tools, including but not limited to ChatGPT, Gemini, Sonnet and DeepL Write. These tools were used to help with paraphrasing and improving the language, while ensuring academic integrity and adherence to the research objectives. All AI-generated content has been critically reviewed, edited and verified to ensure it remains accurate, relevant and original within the scope of this work.

What is essential is invisible to the eye.

Antoine de Saint-Exupéry, The Little Prince

Acknowledgment

I would like to express my sincere gratitude to all those who have supported me throughout the journey of completing this thesis. First and foremost, I extend my heartfelt thanks to my supervisor, Professor Leonhardt, for his invaluable guidance and unwavering support. I am particularly indebted to Daniel Voss, whose insightful thoughts, inspiration, and constructive critique have significantly shaped my work.

The positive and productive atmosphere in the office, created by Simon Lyra and Florian Voss, has been a constant source of motivation. I am also grateful to Benedikt Eliasson for our fruitful discussions during his thesis, which led to remarkable results. My appreciation extends to Chuong Ngo for sharing his experiences and offering steadfast support throughout this process.

I would be remiss not to acknowledge the crucial administrative support provided by Bettina Clever-Offermans and Daniele Glöckner, whose assistance with equipment procurement and navigation of research project formalities has been indispensable. On a personal note, I am deeply thankful to my family for their multifaceted support that has sustained me throughout this journey. A special mention goes to my brother Lennart, whose enlightening discussions have broadened my perspectives and contributed to the depth of my work.

To all my friends and colleagues who have offered encouragement and support, I extend my sincere appreciation. Your collective contributions have been instrumental in the successful completion of this thesis, and I am profoundly grateful for each one of you.

Finally, I want to thank Benjamin Hentze for encouraging me to pursue this path during my master's thesis under his supervision.

Düsseldorf, 14.06.2025

Jöran Rixen

Abstract

Motivation, Goal and Task

Motivation: Electrical Impedance Tomography (EIT) is a non-invasive imaging technique with significant potential in medical diagnostics (e.g., lung monitoring, cancer detection) and industrial applications. However, its clinical adoption remains limited due to three critical challenges inherent to time-independent reconstruction: (1) the ill-posed inverse problem amplifies small measurement errors into severe artifacts, (2) hardware imperfections and modeling inaccuracies degrade robustness, and (3) existing algorithms like Gauss-Newton and D-Bar suffer from computational inefficiency, instability in real-world conditions, or lack of generalizability. Traditional neural network approaches often require calibration data or fail to handle diverse conductivity distributions. This work addresses these gaps by advancing reconstruction quality, computational efficiency, and noise resilience for absolute and frequency-differential EIT.

Goal: The dissertation pursues two complementary approaches to improve time-independent EIT:

Artificial Neural Network (ANN): Design a rotation-invariant architecture to directly map boundary voltages to conductivity distributions, prioritizing noise robustness and generalizability across diverse scenarios.

D-Bar Algorithm: Refine this direct method for absolute and frequency-differential reconstructions while addressing practical limitations like contact impedance, non-circular domains, and limited spatial resolution through radar data fusion.

Task: The work develops two approaches: a rotation-invariant ANN trained on FEM simulations and tank data for direct voltage-to-conductivity mapping, and an enhanced D-Bar algorithm for practically available measurement devices. Validation focuses on synthetic FEM datasets and experimental tank measurements with conductive targets.

Major Scientific Contributions

ANN: The proposed ANN architecture establishes new capabilities in absolute EIT reconstruction through three fundamental innovations. First, the network's rotation-invariant design inherently handles arbitrary domain orientations through weight sharing and electrode position encoding, eliminating the need for explicit coordinate transformations. Second, training exclusively on synthetic datasets generated through Finite Element Method simulations demonstrates generalizability to real-world laboratory and animal data. Third, the architecture constitutes the first successful application of neural networks

to time-independent absolute EIT reconstruction, validated through systematic experiments on tank phantoms with conductive targets and porcine trial datasets showing physiologically plausible conductivity discrimination between major organs.

D-Bar: This work advances practical implementation of the D-Bar method through two key contributions. The first develops a complete operational pipeline within the open-source EIDORS framework. This implementation demonstrates robust experimental performance through comprehensive tank phantom verification with multiple conductive targets. The second introduces a novel pre-processing methodology enabling absolute reconstructions from pure four-electrode measurements – a critical advancement for real world applications. The modified algorithm maintains compatibility with frequency-differential and absolute EIT operation while addressing historical limitations in handling contact impedance variations. Together, these developments bridge the gap between theoretical D-Bar formulations and practically deployable EIT systems.

Major Publications

1. **J. Rixen**, B. Eliasson, B. Hentze, T. Muders, C. Putensen, S. Leonhardt, and C. Ngo: "A Rotational Invariant Neural Network for Electrical Impedance Tomography Imaging without Reference Voltage: RF-REIM-NET". *Diagnostics*, 12:777, 2022.

2. **J. Rixen**, N. Blass, S. Lyra, and S. Leonhardt: "The D-Bar Algorithm Fusing Electrical Impedance Tomography with A Priori Radar Data: A Hands-On Analysis". *Algorithms*, 16:43, 2023.

3. **J. Rixen**, N. Blass, S. Lyra, and S. Leonhardt: "Comparison of Machine Learning Classifiers for the Detection of Breast Cancer in an Electrical Impedance Tomography Setup". *Algorithms*, 16:517, 2023.

4. **J. Rixen**, B. Hentze: "Neural Network to improve Electrical Impedance Tomography Reconstructions using the GREIT Algorithm". *24th International Student Conference on Electrical Engineering.* Prague, Czech Republic, 2020.

5. **J. Rixen**, B. Eliasson, S. Lyra, and S. Leonhardt: "Shape analysis of training data for neural networks in Electrical Impedance Tomography". *45th Annual International Conference of the IEEE Engineering in Medicine and Biology Society.* Sydney, Australia, 2023.

Contents

Acknowledgment v

Abstract vii

Abbreviations and symbols xiii

1 Introduction 1

2 Foundations of Electrical Impedance Tomography 7
- 2.1 Application in the medical Domain . . . 7
  - 2.1.1 General Benefit of EIT in the medical Context . . . 7
  - 2.1.2 Different Approaches of retrieving Information . . . 7
  - 2.1.3 Simulation and Measurement Patterns . . . 9
- 2.2 Bio-Impedance Fundamentals . . . 12
  - 2.2.1 Modelling electrical Systems . . . 12
  - 2.2.2 Impedance of Tissue . . . 14
  - 2.2.3 Measurement of Impedance . . . 16
- 2.3 On the EIT Problem . . . 17
  - 2.3.1 Historical Sketch of the Reconstruction Problem . . . 18
  - 2.3.2 Reviewing mathematical Problems in EIT . . . 19
  - 2.3.3 Solution Strategies . . . 21
  - 2.3.4 Gauss-Newton Algorithm . . . 24
  - 2.3.5 Quantifying the Reconstruction Quality . . . 26
- 2.4 Finite Element Method in EIT . . . 29
  - 2.4.1 Motivation . . . 29
  - 2.4.2 Mesh Elements and Interpolation Functions . . . 30
  - 2.4.3 The weak form of the Laplace Equation . . . 30
  - 2.4.4 Global Solution . . . 32
- 2.5 Summary . . . 32

3 Artificial Neural Networks for time-independent Reconstructions 35
- 3.1 Basics of Artificial Neural Networks . . . 35
  - 3.1.1 The Neuron / fully connected Layer . . . 36
  - 3.1.2 Backpropagation . . . 36
  - 3.1.3 Weight Initialization . . . 38
  - 3.1.4 Components of an ANN . . . 39
- 3.2 Structure of the proposed Artificial Neural Network . . . 45
  - 3.2.1 Motivation . . . 45
  - 3.2.2 Architecture . . . 46

3.2.3 Loss Function . . . 49
3.3 Evaluation . . . 49
3.4 Training Data . . . 51
3.4.1 FEM Model Shape . . . 51
3.4.2 Targets . . . 52
3.4.3 Conductivity Range . . . 53
3.4.4 Noise Modelling . . . 54
3.4.5 Data Augmentation . . . 56
3.5 Summary . . . 57

4 D-Bar Algorithm **59**
4.1 Mathematical Outline of the D-Bar Algorithm . . . 59
4.1.1 From Laplace to Schrödinger . . . 60
4.1.2 The modified Schrödinger Equation . . . 61
4.1.3 Dirichlet-to-Neumann Map . . . 61
4.1.4 On the D-Bar Equation . . . 62
4.1.5 Retrieving the Conductivity . . . 63
4.1.6 Recap of the D-Bar Algorithm . . . 63
4.2 Numerical Implementation . . . 64
4.2.1 Dirichlet to Neumann Map . . . 64
4.2.2 Calculation of the Scattering Transform . . . 65
4.2.3 Solving the D-Bar Equation . . . 66
4.2.4 Reconstruction of Conductivities . . . 69
4.2.5 Summary . . . 69
4.3 Computational aspects in the real World . . . 71
4.3.1 Current Injection Pattern . . . 71
4.3.2 Non-circular Domain . . . 72
4.3.3 The 2-probe Measurement Problem . . . 73
4.4 Time-independent D-Bar (absolute) . . . 75
4.5 Time-independent D-Bar (frequency-differential) . . . 76
4.6 Fusion of EIT and other Modalities . . . 76
4.6.1 Fusion in the Scattering Transform . . . 77
4.6.2 EIT Simulation Setup for the Fusion . . . 78
4.6.3 Radar Simulation Setup . . . 79
4.6.4 Radar Reconstruction . . . 81
4.7 Summary . . . 83

5 Experimental Validation **85**
5.1 Artificial Neural Network . . . 85
5.1.1 Random Data . . . 85
5.1.2 Unseen Training Data . . . 86

5.1.3 Simulated Tank Data 89
5.1.4 Noise Performance 91
5.1.5 Tank Measurements 91
5.1.6 Pig Measurements 94
5.2 D-Bar under 4-probe Measurements 95
5.2.1 Simulation without Contact Impedance 95
5.2.2 Simulation with Contact Impedance 97
5.2.3 Tank Measurements without Contact Impedance 99
5.2.4 Tank Measurements with Contact Impedance 102
5.3 Time-independent D-Bar (absolute) 104
5.4 Time-independent D-Bar (frequency-differential) 106
5.5 D-Bar and a-priori Data 108
5.5.1 Base Reconstruction 108
5.5.2 Reconstruction under Noise 110
5.5.3 Conductivity Variation 110
5.6 Summary 116

6 Discussion **117**
6.1 Artificial Neural Networks for time-independent Reconstructions 117
6.1.1 Proposed ANN Architecture 117
6.1.2 Simulation Data 117
6.1.3 Performance Evaluation 117
6.2 D-Bar Algorithm 118
6.2.1 4-Probe Measurements 118
6.2.2 Absolute D-Bar 119
6.2.3 Frequency-Differential Reconstruction 119
6.2.4 A-Priori Data Integration 120

7 Conclusion and Outlook **121**

A Appendix **125**
A.1 D-Bar 125
A.2 The D-Bar Algorithm in pseudo Code 126
A.3 The D-Bar Algorithm through the eye of Systems Engineering 127
A.4 Peer-reviewed Journal Articles 130
A.5 Conference Proceedings 130
A.6 Supervised Student Theses 132

Bibliography **135**

Abbreviations and symbols

List of abbreviations

Abbrev.	Meaning
ANN	Artificial Neural Network
AR	Amplitude Response
CGO	Complex Geometric Optics
CT	Computed Tomography
DtN	Dirichlet-to-Neumann
EIM	Electrical Impedance Map
EIT	Electrical Impedance Tomography
FC	Fully Connected
FEM	Finite Element Method
FFT	Fast Fourier Transform
fom	figure of merit
GMRES	Generalized Minimal Residual
GN	Gauss-Newton
GREIT	Graz consensus Reconstruction algorithm for EIT
IFFT	Inverse Fast Fourier Transform
NtD	Neumann-to-Dirichlet
MRI	Magnetic Resonance Imaging
MSE	Mean-Squared Error
PE	Position Error
PReLU	Parametric ReLU
ReLU	Rectified Linear Unit
RNG	Ringing
MSE	root-mean-square deviation
SNR	Signal-to-Noise-Ratio
s.t.	subject to
std	standard deviation
MIMO	Multiple Input Multiple Output
BIE	Boundary Integral Equation

List of Latin Symbols

Symbol	Unit	Meaning
A	$[\mathrm{m}^2]$	cross-sectional area
$\tilde{\boldsymbol{A}}$	[]	system matrix
$\tilde{A}$	[]	Single entry of the system matrix
$\boldsymbol{B}$	[T]	magnetic field
$\boldsymbol{c}$	[]	scaling factor for mapping
c	[m/s]	speed of light in the domain
C_m	[F]	cell membrane capacity (Cole parameter)
$\boldsymbol{E}$	$[\mathrm{V\,m}^{-1}]$	electrical field
F	[]	forward model
f	[Hz]	frequency
G	[]	Greens's function
I_i	[A]	injected current
$\boldsymbol{I}$	[A]	current injection pattern
$\boldsymbol{J}$	$[\mathrm{A\,m}^{-2}]$	current density
$\vec{\boldsymbol{J}}$	[]	current injection pattern matrix
$\tilde{\boldsymbol{J}}$	[]	Jacobi matrix
j	[]	$j^2 = -1$
k	[]	complex-valued frequency-like parameter
$\boldsymbol{K}$	[]	regularization matrix
$\vec{\boldsymbol{K}}$	[]	k-space matrix
l	[m]	length
$\boldsymbol{L}_1$	$[\mathrm{V\,\Omega}^{-1}\,\mathrm{m}^{-2}]$	Dirichlet-to-Neumann map for constant domain
$\boldsymbol{L}_\sigma$	$[\mathrm{V\,\Omega}^{-1}\,\mathrm{m}^{-2}]$	Dirichlet-to-Neumann map for given conductivity
$\boldsymbol{n}$	[]	outward normal vector
O	[]	amplitude of a signal
$P(y)$	[]	marginal likelihood
$\boldsymbol{Q}$	[]	helper k-space matrix
R	[Ω]	electrical resistance
R_e	[Ω]	external resistance of extracellular space
R_i	[Ω]	internal resistance of the cell
$\boldsymbol{R}_\sigma$	$[\Omega\,\mathrm{m}^2\,\mathrm{V}^{-1}]$	Neumann-to-Dirichlet map

Symbol	Unit	Meaning
$\tilde{\boldsymbol{R}}$	[]	rotation matrix
$\boldsymbol{S}$	[]	scaling matrix for the electrode position
t	[s]	time
$U(\omega)$	[V]	voltage drop
$\boldsymbol{U}$	[V]	matrix of measured voltages
$\boldsymbol{v}$	[V]	measured voltages
$\boldsymbol{W}$	[]	weight matrix of an artificial neural network
X	[Ω]	reactance
$\boldsymbol{Y}$	[]	desired output of ANN
$\boldsymbol{Y'}$	[]	actual output of ANN
z	[]	complex number representation of position
Z_{ct}	[Ω]	contact impedance
Z_{sample}	[Ω]	sample impedance

List of Non-Latin Symbols

Symbol	Unit	Meaning
Φ	[V]	scalar potential
α	[]	Cole-Cole model correction term
$\boldsymbol{\sigma}$	[S/m]	conductivity distribution
$\boldsymbol{t}(k)$	[]	scattering transform
δ	[m]	skin depth
ϵ	[F/m]	permittivity
ϵ_0	[F/m]	vacuum permittivity
ϵ_∞	[F/m]	permittivity at infinite frequency
ϵ_s	[F/m]	static permittivity
η	[]	regularization parameter
$\hat{\omega}_i$	[]	ANN weights
$\mu(z,k)$	[]	solution to D-Bar equation
μ_0	[H/m]	vacuum permeability
σ	[S/m]	specific conductance
ω	[rad/s]	angular frequency
$\boldsymbol{\nabla}$	[]	Nabla operator $(\frac{\partial}{\partial x}, \frac{\partial}{\partial y}, \frac{\partial}{\partial z})$
$\times$	[]	cross product
$\times$	[]	$\boldsymbol{a} \times \boldsymbol{b} = \{a + jb \mid a \in \boldsymbol{a} \text{ and } b \in \boldsymbol{b}\}$
$\mathcal{R}$	[]	real number symbol
Ω	[]	domain to investigate
$\partial\Omega$	[]	boundary of the domain to investigate
$\CIRCLE$	[]	center of mass
$\oslash$	[]	element-wise division
$\boldsymbol{\Delta}$	[]	Laplacian $(\frac{\partial^2}{\partial x^2} + \frac{\partial^2}{\partial y^2} + \frac{\partial^2}{\partial z^2})$
Ψ	[]	solution to the Schrödinger equation
$\boldsymbol{\Lambda}$	[]	Dirichlet-to-Neumann
$\overline{\boldsymbol{\partial}}$	[]	D-Bar operator $\frac{1}{2}(\frac{\partial}{\partial x} + j\frac{\partial}{\partial y})$
$\odot$	[]	element-wise multiplication
Θ	[]	electrode position
$\boldsymbol{\Theta}$	[]	basis function for a mesh element

1 Introduction

Electrical Impedance Tomography (EIT) is a non-invasive imaging technique that reconstructs the conductivity distribution within a domain by measuring the boundary voltages resulting from injected currents. This method exploits the fact that different tissues and their states exhibit distinct electrical conductivities, rendering EIT particularly useful in medical applications. By placing electrodes on the surface of the domain, EIT can visualize internal structures and monitor physiological changes, providing diagnostic information without the need for ionizing radiation or expensive imaging equipment.

The concept of EIT was first strictly mathematically formalized by the Argentine mathematician Alberto Pedro Calderón in 1980, who posed the inverse boundary value problem that formalizes the underlying problem in EIT. The first spractical implementations of EIT emerged in the 1980s, primarily for geophysical applications.[1] Nevertheless, it was not until the late 1980s and early 1990s that EIT began to gain traction in medical imaging, driven by advancements in computational power and algorithm development [Cal80] [SU87]. Notable achievements include the development of the Gauss-Newton (GN) algorithm for iterative reconstruction and the introduction of the D-Bar algorithm, which provided a direct solution approach to the EIT problem [YWT87], [IMNS04].

Current research in EIT reconstruction is focused on developing improved algorithms and methodologies for time-independent EIT. The potential benefits include enhanced image reconstruction quality, reduced computational complexity, and increased robustness to measurement noise. These advantages could lead to the development of more accurate and reliable diagnostic tools in medical imaging. EIT's capacity to differentiate between various tissue types and states based on their electrical properties offers considerable promise for the monitoring of conditions such as acute respiratory distress syndrome, the detection of cancer, and the assessment of lung function. Nevertheless, practical challenges such as hardware complexity, measurement errors, and the ill-posed nature of the inverse problem have constrained its widespread adoption.

While time-dependent EIT has demonstrated potential in applications such as real-time lung monitoring, there are significant areas where time-independent EIT is more feasible and beneficial [TC19]. Time-independent EIT is a method of reconstructing the conductivity distribution at a single point in time. This makes it suitable for applications where dynamic changes are either minimal or irrelevant. One of the key application areas is cancer detection, where time-

[1] It is noted that Henderson and Webster developed a predecessor of an EIT imaging technique [HW78]. Strictly speaking, this is not EIT, but nevertheless they made a great step in the advancement of EIT.

independent EIT can be used to identify tumors based on their distinct conductivity profiles compared to surrounding healthy tissue. This is particularly useful for breast cancer screening, where EIT can complement traditional mammography by providing additional contrast information [RGMK+22]. Another application is the estimation of bladder volume [LCS+18], [SNLW14]. This can be achieved by reconstructing the conductivity distribution within the pelvic region, which is crucial for patients with urinary retention issues or those requiring regular monitoring of bladder function.

In time-independent EIT imaging, EITcan assist in the detection of abnormalities such as tumors, hemorrhages, ischemic regions within the brain or fatty livers [PAM+23], [SWW+21], [GAD+18], [CHS+21], [KHH+22], [CHS+21]. Its non-invasive nature renders it a safer alternative to traditional imaging techniques such as Computed Tomography (CT) or Magnetic Resonance Imaging (MRI), particularly for patients requiring frequent monitoring. Furthermore, in orthopedic applications, EIT could be utilized to assess bone health and detect fractures or infections [ARP+23]. The capacity to visualize the conductivity distribution within bones leads to invaluable data for the diagnosis and monitoring of conditions such as osteoporosis or osteomyelitis. Another application is in the phenotyping of plants based on the conductivity distribution from their root system [CLSR+19].

In geophysics, EIT, which is often referred to as Electrical Resistivity Tomography, has been employed to map subsurface structures. This application is of great importance for the exploration of natural resources, such as minerals and groundwater, as well as for the monitoring of environmental changes. EIT could be used to characterize soil and rock properties, detect contamination, and assess slope stability, which is of vital importance for landslide risk management and infrastructure safety [Boy16] [CFG+19]. EIT can also be utilized in industrial settings to monitor processes within pipelines and reactors. It provides real-time visualization of material flow, which is essential for ensuring efficient and safe operations. This capability is particularly useful in chemical engineering, where the distribution and movement of fluids, suspensions and gases within reactors can be monitored in real time to optimize reactions and prevent blockages or other issues [MGGM18], [IGBY05]. In the field of material science, EIT can be used to study the properties of composite materials and to detect defects. By imaging the internal conductivity distribution, researchers can identify variations in material composition, detect cracks, and assess the overall integrity of materials. This application is of significant value in the fields of quality control and the development of new materials with specific properties [ZMC+22].

Aim of the Thesis

Current Obstacles

EIT is confronted with a number of significant challenges and limitations that hinders its extensive adoption and practical application. One significant issue is the complexity of the hardware, particularly in the case of advanced reconstruction algorithms such as the D-Bar algorithm, which necessitate 2- and 3-probe measurements in order to function correctly. This entails the use of sophisticated hardware capable of precise current injection and voltage measurement across multiple electrodes simultaneously, which complicates the design and increases costs. Measurement errors also represent a significant challenge, particularly in time-independent EIT. While time-dependent EIT can effectively mitigate modeling inaccuracies of the domain, noise, and hardware imperfections, these errors persist in time-independent EIT, resulting in a deterioration of reconstruction quality. Additionally, the ill-posed nature of the inverse problem in EIT means that small changes in measured data can lead to large variations in reconstructed images, necessitating regularization techniques that add complexity and may not always yield satisfactory results.

Research Gap

Despite advancements in EIT technology and methodologies, several gaps remain in the existing research that this thesis aims to address. These gaps are particularly pronounced in the context of time-independent EIT, where the lack of temporal data exacerbates the inherent challenges. The specific research gaps addressed in this thesis include:

- **Improvement in Time-Independent Reconstruction Algorithms**: Current reconstruction algorithms often struggle with the ill-posed nature of the EIT problem, leading to poor image quality and resolution. This is particularly challenging in time-independent EIT, where the lack of temporal data exacerbates the instability of the inverse problem. It is necessary to develop new algorithms that can provide more accurate and stable reconstructions in the time-independent case. These algorithms should leverage advanced mathematical techniques and computational methods to enhance image quality.

- **Enhanced Robustness to Measurement Errors**: Existing EIT systems are highly susceptible to measurement errors, which can degrade the quality of the reconstructed images. This thesis aims to develop techniques that enhance the robustness of EIT reconstructions to such

errors, ensuring more reliable and consistent results. This includes addressing errors that persist in time-independent EIT, such as modeling inaccuracies, noise, and hardware imperfections. By improving error handling and correction mechanisms, the reliability of EIT systems can be significantly enhanced.

- **Theoretical Foundations for General Reconstruction Approaches**: While application-specific solutions are valuable, there is a need for a more theoretical foundation for general approaches to reconstruction in the time-independent case. This includes the development of robust algorithms that can be applied across various domains without relying heavily on specific application knowledge. Techniques such as Artificial Neural Network (ANN) can be employed to incorporate domain knowledge where applicable, but the primary focus should be on creating versatile and adaptable reconstruction methods that can handle a wide range of scenarios.

- **D-Bar Frequency Differential Approach**: The D-Bar algorithm, particularly in its frequency differential form, offers a promising path for time-independent EIT. This approach leverages the frequency-dependent conductivity of tissues to enhance the contrast and provide additional diagnostic information. By comparing reconstructions at different frequencies, valuable insights into the frequency-dependent properties of tissues can be gained. This thesis aims to explore and refine the D-Bar frequency differential approach to improve the accuracy and applicability of time-independent EIT.

Contributions of the Thesis

By addressing these gaps, this thesis aims to advance the field of EIT, making it a more viable and effective tool for various medical and industrial applications. The potential benefits include improved image reconstruction quality, enhanced computational efficiency, and increased robustness to measurement noise, ultimately leading to more accurate and reliable diagnostic tools. Additionally, the thesis explores the use of the D-Bar algorithm and frequency differential reconstruction to further enhance the capabilities of time-independent EIT.

Structure of the Thesis

This section provides a brief summary of each chapter in the thesis, outlining the main topics and how they contribute to the overall research objectives:

Foundations of EIT

This chapter explores the foundational principles of Electrical Impedance Tomography (EIT). It covers the medical background, bio-impedance fundamentals, and the mathematical formulation of the EIT problem. The chapter discusses various solution strategies, such as variational regularization, statistical inversion, and direct solution approaches, with a focus on the Gauss-Newton (GN) algorithm. It also delves into the Finite Element Method (FEM) in EIT and the metrics for quantifying reconstruction quality.

Artificial Neural Networks for EIT

This chapter examines the application of ANNs for EIT reconstruction. It covers the basics of ANNs, including their components and training processes. The proposed ANN architecture for EIT is introduced, highlighting its innovative features and the motivation behind its design. The chapter also discusses the evaluation of the ANN using simulated data, noisy FEM data, tank data, and real pig data.

D-Bar Algorithm

This chapter provides a comprehensive overview of the D-Bar algorithm, a direct method for solving the inverse problem in EIT. It includes a detailed mathematical outline of the algorithm, practical considerations for implementation, and the numerical implementation process. Additionally, the chapter examines the integration of EIT with radar data to enhance spatial resolution.

Practical Analysis

This chapter presents a practical analysis of the proposed methods and algorithms. It includes the evaluation of the ANN and D-Bar algorithm using various data sets, such as simulated data, tank data, and real pig data. The chapter also discusses the performance of the algorithms under different conditions, such as noise and hardware limitations, and provides insights into their practical applicability. This section discusses the performance of the algorithms under various conditions, such as different noise levels and hardware limitations, to assess their robustness and reliability.

Insights into Practical Applicability

This section provides insights into the practical applicability of the ANN and D-Bar algorithms, highlighting their strengths and limitations in real-world

scenarios. This chapter presents a comparative analysis of the ANN and D-Bar algorithms, highlighting their respective advantages and areas for improvement. Additionally, it explores the implications of the research for the field of EIT and suggests potential applications and future research directions.

Conclusion and Future Work

The chapter also considers the limitations of the current study and suggests paths for further research to address these limitations and advance the field of EIT. By following this structure, the thesis aims to provide a comprehensive and coherent exploration of time-independent EIT, addressing the identified research gaps and contributing to the advancement of EIT techniques and applications.

2 Foundations of Electrical Impedance Tomography

EIT is a non-invasive imaging technique that reconstructs the conductivity distribution within a domain, making it particularly useful in medical applications. Different tissues and their states exhibit distinct conductivities, allowing EIT to monitor conditions such as acute respiratory distress syndrome or detect cancer. The technique involves placing electrodes on the surface of the domain to inject current and measure voltages. From these, the inner distribution of the tissue impedance can be reconstructed. Despite theoretical advancements, practical challenges such as hardware complexity and measurement errors persist. This chapter explores the foundational principles, challenges, and methodologies of EIT, emphasizing its potential and limitations in medical imaging.

2.1 Application in the medical Domain

EIT is used to visualize the conductivity distribution within a region, using the conductivity charactersitics of different tissues and their states, to diagnose and monitor conditions such as acute respiratory distress syndrome and cancer. This section examines the methods used to obtain conductivity distributions. Both time-dependent and time-independent processes are covered, with an emphasis on the importance of measurement patterns. Techniques such as the adjacent-adjacent and trigonometric patterns are discussed, each with unique advantages and challenges. Through an understanding of these patterns, the practical applications and limitations of EIT in clinical settings will be better appreciated.

2.1.1 General Benefit of EIT in the medical Context

EIT aims to recover the distribution of tissues due to their electrical properties in a domain under measurement. In the medical context, this is very helpful, as different tissue types have different conductivities. But not only does tissue itself differ in conductivity, so does the physical state of the tissue. Acute respiratory distress syndrome, for example, describes a condition where fluid leaks into the alveoles and thus, deprives gas exchange. This fluid changes the conductivity of the lung compared to the healthy state, and thus can in theory be detected through an EIT image.

2.1.2 Different Approaches of retrieving Information

In general, EIT can help to visualize time-varying or time-dependent and static or time-independent processes in the human body. The overview is depicted

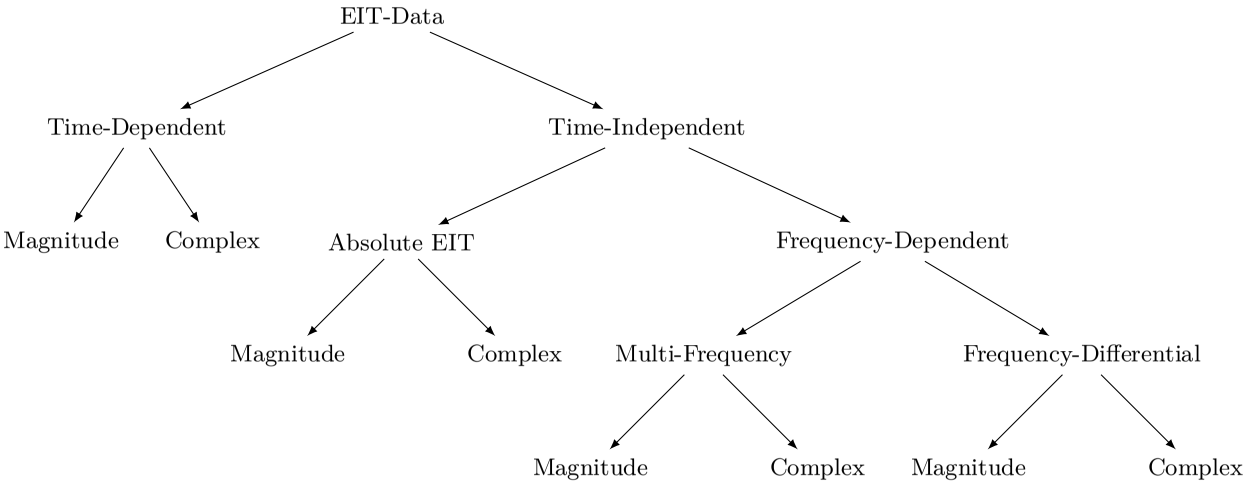


Figure 2.1: Visualization of different means to gather information about the conductivity of the domain in EIT.

in Figure 2.1.

Time-dependent analysis requires knowledge of measurements from two different time points. This allows for visualizations of changes in conductivity over these two time points, e.g., for monitoring the lung. The input for the reconstruction is the difference in voltage between two-time points $\boldsymbol{v}_{t-diff} = \boldsymbol{v}_{t1} - \boldsymbol{v}_{t0}$ or $\boldsymbol{v}_{t-diff} = (\boldsymbol{v}_{t1} - \boldsymbol{v}_{t0})/\boldsymbol{v}_{t0}$. The reference voltage $\boldsymbol{v}_{t0}$ can either be captured at a real point in time or be constructed from, e.g., the average past points in time. The voltages $\boldsymbol{v}$ can either be complex or purely real-valued. The critical feature here is that getting an image takes at least two measurements from different times.

Time-independent EIT stems from the fact that the reconstruction only relies on a specific point in time. Absolute EIT is the process of reconstructing the conductivity enclosure in the domain, just like the Chaldéron problem described in section 2.3.1. One could distinguish absolute EIT in two subgroups: Quantitative EIT, where the exact numerically correct conductivity distribution is desired, and qualitative EIT, where the exact value of the conductivity is only of second interest. Here, the visual identification of the distribution of inclusions is preferred. Then there are frequency-dependent approaches. As noted in section 2.2.2, biological tissue exhibits a shift in conductivity depending on frequency. This effect can be used for reconstruction. When injecting currents of multiple frequencies, the different conductivities at each frequency influence the measured voltage, thus giving more information for the reconstruction process. The simplest case would be frequency-differential EIT, where the frequency difference contrast is visualized. One can speak of multi-frequency reconstruction when more current frequencies are used. Using either real-valued or complex-valued conductivities and voltages is permitted in the time-independent domain. With these time-independent EIT images, in theory more states of the human body can be estimated. Detection of cancer or estimation of the bladder volume are two examples, where time-independent reconstruction could deliver substantial benefit.

2.1.3 Simulation and Measurement Patterns

To retrieve the conductivity distribution inside a domain, electrodes are placed on the surface. For each measurement, a current needs to be injected through the electrodes and voltage measurements need to be made. More in-depth details about this will be presented in section 2.2.3. However, the specific choice of the injection and measurement sites is not straightforward. In theory, any combination of electrodes can be used for injecting a current and any combination of electrodes can be utilized to gather the voltage drop between them.

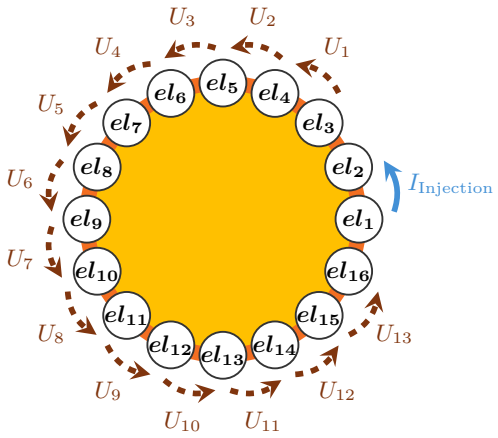


Figure 2.2: Visualization of the first injection and first 16 measurements in the adjacent-adjacent pattern for a domain with 16 electrodes attached to it. In blue, the the electrodes for current injection are visualized, while the voltage measurements are marked as a brown dashed line.

In practice, the most widely used injection and measurement pattern is the so-called adjacent-adjacent/skip-0-0 pattern. Here, a current is injected between two electrodes, and the voltage measurements are carried out between every other neighboring electrode. The first injection and the corresponding measurements can be seen in Figure 2.2. When the measurements have been performed, the injection pair rotates one electrode to the right, such that the next injection pair is the combination of electrodes 2 and 3. The measurements are then carried out on all other neighboring electrode pairs. This is repeated until each electrode pair has been used for injection. For a 16-electrode system, in this way $16 \cdot 13 = 208$ measurements can be gathered. There also are skip-X-Y patterns, which inject the current sill through two electrodes, but between the two electrodes are X other electrodes. This pattern allows for the current to penetrate deeper into the domain. The voltage measurements are carried out the same way: voltages are measured between two electrodes with Y electrodes between them. The larger the X and Y values, the more sensitive the measurements get at the center of the domain. Even though the skip-0-0 pattern does not yield the best measurement results, it is used throughout the work, as most EIT devices only support this pattern [AGM11].

There is one current pattern which gives the theoreticaly best measurement of the domain, the so-called trigonometric pattern. Its performance stems from

the fact, that a system with N electrodes has $N-1$ unique linear independent current injection patterns, given that the potential is directly measured on each electrode. This can be shown as follows. A current pattern can be expressed as

$$\boldsymbol{I}_l = (I_{l,1}, I_{l,2}, ..., I_{l,N}) \quad \forall\, l \in \{1, 2, ..., N-1\} \tag{2.1}$$

$$s.t.\ 0 = \sum_{i}^{N} I_{l,i}, \tag{2.2}$$

where $I_{l,i}$ is the current of the l^{th} current pattern on the electrode i. To show that there are only $N-1$ linear independent current patterns, a new current pattern $\boldsymbol{I}_N$ needs to satisfy

$$\boldsymbol{I}_N = \sum_{l}^{N-1} \boldsymbol{c_l} \boldsymbol{I}_l, \tag{2.3}$$

as it needs to be expressed in terms of all other current patterns. Thus, there are N equations as every current pattern $\boldsymbol{I}_l$ is an N dimensional vector. However, there are only $N-1$ unknowns. The new current pattern must fulfill Kirchhoff's law. One of the equations is redundant and thus, there are indeed only $N-1$ linear independent current patterns. The trigonometric pattern itself is best described through the matrix of current injections $\boldsymbol{J}$. It describes for each column a different current injection scheme, and in each row the injection current at an electrode. Thus, each entry of $\boldsymbol{J}$ is defined as

$$J_{n,m} = \begin{cases} O\cos(m\Theta_n), & m = 1, ..., N/2 \\ O\sin((m - N/2)\Theta_n), & m = N/2+1, ..., N-1 \end{cases}, \tag{2.4}$$

where Θ_n describes the location of the n^{th} electrode in terms of its angle with respect to the center of Ω and O is the amplitude of the injected current. For the case of $m = 8$ a sample, the current pattern is visualized in Figure 2.3.

However, in real life, this scheme has two fatal flaws. At first, the realization in hardware is very complicated. Secondly, the measurement errors are high, due to the fact, that every measurement is a two-probe measurement (see section 2.2.3 for more details). Thus, this pattern is mostly used in theoretical work.

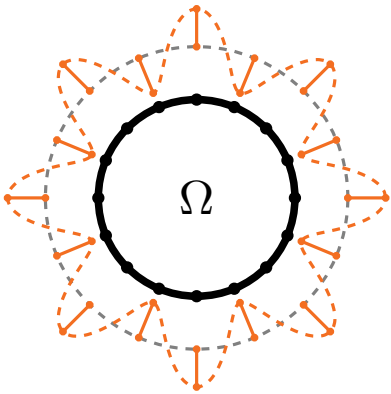


Figure 2.3: Visualization of a trigonometric current injection pattern for $m = 8$ as described in equation (2.4). The circles embedded in the large circle are electrodes, while the gray dashed line denotes a reference for the amplitude O (as defined in equation (2.4)) of zero of the current. The current itself is represented by the orange dashed line.

2.2 Bio-Impedance Fundamentals

Impedance measurement techniques are essential for accurately assessing the electrical passive properties of biological tissues. This section examines the various methods used to measure bio-impedance, with an emphasis on their practical applications and inherent challenges. Techniques such as the two-probe and four-probe configurations are discussed, highlighting their respective advantages and limitations. The effects of electrode placement, contact impedance and frequency-dependent behavior on measurement accuracy are examined. By understanding these techniques, the complexity of bio-impedance measurements and their implications for medical diagnostics and research can be better appreciated.

2.2.1 Modelling electrical Systems

The behavior of an electrical system for the low-frequency case can be formally described as follows. For EIT a source-free domain is assumed. This assumption also holds true for the human body, as the frequency of the potential applied by the body's mechanism, like the heart, are orders of magnitude smaller than the impedance measurements. This allows for considering the

simplified Maxwell equation, which can be stated as follows:

$$\text{Gauss's law of electricity: } \boldsymbol{\nabla} \cdot \boldsymbol{E} = 0, \tag{2.5}$$

$$\text{Farady's law of induction: } \boldsymbol{\nabla} \times \boldsymbol{E} = -\frac{\partial \boldsymbol{B}}{\partial t}, \tag{2.6}$$

$$\text{Ampère's law: } \boldsymbol{\nabla} \times \boldsymbol{B} = \mu_0 \sigma \boldsymbol{E} + \mu_0 \epsilon_0 \frac{\partial \boldsymbol{E}}{\partial t}, \tag{2.7}$$

where $\boldsymbol{\nabla} = (\frac{\partial}{\partial x}, \frac{\partial}{\partial y}, \frac{\partial}{\partial z})$ is the nabla operator, the electrical field is defined as $\boldsymbol{E}$, the cross product is denoted by $\times$, the magnetic field is defined as $\boldsymbol{B}$, the vacuum permeability is defined as μ_o, the specific conductance is defined as σ and the vacuum permittivity is defined as ϵ_0. For the time-harmonic case, which means that the fields are varying sinusoidal with time (this holds true for EIT), we can replace the derivative by multiplication $j\omega$ (with $j^2 = -1$), resulting in

$$\boldsymbol{\nabla} \times E = -j\omega \boldsymbol{B} \tag{2.8}$$

and

$$\boldsymbol{\nabla} \times \boldsymbol{B} = \mu_0(\sigma + j\omega\epsilon_0)\boldsymbol{E}. \tag{2.9}$$

With the help of the vector identity, $\boldsymbol{\nabla} \times (\boldsymbol{\nabla} \times \boldsymbol{P}) = \boldsymbol{\nabla}(\boldsymbol{\nabla} \cdot \boldsymbol{P}) - \boldsymbol{\nabla}^2 \boldsymbol{P}$ (with $\boldsymbol{P}$ being an arbitrary vector), taking the curl of equation (2.8) and substituting $\boldsymbol{B}$ in equation (2.9) leads to

$$\boldsymbol{\nabla}^2 \boldsymbol{E} - j\omega\mu_0\epsilon_0\boldsymbol{E} - \omega^2\mu_0\epsilon_0\boldsymbol{E} = 0. \tag{2.10}$$

Since the wavelength is high compared to the largest distance inside Ω investigated in EIT and time variation is thus low, the time derivatives vanish. This leads to

$$\boldsymbol{\nabla}^2 \boldsymbol{E} = 0. \tag{2.11}$$

This result is the Laplace equation for an arbitrary conductivity, σ. Conservation of charge requires

$$\boldsymbol{\nabla} \cdot \boldsymbol{J} = 0. \tag{2.12}$$

With Ohms' law $\boldsymbol{J} = \sigma \boldsymbol{E}$ and $\boldsymbol{E} = -\boldsymbol{\nabla}\Phi$, the Laplace equation with respect to the scalar potential Φ can be derived

$$\boldsymbol{\nabla} \cdot (-\sigma \boldsymbol{\nabla}\Phi) = 0. \tag{2.13}$$

More in-depth details about the Maxwell equations can be found in [Leh18]. However, these quasi-static approximations fail to produce a good result. This

occurs when the medium in which the fields propagate through is in the scale of the wavelength and the skin depth. The condition can be stated as:

$$\frac{1}{2}(\frac{l}{\delta})^2 + 4\pi^2 j(\frac{l}{\lambda})^2 \ll 1, \tag{2.14}$$

with the wavelength $\lambda = \frac{2\pi c}{\omega}$, the speed of light in the domain $c = \frac{1}{\sqrt{\mu\epsilon}}$, $\delta = \frac{1}{\sqrt{\omega\sigma\mu/2}}$ denotes the skin depth and l representing the smallest length over which fields vary [HA22] [Lar07] [1]. This means that the domain length in EIT has to be smaller than that value.

2.2.2 Impedance of Tissue

Biological tissue is electrically conductive. The conductivity of tissue is closely related to ionic concentrations, as many body functions deal with ions (e.g., potassium, bicarbonate, or calcium). The measured conductivity might vary depending on the tissue type due to cell density and architecture. This conductance is due to ions, which can move. Bound charges within tissues give rise to complex dielectric properties, resulting in frequency-dependent conductivity and permittivity [DRMS08]. Three distinct regions can be distinguished:

1. α-dispersion is found in the range of 10 Hz to a few kHz, which is associated with the interfaces of tissues such as membranes.

2. β-dispersion is found in the range of 1 kHz to several MHz, related to polarizing cell membranes and proteins and other organic macromolecules.

3. γ-dispersion is found for frequencies greater than 10 GHz is associated with water molecule polarization.

An idealized visualization of the dispersion regions can be seen in Figure 2.4. Different tissues exhibit different such curves. Cells in the tissue are surrounded by extracellular fluid and separated by a membrane. Thus, tissues exhibit a complex conductivity capacitive conductivity. The model for a cell is shown in Fig. 2.5. This is derived from the Cole-Cole model, which is used to describe the frequency dependency of tissues. It can be stated as

$$\boldsymbol{\epsilon} = \epsilon_\infty + \frac{\epsilon_s - \epsilon_\infty}{1 + (j\omega\tau)^{1-\alpha}},$$

[1] Further readings regarding this topic can be found in chapter 5 of the book "Electrical Impedance Tomography" by David Holder and Andy Adler [HA22].

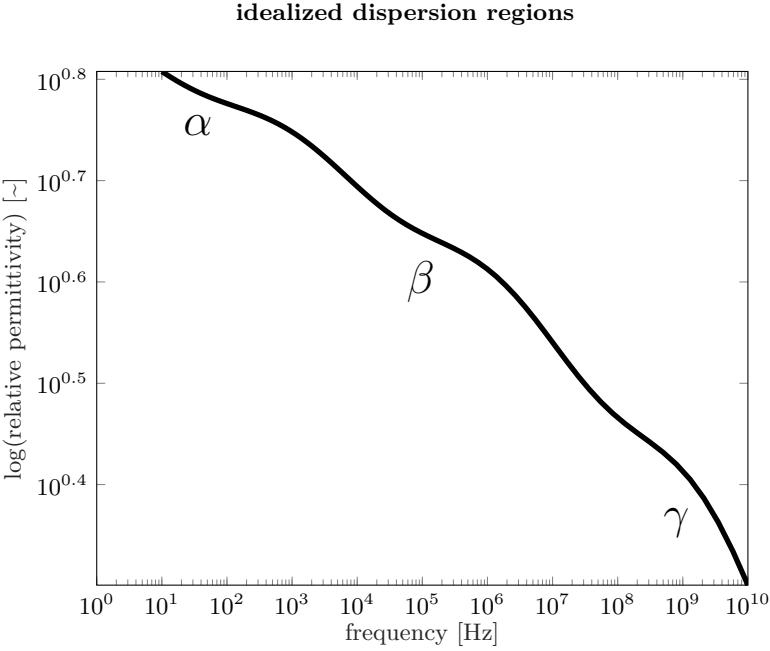


Figure 2.4: Idealized version of the dispersion regions for better visualization — adapted from [DRMS08].

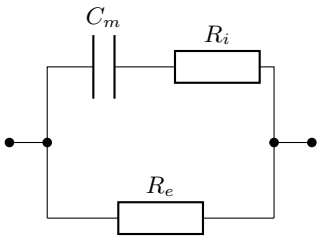


Figure 2.5: Model of the cell conductivity, with the external resistance of the extracellular space R_e, the capacitive behavior of the cell wall C_m and the internal resistance of the cell R_i.

where ϵ_∞ is the permittivity at a frequency of infinity, ϵ_s represents the static permittivity and the parameter α is a correction term that arises from practical measurements [CC41].

Typically, bio-impedance measurements are carried out in the β-dispersion region. This is because designing measurement hardware is easier in lower frequencies, as problems that arise from noise or parasitic effects in the measurement circuit are more manageable.

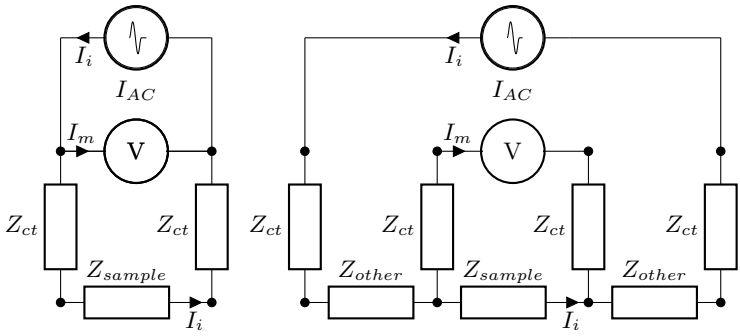
When measuring tissue impedance, however, the device will output an impedance value rather than the underlying tissue properties. This is a result of geometry, which has to be corrected. Given a measurement of the resistance R in a cylindrical object with the longitudinal flow of current, the conductivity σ can be calculated as $\sigma = \frac{1}{R}\frac{l}{A}$, where l is the length and A is the cross-sectional surface area. This is also true for reactance X with $\epsilon = \frac{1}{j\omega X}\frac{l}{A}$.

Also worth mentioning is that some tissue types, like the heart or sceletal muscle, exhibit anisotropic conductivities. In this case, σ is a tensor.

2.2.3 Measurement of Impedance

Measurement of impedance is an active process, meaning that a current needs to be actively applied to the subject under test. The easiest way is to inject a current I_i through two electrodes into the sample and measure the voltage drop $U(\omega)$ on the same electrodes. This concept is visualized in Figure 2.6a. However, this also measures the contact impedance Z_{ct} as it naturally arises due to the connection of electrodes.

To overcome this, a four-probe measurement is preferred. Here, the voltage measurement is done through a different pair of electrodes, resulting in a more



(a) Two-probe impedance measurement arrangement.

(b) Four-probe impedance measurement arrangement.

Figure 2.6: Impedance measurement set-up. I_i is the injected current for the impedance measurement from the current source I_{AC}, I_m is the current that flows into the voltage measurement. This is very close to 0 A as the voltage measurement has a very high input impedance. Z_{ct} is the contact impedance when connecting to the sample. Z_{other} is an impedance part of the sample but not measured. Z_{sample} is the sample's measured impedance.

accurate measurement of the sample Z_{sample}, as the current that flows into the voltage measurement circuit is very low. The concept is visualized in Figure 2.6b. Typically in the human body $Z_{sample} \ll Z_{ct}$, meaning that the contat impedance is order fo magnitude greater then the measured tissue. This is the preferred type of measurement for biological tissues. Note that this shows a simplified contact impedance; the electrodes will develop a half-cell potential in a real-world setting. This could be modeled by adding a voltage source at Z_{ct}. If this is unbalanced, it can corrupt even the four-probe measurements.

2.3 On the EIT Problem

In the following, the mathematical and practical challenges associated with EIT, an imaging technique used to reconstruct the conductivity distribution within a domain based on boundary measurements will be discussed. The EIT problem is classified as a nonlinear ill-posed inverse problem, meaning that it often lacks stability and uniqueness in its solutions. The text outlines the fundamental equations governing EIT will be outlined, including the Laplace equation for the electric potential and the boundary conditions. It also highlights the historical development of the Calderón problem, which forms the

theoretical basis of EIT, and the various solution strategies employed, such as variational regularization, statistical inversion and direct solution approaches will be highlighted. In addition, the text examines the Gauss-Newton (GN) algorithm, a common iterative method used to solve the EIT problem, and discusses the importance of regularization to ensure stable and meaningful solutions. Finally, it presents metrics for quantifying the quality of EIT reconstructions, emphasizing the need for accurate and reliable imaging in practical applications.

2.3.1 Historical Sketch of the Reconstruction Problem

The EIT problem can be formally stated as follows.

Let $\Omega \subseteq \mathcal{R}^n$ for $n \geq 2$ be a bounded domain and $\partial\Omega$ its boundary. The equation governing the distribution of the electric potential $\Phi(\boldsymbol{x})$ in Ω is the Laplace equation (2.13) $\boldsymbol{\nabla} \cdot (-\sigma(\boldsymbol{x})\boldsymbol{\nabla}\Phi(\boldsymbol{x})) = 0$, where $\boldsymbol{x}$ denotes the position in $\mathcal{R}^n$. Note that the conductivity can be complex. The inverse problem is finding the $\sigma(\boldsymbol{x})$ distribution in Ω to match the Dirichlet and Neumann boundary conditions on $\partial\Omega$.

The Dirichlet boundary condition is a scalar potential $\Phi(\boldsymbol{x})$ applied on the boundary, which can be expressed as $\Phi(\boldsymbol{x}) = f(\boldsymbol{x}) \; \forall \boldsymbol{x} \in \partial\Omega$. They are gathered in the real world from the voltage measurements on $\partial\Omega$ or to be more precise from the electrodes on $\partial\Omega$, when a current is injected through the electrodes.

The Neumann boundary condition, on the other hand, can be expressed as $\frac{\partial\Phi(\boldsymbol{x})}{\partial \boldsymbol{n}} = g(\boldsymbol{x}) \; \forall \boldsymbol{x} \in \partial\Omega$, where $\frac{\partial\Phi(\boldsymbol{x})}{\partial \boldsymbol{n}}$ represents the derivative of the scalar potential concerning the outward normal vector on the boundary $\partial\Omega$. In practice, this is the current density $\boldsymbol{J}(\boldsymbol{x})$ on the boundary. This can be seen with the help of description of the normal component of the electrical field $\boldsymbol{E}_n(\boldsymbol{x})$, which is related to the potential with $\boldsymbol{E}_n(\boldsymbol{x}) = -\frac{\partial\Phi(\boldsymbol{x})}{\partial \boldsymbol{n}}$ and $\boldsymbol{J}(\boldsymbol{x}) = \sigma(\boldsymbol{x})\boldsymbol{E}(\boldsymbol{x})$. In the real world, the Neumann boundary conditions are typically known, as they simply are the current injected through the electrodes on $\partial\Omega$. In essence, the EIT problem is to derive the conductivity from impedance measurements. The very first formal statement of this problem was by the Argentinian mathematician Alberto Pedro Calderón in 1980 in his paper "On an inverse boundary value problem" [Cal80] [2]. Although his paper did not provide a solution or proof that the problem was solvable, it tremendously impacted inverse problems and EIT. In 1987, the very first proof of the uniqueness of the Calderón problem was presented for dimensions $\mathcal{R}^n$ with $n \geq 3$ [SU87]. It is noteworthy that their proof

[2] It is important to note that Henderson and Webster designed a system for collecting impedances in the thorax in 1978 [HW78]. However, they did not stated the problem in a solvable mathematical form.

required twice differentiable conductivities. This means that the conductivity is not allowed to change rapidly, which is violated in real-world settings. Since then, several proofs have shown the uniqueness of the solution with more relaxed assumptions [Nac96] [HT13]. Nachmann's publication had the strongest impact on the solution of the Calderón problem. It relaxes the dimension of Ω to $n = 2$ and assumes twice weakly differentiable[3] conductivities. While still somewhat smooth, it comes closer to reality. The usage of complex geometric optic solutions and the non-linear Fourier transform sparked the development of implementations of the so-called D-Bar algorithm.

However, it is not clear whether the real-world EIT problem has a theoretically sound, unique solution. This is because the measurement currents are in a three-dimensional space in most real-world settings. At the same time, only measurements across a two-dimensional cross-section of the body are present. Furthermore, only measurements on the exact spots of the electrode locations are available. Thus, only knowledge of parts of the potential distribution on the domain boundary is available.

2.3.2 Reviewing mathematical Problems in EIT

Mathematical Problems in EIT

The EIT problem belongs to the class of non-linear ill-posed inverse problems. An inverse problem deals with finding the cause based on an observed effect. The term ill-posed is the opposite of a well-posed problem. A well-posed problem, as defined by Hadamard [Had02], implies:

- **Existence**: there exists at least one solution for the problem,
- **Uniqueness**: there exists only one solution, and
- **Stability**: the solution depends continuously on the data

The requirement for existence is true for EIT as even in the real-world setting, there is at least one solution, namely the measured impedance distribution by, e.g., the human body itself. For the requirement of uniqueness, however, it is not clear whether this holds true in the real-world case (see: section 2.3.1), but due to the research in the field, one can be mildly optimistic that uniqueness also holds true.

[3] An intuitive understanding of weak differentiability can be gathered from looking at the classical derivative, which measures how much a function changes at one specific point. For the weak differentiability, this definition is broadened because it describes a sort of average differentiability in a region around each point. This still captures a function's overall derivative behavior but allows for discontinuity in specific points. This later becomes handy for the usage in chapter 2.4.

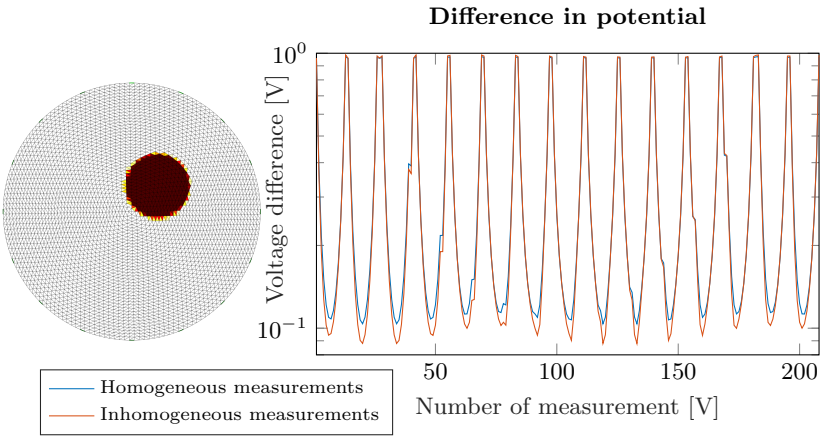


Figure 2.7: To the left the simulated target for the inhomogeneous measurements is visualized, it has 300% of the background conductivity. On the right, the resulting voltage measurements are displayed on a logarithmic scale. The blue graph represents the homogeneous case, and the orange graph is the one with the target. Although the difference in the target conductivity is very high, the voltages do not change much.

The stability, on the other hand, is violated. This is because a large change in conductivity only results in a small change in the outer potential distribution of the domain. This can be seen in Figure 2.7. In there, the difference in the boundary between a conductivity enclosure of 2 $\mathrm{S\,m^{-1}}$ and one on the same position with 4 $\mathrm{S\,m^{-1}}$ can be observed. While the enclosure has double the conductivity value, the changes in potential are up to two orders of magnitude smaller. For EIT this means that the small changes in voltage on the boundary can lead to high changes in conductivity. This renders EIT greatly affected by noise.

But also the non-linearity of EIT is challenging. In CT, the X-rays path through the domain in a straight line. This allows for easy reconstruction of an image through filtered back projection. In EIT, on the other hand, the current fans out and thus simple algorithms like back projection lead to diffuse images.

Measurements

Another problem in EIT is the measurement process itself. In the real world, the knowledge about the outer domain's potential is incomplete. This is because electrodes need to be used for current injection or voltage measurement. The potential is only known on the electrodes. This severely limits the knowledge of the boundary potential. Increasing the number of electrodes will give better knowledge about the boundary potential, but on the other hand, it dampens the voltage amplitude and makes handling more complicated in practice.

Another factor is the electrode's physical size. The bigger the electrode, the easier to ensure contact with the domain in a real-world setting. EIT electrodes belts for application in pulmonary monitoring have relatively larger surface areas as compared to, e.g., electrocardiography electrodes. However, this again limits the resolution on the boundary potential, as the potential on the whole electrode is the same.

Another factor that limits the knowledge of the boundary potential distribution is the electrode contact impedance. In a real-world setting, each electrode has a contact impedance. This results from the human skin, the electrode gel used, the electrode material, and the geometry of the electrode. Generally, the electrode impedance is higher than that of the measured tissue. To reduce the impact in EIT four-probe measurements are used. Thus, the potential distribution of current-injecting electrodes is unknown.

Different current injection patterns have different resolutions and thus different reconstruction qualities [AGM11] [DBD$^+$21]. Although some patterns like trigonometric injection patterns lead to the best reconstruction quality in theory, they are also more prone to errors and thus avoided in the real world [KVKK97]. For the case of trigonometric patterns the hardware requirements are also more complex. Despite exhaustive research no device is known to be capable of it.

Depending on the part of the body to measure, physiological effects such as breath or muscle tension can also limit the quality of measurements.

2.3.3 Solution Strategies

In general, three different solution strategies can be used for solving the EIT problem.

Variational Regularization

The most widely used strategy is the usage of variational regularization. In general, these methods can be captured by

$$\arg\min_{\boldsymbol{\sigma}_{rec}}\{D(\boldsymbol{v}, F(\boldsymbol{\sigma}_{rec})) + \eta R(\boldsymbol{\sigma}_{rec})\} \quad , \tag{2.15}$$

where $F(\boldsymbol{\sigma}_{rec})$ is a model that predicts the voltage measurements formed by the estimated conductivity distribution $\boldsymbol{\sigma}_{rec}$ and $D(\boldsymbol{v}, F(\boldsymbol{\sigma}_{rec}))$ is the data fidelity term, which measures the discrepancy between the observed voltages $\boldsymbol{v}$ and the data predicted by the model $F(\boldsymbol{\sigma}_{rec})$. In reality, $D(\boldsymbol{v}, F(\boldsymbol{\sigma}_{rec}))$ is often the L_2 norm, but it can be any other distance metric like the Kullback-Leibler Divergence. $R(\boldsymbol{\sigma}_{rec})$ is a regularization function. It imposes some desired behavior on $\boldsymbol{\sigma}_{rec}$. This can be a norm like the L_2 norm for Tikhonov regularization, a total variation term line in total variation regularization, or some incorporation of a priori knowledge of $\boldsymbol{\sigma}_{rec}$. In practice, equation (2.15) is solved through the GN method. An initial guess on $\boldsymbol{\sigma}_{rec}$ is applied to a model. The conductivity is updated according to $\boldsymbol{\sigma}_{rec}^{k+1} = \boldsymbol{\sigma}_{rec}^{k} + \alpha_k[-(\tilde{\boldsymbol{J}}^T\tilde{\boldsymbol{J}})^{-1}(\tilde{\boldsymbol{J}})D(\boldsymbol{v}, F(\boldsymbol{\sigma}_{rec}))]$ until some desired residual of equation (2.15) is reached. α_k is the step size for the k^{th} step, and $\tilde{\boldsymbol{J}}$ is the Jacobi matrix describing how much each measured voltage will change when a conductivity element is varied.

Two popular strategies in the literature of this type are Tikhonov and total variational regularization. The Tikhonov regularization, which can be stated as $\min_{\boldsymbol{\sigma}_{rec}}\{\|\boldsymbol{v} - F(\boldsymbol{\sigma}_{rec}))\|^2 + \eta\|\boldsymbol{K}\boldsymbol{\sigma}_{rec}\|^2\}$, where $\boldsymbol{L}$ is often the identity matrix, is probably the most commonly used one [VVK+98]. Typically, this nudges the solution towards smooth distributions of $\boldsymbol{\sigma}_{rec}$. Another popular strategy is total variation regularization. This can be stated as $\min_{\boldsymbol{\sigma}_{rec}}\{\|\boldsymbol{v} - F(\boldsymbol{\sigma}_{rec}))\|^2 + \eta\sum_i\sqrt{|\boldsymbol{K}_i|^2 + \beta}\}$. Here, $\boldsymbol{K}$ describes jumps in the conductivity distribution and $\beta \geq 0$ is a hyperparameter [BGAL09]. This strategy is a kind of L_1 regularization and encourages jumps in the conductivity through $\boldsymbol{K}$.

An example algorithm that uses machine learning approaches and is widely used is the Graz consensus Reconstruction algorithm for EIT (GREIT) algorithm, which trains a matrix to map a voltage difference to a conductivity difference [AAB+09]. Although not obvious, data-driven methods, like artificial neural networks (ANNs), are also part of the variational regularization methods.

Statistical Inversion

Most commonly, Bayesian statistics has been introduced to the statistical methods. In this framework, the inverse problem is recast as a form of statistical

inference from a distribution of unknown parameters [KKSV00]. The goal is to estimate the posterior distribution of the unknown parameters conditioned on the measured data. The posterior distribution is given by

$$p(\boldsymbol{\sigma}_{rec}|\boldsymbol{v}) = \frac{p(\boldsymbol{v}|\boldsymbol{\sigma}_{rec})p(\boldsymbol{\sigma}_{rec})}{p(\boldsymbol{v})} \quad . \tag{2.16}$$

Here, $p(\boldsymbol{v}|\boldsymbol{\sigma}_{rec})$ is the likelihood function, which represents the probability of observing the measurement given the conductivity distribution $\boldsymbol{\sigma}_{rec}$. This is often modeled as a Gaussian distribution with the help of a proper model that allows for calculating the voltage $\boldsymbol{v}$ given $\boldsymbol{\sigma}_{rec}$. $p(\boldsymbol{\sigma}_{rec})$ Represents the prior belief about $\boldsymbol{\sigma}_{rec}$. Popular choices are a Gaussian distribution, an L_1 prior, or a total variation prior. $p(\boldsymbol{v})$ captures the marginal likelihood; it can be understood as the model's probability. The estimation is performed through techniques like Markov chain Monte Carlo methods.

1 Initialize the Markov chain through an initial guess of $\boldsymbol{\sigma}_{rec}$

2 At each iteration k, propose a new conductivity distribution $\boldsymbol{\sigma}_{rec}^{k+1}$ from the proposed distribution $q(\boldsymbol{\sigma}_{rec}^{k+1}|\boldsymbol{\sigma}_{rec}^{k})$

3 Calculate the acceptance probability $a(\boldsymbol{\sigma}_{rec}^{k+1}|\boldsymbol{\sigma}_{rec}^{k}) = \min\{1, \frac{p(\boldsymbol{\sigma}_{rec}^{k+1}|\boldsymbol{v})}{p(\boldsymbol{\sigma}_{rec}^{k}|\boldsymbol{v})}\}$

4 Accept the proposed conductivity distribution $a(\boldsymbol{\sigma}_{rec}^{k+1}|\boldsymbol{\sigma}_{rec}^{k})$ or reject it and keep the current distribution $\boldsymbol{\sigma}_{rec}^{k}$

5 Repeat steps 2 to 4 until the Markov chain converges

Direct solutions Approaches

The direct solution approaches come from a purely mathematical perspective, and their development is closely linked to the Chaldéron problem. These approaches aim to directly calculate $\boldsymbol{\sigma}_{rec}$ from equation (2.13). Explaining this concept in general is nearly impossible due to the diverse nature of such potential strategies. In chapter 4, one such strategy, namely the D-Bar algorithm, will be explained in more detail. Another strategy that can be counted as a direct method is filtered back-projection. Although unrelated to rigorous math, it outputs a solution directly in its basic form. It evolves around projecting the impedance measurements along a simplified path that the current has presumably taken. The addition of all these measurements yields the reconstruction of the image. A filter step is often introduced to clean up the images and decrease the noise.

2.3.4 Gauss-Newton Algorithm

As the GN algorithm is used throughout the work and only a brief explanation of the general concept was given in section 2.3.3, a more detailed and in depth explanation is needed to properly understand the functionality of the algorithm.

The GN belongs to the class of variational regularization algorithms. It was one of the earlier algorithms used to recover the conductivity distribution from the boundary measurements.

Loss Function

The objective in EIT is to identify the conductivity distribution, denoted by $\boldsymbol{\sigma}_{rec}$, that minimizes the discrepancy between the measured voltages, v, and the voltages predicted by the forward model, $F(\boldsymbol{\sigma}_{rec})$. This is achieved while also incorporating a regularization term to stabilize the solution. The forward model, denoted by $F(\boldsymbol{\sigma}_{rec})$, is typically a finite element model, as it can be solved relatively quickly. The process for solving the model is discussed in more detail in section 3. The loss function can be formulated as:

$$\arg\min_{\boldsymbol{\sigma}_{rec}} \frac{1}{2}\|v - F(\boldsymbol{\sigma}_{rec})\|^2 + \frac{\eta}{2}\|\boldsymbol{K}\boldsymbol{\sigma}_{rec}\|^2. \tag{2.17}$$

The data fidelity term, which is represented by the expression $\|v - F(\boldsymbol{\sigma}_{rec})\|^2$, is used to assess the discrepancy between the observed voltages v and the predicted voltage $F(\boldsymbol{\sigma}_{rec})$. The regularization term, which is represented by the expression $\|\boldsymbol{K}\boldsymbol{\sigma}_{rec}\|^2$, is used to impose smoothness or other desired properties on the conductivity distribution $\boldsymbol{\sigma}_{rec}$. The regularization parameter, which is represented by the symbol η, is used to balance the fidelity term and the regularization term. Finally, the regularization matrix, which is represented by the symbol $\boldsymbol{K}$, is used to impose such properties directly on the conductivity distribution.

Importance of Regularization for Gauss Newton

Regularization is of paramount importance in EIT, for the following reasons:

- **Underdetermined system**: As $\boldsymbol{\sigma}_{rec}$ has more unknowns than the measurements provide, a regularization is in fact needed to provide a solution in the GN approach
- **Noise sensitivity**: big changes in conductivity lead to small changes in the boundary voltages. This means that noisy boundary voltages will produce big artifacts in the reconstruction. The regularization term dampens this effect and balances the noise resistance and the spatial resolution.

- **Imposing constraints**: More generally, the regularization term can be used to impose various constraints into the solution like, e.g., sparsity or smoothness.

Gauss-Newton iterative Scheme

The GN method is an iterative optimization technique employed to solve non-linear least squares problems. In the context of EIT, it is utilized to minimize the discrepancy between the measured and predicted voltages, while incorporating regularization to stabilize the solution. The GN update rule is expressed as follows:

$$\boldsymbol{\sigma}_{rec}^{k+1} = \boldsymbol{\sigma}_{rec}^{k} + \alpha_k \partial \boldsymbol{\sigma}^k \tag{2.18}$$

where α_k is the step size at iteration k and $\partial\boldsymbol{\sigma}$ is the update direction computed as:

$$\partial \boldsymbol{\sigma}^k = -(\tilde{\boldsymbol{J}}^T \tilde{\boldsymbol{J}})^{-1} (\tilde{\boldsymbol{J}}^T)(v - F(\sigma_{\text{rec}})), \tag{2.19}$$

where $\tilde{\boldsymbol{J}}$ is used to describe the sensitivity of a change in conductivity to a change in voltage. As a default initial guess, a often constant value is used. In this work, it is set to 1.

Jacobian Calculation

The Jacobian matrix, denoted by $\tilde{\boldsymbol{J}}$, represents a pivotal element in the GN algorithm. It is defined as:

$$\tilde{\tilde{\boldsymbol{J}}}_{i,j} = \frac{\partial v_i}{\partial \sigma_j}. \tag{2.20}$$

The voltage measurement on the i-th electrode, designated by v_i, is used to describe the voltage measurement. The conductivity at the j-th element of $\boldsymbol{\sigma}_{rec}$, designated by σ_j, is used to describe estimation of the conductivity of the j-th element. The Jacobian can be calculated using a variety of techniques, including direct perturbation, adjoint methods, and Fréchet derivatives [BCJ+17].

Regularization

The most popular regularization strategy in EIT is the Tikhonov regularization, which is the term $\frac{\eta}{2}\|\boldsymbol{K}\sigma_{\text{rec}}\|^2$ from equation (2.17). In the case of Tikhonov, the regularization matrix $\boldsymbol{K}$ is the identity matrix.

Summary

The GN algorithm is an iterative optimization technique employed to resolve non-linear least squares problems. It updates the estimate of the parameters by linearizing the non-linear model around the current estimate and solving the resulting linear least squares problem. The update rule involves computing the Jacobian matrix of the forward model and utilizing it to adjust the parameter estimates iteratively. Regularization is employed to stabilize the solution, particularly in ill-posed problems such as EIT, where it serves to mitigate the effects of noise and ensure the existence of a unique, stable solution.

2.3.5 Quantifying the Reconstruction Quality

When developing or using reconstruction techniques, it is crucial to know or judge their capabilities. Although at first glance using the root-mean-square error or the image correlation might seem useful, it is not the primary goal to guess the right values for $\boldsymbol{\sigma}_{rec}$, but rather the information gained from the images. In the end, the physician must be able to generate useful conclusions from a given reconstruction.

For this, metrics for the reconstruction quality have to be formulated and used. For their research on GREIT algorithm, Adler et al. developed six metrics, which capture different aspects of an algorithm's reconstruction [AAB+09]. The advantage of having multiple metrics over simpler single metrics like mean squared error or cross-correlation between a ground truth image and a reconstruction is that multiple different aspects of the reconstruction can be assessed.

The assesment places a small circular target into the medium at different positions and then calculates the metrics for each of the positions separately. From multiple of these calculations, the quality of the reconstruction algorithm can be assessed. The GREIT figure of merit (fom) were initially made for time-dependent reconstruction, which means that they revolve around the fact that the reconstruction has positive and negative values. This is not possible for time-independent reconstruction, as physically plausible values for the bioimpedance are always positive. Thus, the initial proposed GREIT fom must be adapted for time-independent reconstruction. The fom are formed as follows:

Let the EIT reconstruction be denoted as $\boldsymbol{\sigma}_{rec}$. Then the first step produces a reconstruction centered around zero with the help of

$$\boldsymbol{\sigma}_{eval} = \boldsymbol{\sigma}_{rec} - \boldsymbol{\sigma}_{\text{median}},$$

where $\boldsymbol{\sigma}_{\text{median}}$ is the median conductivity of the reconstruction $\boldsymbol{\sigma}_{rec}$. This step assumes that the median value of $\boldsymbol{\sigma}_{rec}$ can be regarded as a background. The choice of subtraction of the median $\boldsymbol{\sigma}_{\text{median}}$ over the calculated mean of

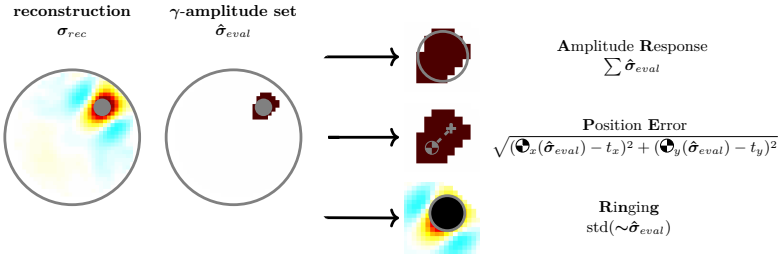


Figure 2.8: Visualization of the calculation of the GREIT fom for a target on the top right. To the very left the reconstruction $\boldsymbol{\sigma}_{rec}$, and in the middle the γ-amplitude set is visualized. To the right, the calculations of the fom can be seen.

$\boldsymbol{\sigma}_{rec}$ has two reasons. For a single target inside a homogenous domain Ω, the perfect reconstruction only has two values: the background and the target. Subtraction of the mean from $\boldsymbol{\sigma}_{rec}$ would lead to a negative background. This makes constructing the other steps more complicated and less easy to interpret. The second reason is that reconstruction is not guaranteed to give well-behaved reconstructions. Using $\boldsymbol{\sigma}_{\text{median}}$ is more robust to any outliers in the data. The other steps closely follow the definition of the original fom from Adler et al. [AAB+09]. The evaluation mask needs to be computed after shifting the target and background around zero. This can be done through a thresholding:

$$\sim\hat{\boldsymbol{\sigma}}_{eval} = \begin{cases} 1 & if\ \boldsymbol{\sigma}_{eval} < \gamma \cdot \min(\boldsymbol{\sigma}_{eval}) \\ 0 & else \end{cases}, \tag{2.21}$$

where $\boldsymbol{m}$ is the binary evaluation mask and $\gamma = \frac{1}{2}$ is the thresholding value. The exact value of γ is not critical. However, it is important to always use the same when comparing different techniques. Throughout this work, $\gamma = \frac{1}{2}$ holds true. Also, note that the inequality operator $<$ depends on whether the target conductivity is greater or less than the background. The inequality operator must be changed for targets with greater conductivity than the background. Values of $\boldsymbol{\sigma}$ inside the mask are referred to as $\hat{\boldsymbol{\sigma}}_{eval}$, while all values outside the mask are denoted as $\sim\hat{\boldsymbol{\sigma}}_{eval}$. With the help of the mask, all the fom can finally be calculated (an overview graphical representation of the calculations are presented in figure 2.8):

Amplitude Response (AR)

AR measures how well the EIT reconstruction can reproduce the correct amplitude of the conductivity changes within the area of the image. It can be calculated as

$$AR = \sum \hat{\boldsymbol{\sigma}}_{eval}. \tag{2.22}$$

Note that this definition deviates slightly from the original one, as the normalization part is missing. However, this normalization would require manual adjustment and is thus omitted. A constant AR (a standard deviation (*std*)) is considered the most important fom. This is because the reconstructed area of the test target should be the same for each position in the medium.

Position Error (PE)

PE measures the discrepancy between the actual position of the center of the target and its actual position. It is calculated as follows

$$PE = \sqrt{(\clubsuit_x(\hat{\boldsymbol{\sigma}}_{eval}) - t_x)^2 + (\clubsuit_y(\hat{\boldsymbol{\sigma}}_{eval}) - t_y)^2}, \tag{2.23}$$

$\clubsuit_x$ and $\clubsuit_y$ represent the x and y components of the center of mass (in this case, the conductivity is used as a weight), respectively. Meanwhile, t_x and t_y correspond to the actual x and y positions, known as the ground truth coordinates. The PE should be as low as possible and exhibit small variability. This is considered to be the second most important metric, as a variable PE can mislead in interpreting the reconstruction.

Ringing (RNG)

RNG captures the presence of artifacts in the reconstructed image; they often appear as bands of rings around the actual target. Throughout this work, it is defined as

$$RNG = \mathrm{std}(\sim\hat{\boldsymbol{\sigma}}_{eval}). \tag{2.24}$$

RNG should be low and uniform, as a low RNG shows low artifacts and is considered to be the third most important metric. Note that this RNG definition deviates from the original one from Adler et al., which was altered for ease of computation, but it still grasps the concept of the original metric [AAB+09].

In this work, the other metrics introduced by Adler et al. [AAB+09], like e.g. REsolution or Shape Deformation, are omitted, as the ones presented here capture the most important aspects of the reconstruction and make it easier to grasp the reconstruction quality.

2.4 Finite Element Method in EIT

The provided text discusses the application of the finite element method in EIT. It explains the motivation for using FEM, the process of meshing the domain, deriving the weak form of the Laplace equation and constructing the global solution. FEM is used to approximate solutions for complex geometries and conductivity distributions that are difficult to solve analytically. The method involves dividing the domain into simpler subdomains, choosing interpolation functions, deriving the weak form of the differential equation, constructing and solving the global system of equations, and analyzing the results. The text also describes the meshing process, the derivation of the weak form and the construction of the global solution matrix.

2.4.1 Motivation

Analytically solving the Laplace equation (2.13) may be possible for simple geometries and conductivity distributions, like e.g. the unit-disk with constant conductivity and sinusoidal voltage or current excitation. However, deviations from this simple setup make analytic solutions of equation (2.13) way more complicated or even impossible. Circular domains or homogeneous conductivity distributions do not occur in humans. The conductivity distribution and shape of the domain are way more complex. Solving this analytically is next to impossible. To conduct simulation studies, another approach had to be chosen. For this, the FEM was selected. FEM revolves around approximating the solution of a given differential equation (in this case, the Laplace equation) for a given geometry, conductivity distribution, and boundary conditions. To construct the approximate solution, the following steps have to be followed [ÖK18]:

- Divide the domain Ω into a set of simple-shaped subdomains (finite element mesh)
- Choose the proper interpolation functions (shape and basis functions)
- Derive the weak form of the differential equation
- Construct the global system of equations to solve for
- Enforce the desired boundary conditions
- Solve the global system of equations
- Analyze and use the computed results

In this work, the FEM simulations have been performed using the "Electrical Impedance Tomography and Diffuse Optical Tomography Reconstruction Software" (EIDORS) framework, which is a Matlab-based toolbox for EIT-related topics [AL06]. FEM is also vital for some reconstruction algorithms. The variational regularization strategies often rely on the calculation of the Jacobi matrix $\tilde{\boldsymbol{J}}$, which in turn can be done through FEM simulation.

2.4.2 Mesh Elements and Interpolation Functions

To solve the Laplace equation, the domain of interest (either 3D or 2D throughout this work) is partitioned into single elements. For a 2D domain, these elements are two-dimensional, and for a 3D domain, these elements are three-dimensional. Apart from this restriction, the shape can be arbitrary. In this work, triangles have been used for the 2D case, and tetrahedra have been used for the 3D case. This makes the meshing process faster, as it is easier to mesh these quite simple shapes [AC14], [Dan22]. The meshing was performed through Netgen in the EIDORS Matlab toolbox, which uses the Delaunay meshing algorithm [Sch97], [AL06]. Each domain element approximates the potential Φ only in its element. Collecting all elements then forms the approximated solution for Φ on the whole domain. This can be compared to a spline interpolation, where each spline element locally approximates an underlying function. As in a spline interpolation, each mesh element has an underlying function, forming the approximate solution. The most simple approximation function is a linear function. However, it tends to have a more significant error than more complex interpolation functions. Linear functions are easier to compute, and the interpolation error can be offset by having more elements in the mesh. To make the solution more accurate, it is essential to refine the mesh in places where the solution Φ changes rapidly. This is the case near current injecting electrodes; thus, the mesh is refined near all the electrodes in this work. The process of meshing is still more complex and has many nuances. Details on this topic can be found in [Lo14].

2.4.3 The weak form of the Laplace Equation

Given the Laplace equation (2.13) ($\boldsymbol{\nabla}\cdot(-\sigma\boldsymbol{\nabla}\Phi) = 0$) - also known as the strong form - one can derive the so-called weak form of it by multiplication of another function $v \in \mathcal{V}$ and integration over the domain Ω:

$$\int_{\Omega} v\boldsymbol{\nabla}\cdot(-\sigma\boldsymbol{\nabla}\Phi)\,d\Omega = 0 \quad \forall v \in \mathcal{V}, \tag{2.25}$$

where $\mathcal{V}$ is a suitable function space, which means that it has to satisfy, among other things, the appropriate Dirichlet boundary conditions. With the help of the Greens's identity and $\boldsymbol{\nabla} \cdot \left(\boldsymbol{A}\boldsymbol{B}^T\right) = \boldsymbol{B}(\boldsymbol{\nabla} \cdot \boldsymbol{A}) + (\boldsymbol{A}\boldsymbol{\nabla})\boldsymbol{B}$, one gets

$$\int_{\Omega} \boldsymbol{\nabla} \cdot (-v\sigma\boldsymbol{\nabla}\Phi)\, d\Omega - \int_{\Omega} \sigma\boldsymbol{\nabla}\Phi \cdot \boldsymbol{\nabla} v\, d\Omega = 0. \tag{2.26}$$

With the help of the divergence theorem, one gets

$$\int_{\Omega} \sigma\boldsymbol{\nabla}\Phi \cdot \boldsymbol{\nabla} v\, d\Omega = \int_{\partial\Omega} \sigma\boldsymbol{\nabla}\Phi \cdot \boldsymbol{n} v\, d\partial\Omega, \tag{2.27}$$

where $\boldsymbol{n}$ is the outward normal vector of the domain. Equation (2.27) finally is the weak form of the Laplace equation. The order of the equations of the weak form is one lower than the original equation. However, it is noted that the solution to Φ in the weak form is mathematically exactly equal to the original solution of Φ. The right-hand side represents the boundary conditions. In each element Ω_e of the mesh, the true potential Φ is approximated by the potential Φ^e through basis functions $\boldsymbol{\Theta}_i$:

$$\Phi \approx \Phi^e = \sum_i \Phi_i^e \boldsymbol{\Theta}_i^e, \tag{2.28}$$

where Φ_i^e are the unknown coefficients to be determined and $\boldsymbol{\Theta}_i^e$ depends on the element type and desired approximation function. The weak form of equation (2.27) has to hold for each element. Thus, equation (2.28) can be plugged into equation (2.27), thus gaining the elementwise weak form:

$$\sum_j \Phi_i^e \underbrace{\left(\int_{\Omega_e} \sigma\boldsymbol{\nabla}\boldsymbol{\Theta}_i^e \cdot \boldsymbol{\nabla}\boldsymbol{\Theta}_j^e\, d\Omega_e\right)}_{A_{i,j}^e} = \underbrace{\int_{\partial\Omega} \sigma\boldsymbol{\nabla}\Phi_i^e \cdot \boldsymbol{n}\boldsymbol{\Theta}_i^e\, d\partial\Omega_e}_{b_i^e} \quad i \in \{1, ..., n^e\}, \tag{2.29}$$

where n^e denotes the number of nodes in an element. For v the interpolation function of the element Φ was used. This technique is called the "Garlekin" method, but one can also use other functions for v. Notably, the right-hand side term is non-zero only for elements where the electrodes are part of the element.

2.4.4 Global Solution

To construct the solution in each element from equation (2.29), the unknown coefficients Φ_i^e need to be calculated. The equation system can be expressed as $\tilde{\boldsymbol{A}}^e \boldsymbol{\Phi}^e = \boldsymbol{b}^e$. $\tilde{\boldsymbol{A}}$ is an $n^e \times n^e$ matrix and $\boldsymbol{b}$ is a $n^e \times 1$ vector. Each element in $\tilde{\boldsymbol{A}}$ is defined as $\tilde{A}^e_{i,j} = (\int_{\Omega_e} \sigma \boldsymbol{\nabla} \boldsymbol{\Theta}^e_i \cdot \boldsymbol{\nabla} \boldsymbol{\Theta}^e_j \, d\Omega_e)$, while each element of $\boldsymbol{b}$ can be expressed as $b^e_i = \int_{\partial\Omega} \sigma \boldsymbol{\nabla} \Phi^e_i \cdot \boldsymbol{n} \boldsymbol{\Theta}^e_i \, d\partial\Omega_e$.

The global matrix can be assembled after constructing $\tilde{\boldsymbol{A}}^e$ and $\boldsymbol{b}^e$ for each element. Each element has n^e nodes, which are locally defined. To assemble the global matrix $\tilde{\boldsymbol{A}}$, the mapping from the local nodes i of each element to the global nodes i_g is needed. Thus, each element of $\tilde{\boldsymbol{A}}$ is defined as $\tilde{A}_{i_g,j_g} \leftarrow \tilde{A}_{i_g,j_g} + \tilde{A}^e_{i,j}$ and respectively for $\boldsymbol{b}$ with $b_{i_g} \leftarrow b_{i_g} + b^e_i$. Nearly all the global nodes have more than one local node mapping to them. This is simply because the elements in the mesh are connected. Boundary conditions can then be applied to the right-hand side vector $\boldsymbol{b}$. These boundary conditions are not included in $\tilde{\boldsymbol{A}}$; this is very useful in the case of EIT, as each stimulation and measurement $\tilde{\boldsymbol{A}}$ can be reused, and only the right-hand side needs to be updated. Solving the global system $\tilde{\boldsymbol{A}}\boldsymbol{\Phi} = \boldsymbol{b}$ yields the approximated solution and gives the potential distribution for each element.

2.5 Summary

EIT is a non-invasive imaging technique that reconstructs the conductivity distribution within a domain. This is a particularly useful technique in medical applications, as different tissues and their states exhibit distinct conductivities. This makes EIT valuable for monitoring conditions such as acute respiratory distress syndrome or detecting cancer. EIT involves placing electrodes on the surface of the domain to inject current and measure voltage. The most common pattern is the adjacent-adjacent (skip-0-0) pattern, where current is injected between two neighboring electrodes, and voltages are measured between other neighboring electrodes.

Although theoretically optimal patterns like the trigonometric pattern exist, they are impractical due to hardware complexity and measurement errors.

The chapter has explained the Maxwell equations and their simplifications for EIT, leading to the Laplace equation for potential distribution. Mathematically, the EIT problem is an inverse problem, which aims to determine the conductivity distribution from boundary measurements. This problem was first formalized by Calderón in 1980. It is non-linear and ill-posed, which means that it may not have a unique, stable solution and is sensitive to noise. There are

several solution strategies for this problem, including variational regularization, statistical inversion and direct solution approaches. Variational regularization involves minimizing a loss function that balances data fidelity and regularization terms to stabilize the solution. Statistical inversion employs Bayesian methods to estimate the posterior distribution of the unknown parameters. A direct solution approach aims to calculate the conductivity distribution directly, utilizing mathematical techniques such as the D-Bar algorithm.

FEM can be employed to approximate solutions to the Laplace equation for complex geometries and conductivity distributions. This process involves meshing the domain, selecting interpolation functions, deriving the weak form of the differential equation, and solving the global system of equations. Metrics such as AR, PE, and RNG can be employed to assess the quality of EIT reconstructions, ensuring that they provide useful and accurate information for medical diagnosis. This chapter has established the foundation for comprehending EIT's principles, challenges, and methodologies, emphasizing its potential and limitations in medical imaging.

3 Artificial Neural Networks for time-independent Reconstructions

The chapter delves into the application of Artificial Neural Networks (ANNs) for EIT, highlighting their potential to address the non-linear and ill-posed nature of EIT's inverse problem. It begins with a historical overview of ANNs, tracing their origins and fundamental principles. The discussion then moves to the architecture of ANNs, detailing components such as neurons, fully connected layers, convolutional layers, dropout layers, and activation functions. The proposed ANN architecture for EIT reconstruction is introduced, emphasizing innovative features like input transformation and convolutional blocks. The chapter also covers the design and implementation of the loss function and training process, followed by an evaluation of the ANN's performance using various data sets. Additionally, the generation of training data through FEM method simulations is discussed.

3.1 Basics of Artificial Neural Networks

The concept of ANNs has been the subject of intense interest among researchers and scientists for decades. Its origins can be traced back to the pioneering work of neurophysiologist Warren McCulloch and mathematician Walter Pitts in 1943 [MP43]. They developed a simplified model of a neuron, now known as the McCulloch-Pitts neuron, which fundamentally operates by summing its inputs and producing an output of one if the sum surpasses a certain threshold, and zero otherwise. This model, despite its simplicity, established the foundation for understanding the operational principles of neurons in the human brain. However, due to its inability to fully encapsulate the brain's complexity, the McCulloch-Pitts neuron model received more attention in the emerging field of artificial intelligence than in neuroscience itself [MP43].

The architecture of an ANN is constructed from layers of these simplified neuron models. When neurons within a layer are interconnected to neurons in subsequent layers, or directly to the input data, the resulting structure is termed an ANN. This hierarchical arrangement of neurons and layers enables the network to approximate complex functions, effectively mapping input data to desired outputs. The term "deep learning" emerges from the practice of employing multiple layers within a network to build more profound and capable models. Nowadays, the utilization of neural networks spans a diverse range of fields, exemplifying their versatility and potency. Search engines, for instance, employ neural networks to refine and enhance search results, thereby tailoring them to user queries in a more effective manner. A notable achievement in the realm of competitive games was accomplished by Google DeepMind, which

developed a deep neural network that triumphed over the world's top players in the game of Go. This demonstrated the potential of neural networks in complex strategic applications, as evidenced by [SSS+17]. Furthermore, in the medical field, deep neural networks have demonstrated remarkable capabilities, such as matching the diagnostic accuracy of dermatologists in identifying skin cancer. This illustrates their potential to revolutionize healthcare and diagnostics [EKN+17]. This evolution of neural networks from their conceptual inception to their current state as pivotal tools in technology and medicine underscores their significance in advancing artificial intelligence and computational models that mimic the intricacies of the human brain.

3.1.1 The Neuron / fully connected Layer

The fundamental operation of a neuron within a neural network is the processing of an input to generate an output. This process is encapsulated by the following mathematical expression:

$$\boldsymbol{z} = \sigma(\boldsymbol{x}\boldsymbol{W} + \boldsymbol{b}) \tag{3.1}$$

In this context, the symbol $\boldsymbol{x}$ denotes the input vector to the neuron, the symbol $\boldsymbol{W}$ represents the weight matrix associated with the neuron, the symbol $\boldsymbol{b}$ represents the bias vector, the symbol σ is the activation function, and the symbol $\boldsymbol{z}$ is the resultant output of the neuron. For a clearer comprehension of the operation of a neuron, please refer to Figure 3.1.[1]

3.1.2 Backpropagation

The loss function is a crucial component in training ANNs. The loss function quantifies the discrepancy between the predicted output of the network and the actual target value, thereby providing a measure of the model's performance. The objective of training an ANN is to minimize the loss function by adjusting the weights and biases of the network. A common loss function used in regression problems is the Mean-Squared Error (MSE), defined as:

$$\text{MSE} = \frac{1}{2N} \sum_{\text{N}} (\boldsymbol{Y} - \boldsymbol{Y}')^2, \tag{3.2}$$

where N is the number of training examples, $\boldsymbol{Y}$ is the actual output (ground truth), and $\boldsymbol{Y}'$ is the predicted output of the network. In order to minimize the

[1] Note that the figure only represents a scalar output for explanatory purposes. In reality the output can be a vector, however the mathematical operations for each element are the same as in the scalar case

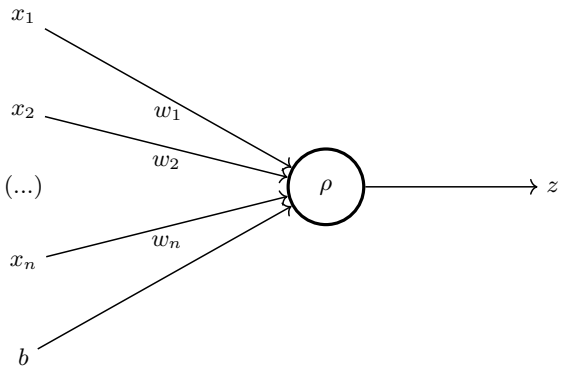


Figure 3.1: A simple neuron is depicted below. The inputs are weighted by the weights w, and then summed up with a bias. The activation function ρ is able to add non-linearity to the output.

loss function and improve the network's performance, the weights and biases are iteratively updated using an optimization algorithm such as gradient descent. The backpropagation algorithm is employed to efficiently compute the gradients of the loss function with respect to the weights and biases. The weight update rule for a weight w in layer l at position (i, j, c) and iteration t is given by:

$$w^{\mathrm{l}}_{\mathrm{t,i,j,c}} = w^{\mathrm{l}}_{\mathrm{t-1,i,j,c}} - \eta \frac{\partial \mathrm{MSE}}{\partial w^{\mathrm{l}}_{\mathrm{t-1,i,j,c}}}, \tag{3.3}$$

where the learning rate, denoted by the symbol η, determines the step size of the weight update. More advanced optimization algorithms, such as Adaptive Moment Estimation (Adam), combine the momentum method with adaptive learning rates for each parameter [KB14a]. The Adam update rule is given by:

$$
\begin{aligned}
m^{\mathrm{l}}_{\mathrm{t,i,j,c}} &= \beta_1 m^{\mathrm{l}}_{\mathrm{t-1,i,j,c}} + (1-\beta_1)\frac{\partial MSE}{\partial w^{\mathrm{l}}_{\mathrm{t-1,i,j,c}}},\\
v^{\mathrm{l}}_{\mathrm{t,i,j,c}} &= \beta_2 v^{\mathrm{l}}_{\mathrm{t-1,i,j,c}} + (1-\beta_2)\frac{\partial^2 \mathrm{MSE}}{\partial^2 w^{\mathrm{l}}_{\mathrm{t-1,i,j,c}}},\\
\hat{m}^{\mathrm{l}}_{\mathrm{t,i,j,c}} &= \frac{m^{\mathrm{l}}_{\mathrm{t,i,j,c}}}{1-\beta_1^{\mathrm{t}}},\\
\hat{v}^{\mathrm{l}}_{\mathrm{t,i,j,c}} &= \frac{v^{\mathrm{l}}_{\mathrm{t,i,j,c}}}{1-\beta_2^{\mathrm{t}}},\\
w^{\mathrm{l}}_{\mathrm{t,i,j,c}} &= w^{\mathrm{l}}_{\mathrm{t-1,i,j,c}} - \frac{\eta}{\sqrt{\hat{v}^{\mathrm{l}}_{\mathrm{t,i,j,c}}}+\epsilon}\hat{m}^{\mathrm{l}}_{\mathrm{t,i,j,c}},
\end{aligned}
$$

where the first and second moment estimates, denoted by m and v, respectively, are used to compute the hyperparameters, β_1 and β_2. These hyperparameters control the decay rates. The constant, ϵ, is used to maintain numerical stability. The weights and biases are updated iteratively using the gradients computed by the backpropagation algorithm and an optimization method, such as Adam. This process enables the ANN to learn and minimize the loss function, thereby improving its performance on the given task. The selection of the loss function, optimization algorithm, and hyperparameters can have a significant impact on the training process and the final performance of the model.

3.1.3 Weight Initialization

The initialization of weights is a crucial step in the setup of a neural network for training. The choice of initial weights can significantly impact the convergence and learning speed of the network. Several studies have demonstrated that the manner in which the initial weights are defined plays a vital role in the network's performance [NW90] [YC00].

One might consider setting all the weights to zero as a simple approach. However, this naive initialization would lead to zero gradients, preventing the network from learning any weights other than zero, effectively stalling the training process. Similarly, initializing all the weights with a constant non-zero value would still impede the network's capacity to adapt appropriate weights, as every neuron within a layer would possess identical gradients and develop the same weights, including in convolutional layers. The most easy method for initializing a neural network is through random initialization; however, the selection of the underlying distribution is of paramount importance and should be

tailored to the specific layers and their corresponding activation functions. A common approach is to sample weights from a normal distribution with a fixed variance, such as $\sigma^2 = 0.01$. While this method is superior to the previously mentioned ones, there is still room for improvement.

Glorot and Bengio proposed an initialization method with the objective of mitigating the exploding/vanishing gradients problem. This refers to the issues of gradients becoming either too small (vanishing), which causes the network to stop learning, or too large (exploding), which prevents the network from reaching a minimum [BSF94]. However, their assumption does not hold true for the Rectified Linear Unit (ReLU) activation function (for more details see section 3.1.4). To address this issue, a modified version of the He et al. (2015) initialization method was employed [HZRS15a]. The initialization is based on the propagation of variances across different layers during the backpropagation algorithm. When considering the derivative of a layer, it can be shown that the corresponding variance of that layer is a function of the variances of all the following layer's weights. This is given by the following equation:

$$Var(\Delta x_{\mathrm{l}}) = Var(\Delta x_{\mathrm{L}+1})(\prod_{\mathrm{l}'=\mathrm{l}}^{\mathrm{L}} \frac{1}{2} n_{\mathrm{l}} Var(w_{\mathrm{l}'})),$$

The notation n_{l} denotes the number of inputs to layer l, L represents the total number of layers until the end of the network, and $w_{\mathrm{l}'}$ represents the weights of the corresponding layer. In order to maintain a steady gradient flow, it is necessary to ensure that the variance of the weights, denoted by $Var(w_{\mathrm{l}} = 1)$, is equal to one for all layers in the network, L. Consequently, the weights are initialized using a zero-mean Gaussian distribution with a standard deviation (std) of $\sqrt{2/n_{\mathrm{l}}}$. By carefully selecting the appropriate weight initialization method, such as the initialization for ReLU activation functions, neural networks can be set up for more efficient training and improved convergence, ultimately leading to better performance on the given task.

3.1.4 Components of an ANN

Convolutional Layer

Convolutional layers were introduced to overcome the limitations of fully connected layers, particularly in the context of image processing. One of the first neural networks to use convolutional layers was LeNet-5, developed by Yann LeCun. The primary goal of LeNet-5 was to classify 32×32 images of handwritten digits into their corresponding numerical values [LBBH98].

The concept of convolutional layers was inspired by the seminal work of Hubel and Wiesel in 1959, where they studied the visual cortex of cats [HW59].

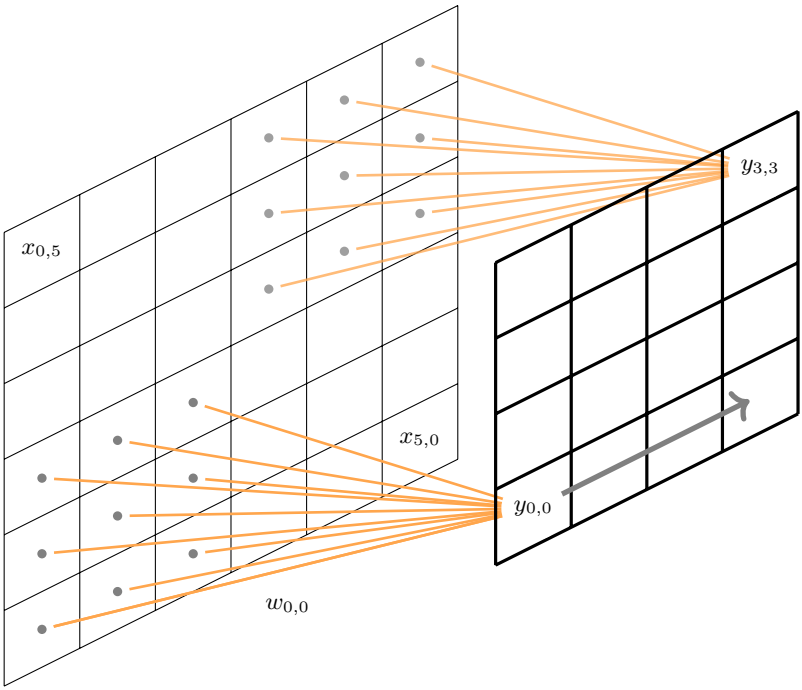


Figure 3.2: Example of two-dimensional convolution. The filter kernel is moved row by row through the input matrix $\boldsymbol{X}$ (to the left). In turn, the output matrix $\boldsymbol{Y}$ (to the right) becomes smaller.

Their research showed that certain neurons in the cat's brain were sensitive to certain shapes and patterns. This discovery laid the foundation for the development of convolutional layers in ANNs. In a convolutional layer, each feature map is designed to detect specific local patterns or shapes within the input image. While a single convolutional layer can only capture primitive features, a hierarchical arrangement of convolutional layers allows the network to learn increasingly complex and abstract representations of the input data.

The operation of a convolutional layer can be conceptualized as moving a filter kernel across the input matrix, similar to shining a flashlight on the image. At each position, the filter kernel, represented as a matrix of learnable weights, is multiplied element-wise by the corresponding region of the input.

The resulting products are summed to produce a single value in the output feature map. This process is repeated for each position of the filter kernel to produce a complete output feature map. Figure 3.2 illustrates this concept using a simple example of a 3×3 filter kernel applied to a 6×6 input matrix. The output of the convolution is smaller in dimension compared to the input. If the output shall have the same dimensions as the input, a "padding strategy" has to be applied. This means that at the borders of the input values are inserted to expand the dimensions. For this there are different strategies, e.g., zeros. Another strategy is the so-called "circular padding". "Circular padding", also known as "wrap-around padding" or "periodic padding", is a technique used in convolutional neural networks to preserve the rotational invariance property and overcome the limitations of convolutional neural networks in detecting features at the edges of the input matrix due to the finite size of the convolution kernel. In this method, the input matrix is padded by replicating the values from the opposite sides of the matrix, allowing the convolution operation to be performed on the edges of the matrix without losing information. To apply "circular padding", the input matrix is expanded by appending the values from the opposite sides of the matrix to the edges. This ensures that the convolution kernel can access the necessary information from the surrounding regions, even at the edges of the matrix, allowing for more effective feature extraction.

By exploiting local connectivity and weight sharing, convolutional layers significantly reduce the number of parameters compared to fully connected layers. This reduction in the number of parameters not only reduces memory requirements, but also improves the network's ability to learn translation-invariant features. In addition, the sparse connectivity of convolutional layers allows for efficient computation, resulting in faster training and inference times.

The hierarchical structure of convolutional neural networks, with successive layers capturing increasingly complex patterns, has proven highly effective in various computer vision tasks such as object recognition, image segmentation and face recognition. The success of convolutional layers has revolutionized the field of computer vision and has become a fundamental building block in modern deep learning architectures.

Fully connected Layer

While fully connected layers were the first type of layers used in neural networks and are still used in certain architectures, they have some limitations, particularly when dealing with image-related tasks. However, despite these drawbacks, fully connected layers remain useful in many scenarios and continue to play an important role in modern neural networks. One of the main disadvantages of fully connected layers is that the weight matrix can become

very large. In a fully connected layer, every input is connected to every neuron in that layer. If the layer preceding the fully connected layer has n neurons, and the fully connected layer itself has m neurons, the weight matrix will have a dimensionality of $n \times m$. When processing images, which are typically large, this can lead to significant memory consumption. In addition, the weights of the fully connected layers themselves consume a significant amount of memory. As a result, the required computing power increases as each weight needs to be processed. Despite these limitations, fully connected layers still offer valuable advantages in neural network architectures. They are particularly useful in the final stages of a network, where they can help to capture global relationships and make decisions based on the features extracted by previous layers. Fully connected layers allow signals from different parts of the input to be mixed, allowing the network to consider the entire input when making predictions. Fully connected layers are also easier to implement and have been extensively studied and optimized over the years. They are well suited to tasks where the spatial structure of the input is less important, such as natural language processing or tabular data analysis.

Dropout Layer

Overfitting is a common challenge in deep learning, and occures if a network becomes too specialized to the training data and fails to generalize well to unseen examples. In this scenario, the ANN's weights essentially memorize the training data, resulting in excellent performance on the training set but poor performance on new, unseen data. To mitigate this problem, Srivastava et al. introduced the concept of "dropout" in their paper [SHK+14].

Dropout is a regularization technique that aims to prevent overfitting by randomly deactivating neurons or filter kernels (in the case of convolutional layers) during the training phase. The activation state of each neuron or filter kernel follows a Bernoulli distribution with probability p. The authors draw an analogy to genetics, suggesting that this technique mimics the concept of genetic diversity and robustness. By randomly deactivating neurons during training, the remaining active neurons are forced to produce meaningful outputs as a subset of the original network. This encourages each neuron to learn more robust and generalized features, rather than relying on the presence of specific neighboring neurons. As a result, the network becomes more resilient and able to work effectively with different subsets of neurons, improving its ability to generalize to unseen data.

However, during the inference phase, all neurons are typically active, as the goal is to utilize the full capacity of the trained network. This mismatch between the training and inference configurations can lead to a bias in the net-

work's output. When all neurons are active, they tend to produce larger values compared to the training scenario where only a subset of neurons was active at any given time. To compensate for this effect, and to ensure consistency between training and inference, the outputs of all neurons are scaled by the probability p used during training.

Activation function

In an ANN the activation function is used to add non-linearity. Without it, the ANN only learns linear functions. There are various types, including e.g. sigmoid, tanh or swish. PReLu is an activation function that extends the Rectified Linear Unit (ReLU) by introducing a learnable parameter. In PReLU, the slope for negative inputs is not fixed, but is learned during the training process [HZRS15b]. The PReLU activation function is defined as follows

$$f(x_i) = \begin{cases} x_i, & \text{if } x_i > 0 \\ \alpha_i x_i, & \text{otherwise} \end{cases},$$

where x represents the input and α is a learnable parameter that controls the slope for negative inputs. A visualization of PReLU The main benefits of PReLU are:

- Addition of non-linearity
- Additional flexibility due to the learnable parameter
- Gradients for $x_i < 0$ can be computed

Throughout this work, the PReLU was used.

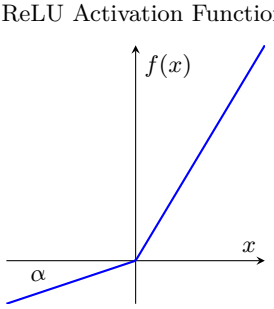


Figure 3.3: Example of the PReLU activation function

3.2 Structure of the proposed Artificial Neural Network

This section discusses the motivation and structure of using an ANN for EIT reconstruction, a challenging non-linear, ill-posed inverse problem. Traditional methods like the GN algorithm are slow and prone to artifacts, while ANNs offer faster evaluations, better noise handling, and improved reconstruction by capturing complex system behavior. The next section details the ANN architecture, including input transformation, convolutional and fully connected layers, and the training loss function, aiming to enhance reconstruction quality with fewer training examples.

3.2.1 Motivation

As elaborated in chapter 2, EIT is a non-linear ill-posed inverse problem. Traditional variational bases regularization techniques like the GN method have the drawback, that they produce ringing artifacts in the reconstruction and can take much time to come up with a solution.

This makes an ANN a good candidate for the usage in EIT reconstruction. ANNs are well-known for their capability of capturing complex non-linear relationships between the data and the output[2]. They find wide usage in many different areas of application. They include computer vision tasks like object detection or image segmentation, natural language processing for translation or text summarization, speech recognition for speech-to-text conversion or speaker identification and many other applications which have not been feasible in past decades [ATY+18].

Only recently, ANNs have emerged in the field of EIT. The main potentials gain in using ANNs for reconstruction in EIT are the following:

- Capturing the highly non-linear nature of the relationship between the impedance measurements and the underlying conductivity distribution
- Learning non-linear filters for the input voltage data to overcome susceptibility to noise
- Potentially faster evaluation compared to iterative reconstruction techniques
- Incorporation of system information in the structure or training data

[2] Compared to the Gauss Newton approach, ANNs are able to better capture more non-linearity. The GN algorithm linearizes the problem during its iterations. Thus, it implicitly assumes a weaker non-linearity, as the linearization in each of the steps must be justified.

- Reduction of reconstruction artifacts

Although in the literature there have been ANNs proposed for reconstruction, they lack some desired properties. Kłosowski et al. [KR17] proposed a neural network for EIT reconstruction. However, this network is only able to output single reconstruction targets and does not have the ability to recover more complex conductivity distributions. Hamilton et al. [HH18] proposed a neural network, which improved traditional reconstructions, thus not deploying ANNs to its full potential. Hu et al. proposed an ANN, which leveraged rotational symmetry, but needed calibration data to properly function [HLY19].

3.2.2 Architecture

In the choice of the architecture, the desired capabilities of the network can be incorporated. A low number of trainable parameters, as well as the incorporation of system behavior (which can go hand in hand), can greatly improve the reconstruction quality while simultaneously drastically reduce the required number of training examples. The proposed structure of the ANN can be found in Figure 3.4.

Input and Electrical Impedance Map (EIM) The first transformation happens right at the beginning, where the vector of 208 measured voltages from the adjcent-adjacent pattern is converted into a 16×16 matrix. Each row represents an injection pair, while each column represent a measurement pair (this is visualized in Figure 3.5). This has the advantage that the feature extraction can be done through two-dimensional convolutions, which in turn saves trainable weights, while at the same time making the feature extraction rotational invariant. As a rotation in the conductivity distribution results in a translatory motion of the whole input voltages along the diagonal in the input EIM.

Convolutional Layers The convolutional layers extract features necessary for the reconstruction step. The convolutional blocks (marked as “conv” in Figure 3.4) are composed of five components:

1. Droput-Layer
2. Circular-Padding
3. 2D-Convolution
4. PReLu

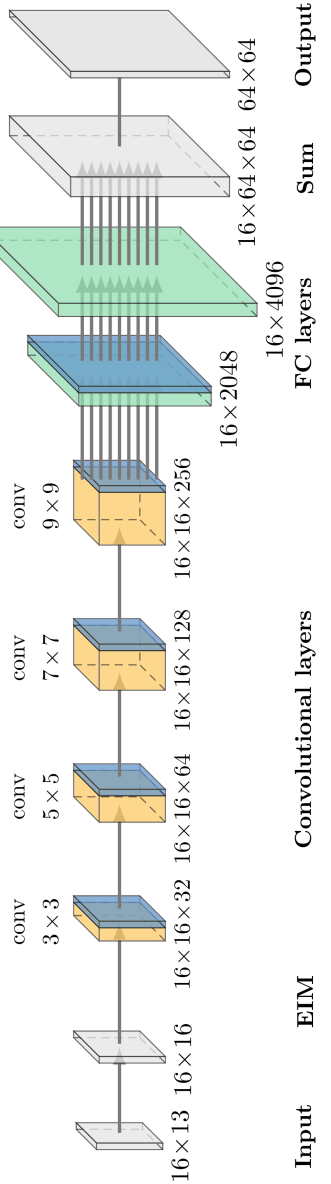


Figure 3.4: Structure of the proposed ANN from Rixen et al. [REH+22]

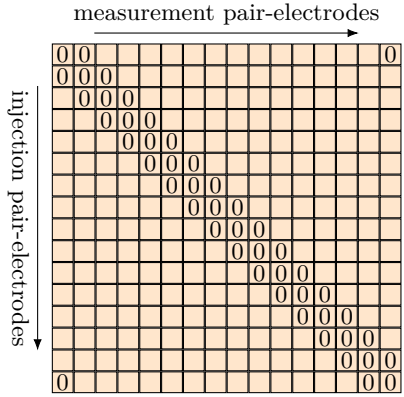


Figure 3.5: A 16×16 arrangement of the Electrical Impedance Map (EIM) from an adjacent injection pattern. The zeros represent values that are not collected in the adjacent measurement mode because at least one electrode is used for current injection.

5. Layer Normalization

Fully Connected Layers and Summation The Fully Connected layers (FC), referred to as "FC layers" in Figure 3.4, play a crucial role in the reconstruction process. Typically, these layers are computationally intensive due to their dense connections with each output from the previous layer. However, when considering the circular domain of a tank or a pig, the physics remains consistent from the perspective of each injection. To exploit this rotational invariance, instead of flattening the output after the last convolution, the first dimension representing injections is preserved. The fully connected layer is then applied 16 times, once for each stimulation. This approach allows a significant reduction in the number of weights in the final stage, saving $\frac{15}{16}$ of the total weights. Once the layers are fully connected, the feature maps are transformed into a $16 \times 64 \times 64$ tensor, where each injection has its own 64×64 reconstruction of conductivity. Finally, to fuse all the reconstructions together, the 16 images corresponding to each injection are summed element-wise, resulting in the final reconstruction that incorporates information from all the injections.

3.2.3 Loss Function

The loss function plays a crucial role in ensuring convergence of the ANN. As the conductivities expected in the thorax region of a human or a pig may lie orders of magnitude apart, the mean squared logarithmic error is used. It is defined as

$$\mathcal{L}_{MSLE} = \frac{1}{N}\sum(\log(\boldsymbol{Y}+1) - \log\big(\boldsymbol{Y'}+1\big))^2,$$

where $\boldsymbol{Y}$ is the desired output of the ANN[3] and $\boldsymbol{Y'}$ is the actual output of the ANN.

In classical EIT reconstruction algorithms, "Total Variation regularization" can be used to denoise images. It is a denoising technique that preserves sharp edges, thus keeping rich detail in the output. To further refine the ANN output total variation was added and can be stated as

$$\mathcal{L}_{TV} = \sum_{\mathrm{i,j}} |\boldsymbol{Y'}_{\mathrm{i+1,j}} - \boldsymbol{Y'}_{\mathrm{i,j}}| + |\boldsymbol{Y'}_{\mathrm{i,j+1}} - \boldsymbol{Y'}_{\mathrm{i,j}}|.$$

Another factor that can enhance the performance of an ANN is the concept of L2-weight-regularization. It encourages weights to be close to zero, which leads to a simpler model, that will be able to generalize better. This can be stated as

$$\mathcal{L}_{\hat{\omega}^2} = \sum_{\mathrm{i}=1}^{\mathrm{N}} \hat{\omega}_{\mathrm{i}^2}\,.$$

The total loss function was composed of all three terms. This leads to the following total loss function

$$\mathcal{L}_{total} = \mathcal{L}_{MSLE} + \lambda_1 \cdot \mathcal{L}_{TV} + \lambda_2 \cdot \mathcal{L}_{\hat{\omega}^2} \tag{3.4}$$

with $\lambda_1 = 0.1$ and $\lambda_2 = 1{\cdot}10^{-6}$, which are parameters to balance the influence of the regularization components. The ANN was trained with the Adam optimizer using TensorFlow [KB14b], [AAB+15]. Additionally, the learning rate was reduced by 70% whenever the loss reached a plateau.

3.3 Evaluation

This section describes the evaluation and training of an ANN designed for EIT. The evaluation includes simulations using FEM data, performance under noisy conditions and real data from a circular EIT tank and an experimental pig

[3] This is not directly $\boldsymbol{\sigma}$, but rather the "image" version of it. Thus, it also includes parts of the outside of the somain Ω

study. The training data, simulated primarily for cost-effectiveness, involves the creation of a cylindrical FEM model with different base shapes and transformations to ensure different conductivity distributions. Noise modelling and data augmentation techniques such as rotation and α-blending (see 3.4.5) were used to improve the generalization capabilities of the ANN.

Simulation Data

To evaluate the performance of the proposed ANN, FEM was first utilized to simulate data that the network had not encountered during training. Multiple enclosures with varying conductivities were simulated, and the enclosure was positioned such that it moved from the center of the domain towards the outer boundary. This setup simulated a cucumber in a saline water tank. The reconstructions obtained from the ANN were compared with those from the GN algorithm. For the hyperparameter selection of the GN algorithm, the L-curve criterion was initially employed, but did not yield usable results. This is attributed to the reference-free reconstruction approach, which destabilizes the EIT problem compared to differential EIT. Consequently, multiple sweeps of the hyperparameters were performed to iteratively narrow down the optimal values.

Performance under noisy FEM Data

Secondly, the noise performance of the ANN and GN was compared on a FEM data sample. For this evaluation, an enclosure near the boundary was simulated, and the Signal-to-Noise-Ratio (SNR) was incrementally decreased from 200 to 5. The SNR is defined as $SNR = \frac{\|\text{signal}\|}{\|\text{noise}\|}$. The GN reconstructions are provided for comparison. For this, the EIDORS function *add_noise* was used, which adds noise according to

$$noise = \mathcal{N}(0, 1) \tag{3.5}$$

$$v_{noisy} = v_{original} + noise \cdot \frac{\|v_{original}\|_2}{\|noise\|_2} \cdot \frac{1}{SNR}. \tag{3.6}$$

Tank Data

To further assess the performance, data acquired from a circular EIT tank with a diameter of 28 cm and 16 equidistantly attached electrodes was utilized. The tank was filled with a 0.9 % saline solution, and a pickle with a circumference of 4.5 cm served as the target. The pickle was moved from the center towards one electrode in nine steps, with the final position being 1 cm in front of the

electrode. The measurements were performed using the EIT evaluation kit 2 (Draeger EEK2, Draeger Medical GmbH).

Pig Data

Finally, an impression of the performance of the ANN on real-world data obtained from an experimental pig trial using a clinical EIT device (Draeger Pulmo Vista 500, Draeger Medical GmbH) is given. During the trial, eight anesthetized and tracheotomized pigs were positioned in a supine position, and CT measurements at the position of the electrode belt were taken. In the data sample used, two measurement points from a single healthy pig within a time span of approximately 30 seconds were utilized. As there is no ground truth regarding the conductivity distribution, two images will be presented. The first image shows the mean conductivity over an entire breathing cycle, while the second displays the *std* over the same cycle. A CT image will be provided as a background reference to facilitate a qualitative assessment of the reconstruction quality. The absolute GN algorithm did not yield meaningful results after a thorough hyperparameter sweep and was therefore not included as a reference.

3.4 Training Data

Typically, training data for an ANN is picked from the real world. In the case of EIT this cannot be done realistically, due to the inherent limited spatial resolution of EIT. Magnetic resonance EIT could resolve this problem, as it allows the visualization of the injected currents through an MRI scan [SJAH91]. Thus, the spatial resolution is far greater than in normal EIT. However, though this process offers a very high spatial resolution, nearly all the benefits are lost and most importantly, it would be very expensive to build a suitable data set for training an ANN.

Thus, for cost-efficiency reasons, the training data used to train the proposed ANN has been purely simulated. However, this also has many fallacies which can worsen the reconstruction capabilities on real world data.

3.4.1 FEM Model Shape

At first, a base model for the FEM simulation has to be chosen. If possible, no specific shape of the FEM model would be chosen. However, as FEM simulations require a precise definition of the geometry, in this work a circular tank was chosen. Two factors support this decision. First, the tank available for laboratory measurements is also circular. Secondly, the shape of a pig thorax,

where the real world evaluations were carried out, is also roughly circular. To make the physical behavior of the model more realistic, a 3D model was created, resulting in a cylindrical FEM model.

Next, the mesh density of the FEM model has to be balanced. Since for the training of the ANN thousands of training samples are needed, the mesh must be limited in its density. To strike a compromise between computational speed and precision, the maximum element size for the whole mesh was chosen to be 7.5 mm, while the biggest element size on the electrodes was chosen to be 0.1 mm. This was done, because the current density at the electrodes is biggest and secondly it's spatial rate of change on near the electrodes is quite large for the current density.

3.4.2 Targets

The next crucial part of the training process is the creation of a conductivity distribution inside the model. At first glance, ensuring anatomically inspired conductivity distributions might be a good idea. However, this has a major drawback. If the ANN has only seen anatomically inspired distributions during training, it will likely reproduce them. Most available data for anatomical features stems from healthy subjects. Thus, the ANN would be very likely to reproduce healthy distributions. This bears the risk of not giving accurate reconstructions in the presence of unhealthy features of a potential patient. The goal for the ANN is to learn the general underlying relationship between the boundary measurements and the resulting conductivity distribution.

Base Shapes

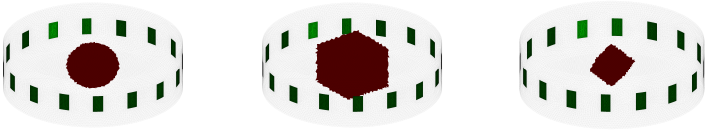
To cover many of the possible conductivity distributions, up to 3 base shapes have been included randomly into the model. The base shapes are a sphere, a cube, and an octahedron. Visualization of the base shapes placed in the center of the FEM model can be seen in Figure 3.6.

The equations for the masks, that define whether a point of the domain is inside a base shape or not, are given by

$$mask_{sphere} = (x^2 + y^2 + z^2) <= 1, \tag{3.7}$$

$$mask_{cube} = max(abs(x), abs(y), abs(z)) <= 1, \tag{3.8}$$

$$mask_{octahedron} = abs(x) + abs(y) + abs(z) <= 1. \tag{3.9}$$



(a) Circle shape **(b)** Cube shape **(c)** Octrahedron shape

Figure 3.6: Example of each primitive shape

Transformation of the base Shapes

As pointed out, up to 3 base shapes were inserted into the domain. To get a more diverse set of training data samples, every base shape was transformed before the insertion into the domain. The three transformation operations are translation, rotation, and scaling along each dimension. The operation of each point can be expressed as

$$\boldsymbol{z'} = (\tilde{\boldsymbol{R}}(\boldsymbol{z} - \boldsymbol{t})) \oslash \boldsymbol{s}, \tag{3.10}$$

where $\boldsymbol{z} = \{x, y, z\}$ is the base position as a vector, $\boldsymbol{z'} = \{x', y', z'\}$ is the resulting-transformed position, $\boldsymbol{t} \in \mathbb{R}^3$ represents the translation, $\tilde{\boldsymbol{R}} \in \mathbb{R}^{3\times3}$ is the rotation-matrix, $\boldsymbol{s} \in \mathbb{R}^3$ is the scaling vector and $\oslash$ represents the element-wise division. For example, the scaling allows for the sphere to be transformed into an ellipsoid. The selection of how many base shapes and which base shapes are used is randomly chosen. Each occurrence has equal probability. Also, the values for the translation, rotation, and scaling were sampled randomly from a uniform distribution. $\boldsymbol{t}$ was sampled such that it is always inside the FEM model. The rotation vector of $\tilde{\boldsymbol{R}}$ was sampled between $[0, 2\pi)$ and $\boldsymbol{s}$ was chosen such that the maximum length of an object lied between 10 % and 80 % of the model radius.

3.4.3 Conductivity Range

An important consideration is the conductivity range used during training. When using EIT tanks for testing purposes, the conductivity range of the test data is usually known. It may be tempting to simply use the same conductivity range to train the ANN. However, in practical scenarios the conductivity is typically not known with such precision. For a cross-section of the chest, conductivity values can range from $3.5 \cdot 10^{-3}\,\mathrm{S\,m^{-1}}$ (cortical bone) to $4.64 \cdot 10^{-1}\,\mathrm{S\,m^{-1}}$ (deflated lung). A range of $1 \cdot 10^{-5}\,\mathrm{S\,m^{-1}}$ to $1\,\mathrm{S\,m^{-1}}$ was used

for the background conductivity, as this ensures to cover the conductivity values typically encountered in chest measurements, while leaving a margin well outside the range to improve generalization. Values were sampled uniformly from a logarithmic array of the above conductivity range, also known as a reciprocal or log-uniform distribution. This choice was made because the ANN should be able to distinguish objects that are an order of magnitude larger or smaller than the background, regardless of the actual background conductivity. The next critical step is the appropriate choice of conductivity enclosures. As mentioned above, it is essential that the ANN can discriminate between conductivity contrasts. At the same time, the ANN should be able to discriminate these contrasts symmetrically, both above and below the background conductivity range. To achieve this, the conductivity of the enclosure is chosen with respect to the background conductivity. This ensures that the ANN is not biased towards a conductivity contrast higher or lower than the background. The enclosure conductivity is therefore chosen by multiplying the background conductivity by values in the range $1 \cdot 10^{-2}$ to $1 \cdot 10^{2}$. Again, this is a uniform sample from the logarithmic array of these values.

In the real world, conductivities are rarely perfectly homogeneous across a tissue type. To account for this, both the enclosures and the background were perturbed. Each node of the FEM model was scaled by different values. This is achieved by using a Gaussian distribution with a mean of 1. For each training sample and chosen conductivity value, a different *std* was chosen from $1 \cdot 10^{-8}$ to $1 \cdot 10^{-2}$. Once the *std* was chosen, the values of a conductivity were perturbed by multiplication with the sampled values. This is visualized for a simple case in Figure 3.7.

3.4.4 Noise Modelling

ANNs often face the challenge of generalizing the learned examples to cases that the ANN has not encountered before. To overcome this problem, further data augmentation strategies must be employed. While the previous steps required new simulations for each training sample, the following steps rely on already simulated data, thus saving computational time.

EIT measurements can be affected by several sources of noise. Combined with the ill-conditioned nature of the EIT problem, this can lead to artifacts in the reconstruction. Reconstruction algorithms often have a hyperparameter that essentially balances the robustness to noise and the quality of the reconstruction. As with ANNs, the sensitivity to noise can be adjusted by the noise present in the training data.

A key component in EIT systems is the analogue-to-digital converter, and the noise consists mainly of thermal noise, jitter noise, and quantization noise [FR97].

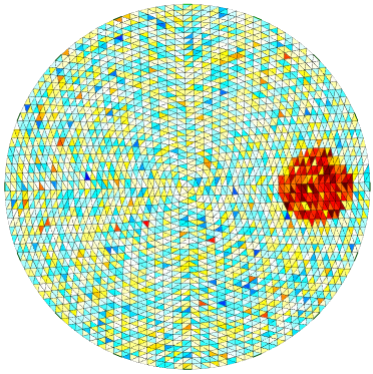


Figure 3.7: Visualization of the non-uniform conductivity distribution of the background and the target.

The first two depend on the size of the signals. The larger the signal, the larger the noise. This can be modelled by multiplying the noise-free signal by a constant derived from Gaussian noise:

$$U^{\mathrm{i,j}}_{\mathrm{ther,jit}} = U^{\mathrm{i,j}} \cdot n_{\mathrm{mult}}, \quad n_{\mathrm{mult}} \sim \mathcal{N}(1, \sigma^2), \forall\, i, j \in \{1, ..., 16\}, \tag{3.11}$$

where $U^{\mathrm{i,j}}\mathrm{ther,jit}$ is the measurement affected by thermal noise, $U^{\mathrm{i,j}}$ is the unaffected measurement, and n_{mult} is the noise sampled from a normal distribution. The quantization noise does not depend on the signal level and can be modelled by adding a noise term to the voltage signals:

$$U^{\mathrm{i,j}}_{\mathrm{quant}} = U^{\mathrm{i,j}} + n_{\mathrm{add}}, \quad n_{\mathrm{add}} \sim \mathcal{N}(0, \sigma^2), \forall\, i, j \in \{1, ..., 16\}, \tag{3.12}$$

where $U^{\mathrm{i,j}}\mathrm{quant}$ is the measurement affected by the quantization noise, and n_{add} is the noise sampled from a normal distribution. However, there is another source of noise. Different measurement channels of a given EIT system may have different gains due to different gains in the multiplexers. This noise can be described as

$$U^{\mathrm{i,j}}_{\mathrm{gain}} = U^{\mathrm{i,j}} \cdot n_{\mathrm{mult}}, \quad n_{\mathrm{mult}} \sim \mathcal{N}(0, \sigma^2), \forall\, j \in \{1, ..., 16\}. \tag{3.13}$$

Note that this noise only affects one row of the EIM, compared to equation (3.11), where each entry is affected individually. For the additive noise, n_{add}, a *std* of $1 \cdot 10^{-8}$ was chosen. For the multiplicative noise, n_{mult}, a *std* of $1 \cdot 10^{-6}$ was chosen.

3.4.5 Data Augmentation

During training, the data can be modified further, such that even more variety is present.

Rotation

To specifically incorporate rotational invariance into the ANN, the voltage data were prepared with minimal computational cost as follows. A shift of n columns along the EIM results in a rotation of the reconstructed image by $\frac{2\pi n}{16}$. Therefore, the target image must be shifted by this angle. To remove the rotation variance, 15 additional shifted voltages for each training sample were generated, as described above.

α-Blending

With the given data set, there is the possibility to generate completely new training samples. In the field of image classification, a technique known as alpha blending is used. This technique creates a new image by linearly combining two other images, using an alpha factor (α) between 0 and 1 to weight the contributions of each image [PD84, Ino18, ZCDLP17]. For example, an α value of 0.3 would result in the new image being a combination of 30% of the first image and 70% of the second image. We can adapt this technique to EIT images as follows

$$\boldsymbol{\sigma}_{comb} = \alpha\boldsymbol{\sigma}_1 + (1-\alpha)\boldsymbol{\sigma}_2 \tag{3.14}$$

Here $\boldsymbol{\sigma}_{comb}$ represents the combined conductivity distribution, which is a linear combination of the conductivity distributions $\boldsymbol{\sigma}_1$ and $\boldsymbol{\sigma}_2$, weighted by α. From Ohm's law, which relates the conductivities to the constant injection current, the procedure for combining the voltage measurements accordingly can be derived:

$$\mathbf{Y_{comb}} = \alpha\mathbf{Y_1} + (1-\alpha)\boldsymbol{Y_2} \tag{3.15}$$

$$\Leftrightarrow \frac{\boldsymbol{I}}{\boldsymbol{U_{comb}}} = \alpha\frac{\boldsymbol{I}}{\boldsymbol{U_1}} + (1-\alpha)\frac{\boldsymbol{I}}{\boldsymbol{U_2}} \tag{3.16}$$

$$\Leftrightarrow \frac{1}{\boldsymbol{U_{comb}}} = \alpha\frac{1}{\boldsymbol{U_1}} + (1-\alpha)\frac{1}{\boldsymbol{U_2}} \tag{3.17}$$

$$\Leftrightarrow \boldsymbol{U_{comb}} = (\frac{\alpha}{\boldsymbol{U_1}} + \frac{1-\alpha}{\boldsymbol{U_2}})^{-1} \tag{3.18}$$

In the above equations $\boldsymbol{Y}$ denotes the admittance between the voltage measurement electrodes and $\boldsymbol{U}$ represents the voltage measurements. By linearly

combining the admittances and then taking the inverse, the combined voltage measurements $\boldsymbol{U_{comb}}$ corresponding to the combined conductivity distribution $\boldsymbol{\sigma_{comb}}$ can be obtained.

3.5 Summary

The exploration of ANNs for EIT has demonstrated their significant potential to address the complex challenges of this imaging technique. The origins of ANNs can be traced back to the pioneering work of Warren McCulloch and Walter Pitts in 1943, who developed a simplified neuron model. This model laid the foundation for modern neural networks, which are now an integral part of various fields, including EIT. The basic components and techniques of ANNs, such as neurons, fully connected layers, backpropagation, weight initialization, convolutional layers, dropout layers and activation functions, are crucial to understanding their operation. Neurons process inputs to produce outputs using a weight matrix, bias vector and activation function. Fully connected layers capture global relationships in the data, while convolutional layers capture local patterns, significantly reducing the number of parameters and improving computational efficiency. Dropout layers prevent overfitting by randomly deactivating neurons during training, and activation functions introduce non-linearity into the network.

The proposed ANN architecture for EIT reconstruction incorporates several innovative features to improve performance. The input vector of measured voltages is transformed into a matrix to facilitate two-dimensional convolutions, exploiting rotational invariance. Convolution blocks with dropout, circular padding, two-dimensional convolution, parametric rectified linear unit and layer normalization extract the necessary features for reconstruction. Fully connected layers are applied separately for each injection, significantly reducing the number of weights. The final reconstruction is obtained by summing the individual reconstructions. The loss function combines mean squared logarithmic error, total variation regularization and L2 weight regularization to ensure convergence and improve reconstruction quality. The ANN was trained using the Adam optimizer with a learning rate reduction strategy to deal with plateaus. The performance of the proposed ANN was evaluated using simulated data, noisy FEM data, tank data and real pig data, demonstrating its ability to capture complex non-linear relationships, reduce reconstruction artifacts and outperform traditional algorithms. Training data is generated through simulations using a FEM model, including different shapes and conductivity distributions to ensure the ANN learns to generalize well to different scenarios. The results will be prensted in chapter 5

For time-independent reconstruction in EIT, the proposed ANN architecture aims to perform accurate reconstructions, minimize the number of weights, exploit rotational symmetry, work effectively on real data and outperform traditional algorithms.

For the case of time-independent reconstruction, an ANN shall have the following desired capabilities:

- Actually perform the time-independent reconstruction
- Have as few weights as possible
- Leverage the rotational symmetry of the adjacent-adjacent pattern
- Properly function on real-world tank- and experimental-data
- Perform better compared to traditional algorithms

4 D-Bar Algorithm

This chapter examines the D-Bar algorithm, a direct method for solving the inverse problem in EIT. The D-Bar algorithm for the direct computation of the conductivity distribution from boundary measurements by transforming the Laplace equation into a time-independent Schrödinger equation. The transformation allows for the usage of mathematical tools, which then enable the direct solution of the conductivity distribution. The D-Bar algorithm enables time-dependent and time-independent reconstruction in a 2D domain.

The chapter commences with a comprehensive mathematical overview, explaining the transformation process and the utilization of complex geometric optics solutions. It then proceeds to discuss the practical considerations for implementing the algorithm, including the handling of non-circular domains and the incorporation of data from other imaging modalities. Furthermore, the chapter addresses the numerical implementation of the D-Bar algorithm and explores the fusion of EIT with radar data to enhance spatial resolution, thereby providing a comprehensive overview of the D-Bar algorithm and its applications.

4.1 Mathematical Outline of the D-Bar Algorithm

The D-Bar algorithm belongs to the class of direct solution approaches for the EIT problem. Instead of retrieving the conductivity iteratively, the algorithm computes a solution based directly on the underlying differential equations. It revolves around finding a solution to the Schrödinger equation. This solution has parts of the conductivity distribution it, which in turn allows for the computation of the conductivity distribution from it. The algorithm works as follows.

The D-Bar algorithm begins with the transformation of the Laplace equation into the time-independent Schrödinger equation. This transformation introduces a new potential, denoted as $\tilde{u}$, which encapsulates both the actual electric potential and the conductivity distribution in it. To solve the transformed equation, specific adjustments are made, resulting in a modified version of the Schrödinger equation. This revised equation includes the Laplacian operator, a complex interaction term, and a potential function $q(z)$. The potential $\mu(z, k)$ is solved using the non-linear Fourier transform, also known as the scattering transform. This mathematical tool is crucial for retrieving the conductivity distribution $\boldsymbol{\sigma}$ from the potential $\mu(z, k)$.

4.1.1 From Laplace to Schrödinger

Given the Laplace equation (2.13) $\boldsymbol{\nabla} \cdot (\sigma \boldsymbol{\nabla} \Phi) = 0$ (note that the negative sign is discarded to align with other literature about the D-Bar algorithm) for a two-dimensional domain Ω (the unit circle), it can be modified into the time-independent Schrödinger equation through change of variables

$$-\boldsymbol{\Delta}\tilde{u} + q(z)\tilde{u} = 0, \quad z \in \Omega, \tag{4.1}$$

where $z = x + jy$ is a representation of the position (x- and y-position in the plane of the electrodes) in complex numbers. $q(z)$ and $\tilde{u}$ are defined as

$$q(z) = \frac{\boldsymbol{\Delta}\sqrt{\boldsymbol{\sigma}(z)}}{\sqrt{\boldsymbol{\sigma}(z)}}, \tag{4.2}$$

$$\tilde{u}(z) = \sqrt{\boldsymbol{\sigma}(z)}u(z). \tag{4.3}$$

When the newly created potential $\tilde{u}$ is known in the domain, the conductivity distribution $\boldsymbol{\sigma}$ can be derived[1]. The Schrödinger equation is widely used in scattering problems[2]. In these scattering problems, the parameters of the material that is scattered need to be estimated. For this, the solution of the Schrödinger equation is necessary. With the help of so-called complex geometric optics (CGO) solutions, a solution to the potential can be constructed. These CGO solutions are noted as $\Psi(z, k)$, where $k = k_1 + jk_2$ is another complex parameter. k can be thought of as a complex-valued frequency. $\Psi(z, k)$ needs to fulfill the property that it is bounded, more formally $\Psi(z, k) \sim e^{jkz}, \|z\| \to \infty$. This results from the fact that in scattering problems, only the stationary scattered wave is of interest[3], and thus, the wave needs to be observed at a great distance to the origin. The parameter k can be thought of as probing or "illuminating" the domain in different directions. Thus, it captures the impedance behavior inside Ω from different directions (like e.g., CT). $\Psi(z, k)$ fulfills equation (4.1) leading to a reformulated Schrödinger equation with respect to $\Psi(z, k)$

$$-\boldsymbol{\Delta}\Psi(z, k) + q(z)\Psi(z, k) = 0. \tag{4.4}$$

[1] The potential $\tilde{u}$ is a purely mathematical construct, which later on allows the usage of advanced math to retrieve the conductivity distribution in the domain

[2] Scattering problems regularly appear in the domain of physics. Of interest here are interactions of light with small particles to determine how light interacts with small particles. Another application is the interaction of soundwaves with rigid surfaces to, e.g., determine the structure of the sea bed.

[3] This is because the stationary waves have the time-dependent interactions decayed, to analyze the wave and calculate the interactions between the incoming wave and the object.

4.1.2 The modified Schrödinger Equation

To make the solution process a little simpler, the exponential term for the solution is factored out, and instead, a new function $\mu(z,k) := e^{-jkz}\Psi(z,k)$ is introduced. This needs to be put into the Schrödinger equation. To make this easier to read, these three definitions are given beforehand,

$$\overline{\boldsymbol{\partial}} = \frac{1}{2}(\frac{\partial}{\partial x} + j\frac{\partial}{\partial y}), \quad \boldsymbol{\partial} = \frac{1}{2}(\frac{\partial}{\partial x} - j\frac{\partial}{\partial y}), \tag{4.5}$$

$$\boldsymbol{\Delta} = 4\boldsymbol{\partial}\overline{\boldsymbol{\partial}}, \tag{4.6}$$

here " $^-$ " denotes the complex conjugate operator. The Schrödinger equation then becomes (the details can be found in the Appendix A.1)

$$\begin{aligned} -\boldsymbol{\Delta}\Psi(z,k) + q(z)\Psi(z,k) &= 0 \\ (-\boldsymbol{\Delta} - 4\overline{\boldsymbol{\partial}}jk + q(z))\mu(z,k) &= 0 \end{aligned} \tag{4.7}$$

The modified Schrödinger equation (4.7) allows us to finally recover the conductivity from $\mu(z,k)$.

However, what is still missing is the direct connection between the solution of the Schrödinger equation and the EIT measurements taken. Nachmann showed a link between the boundary measurements and the CGO solutions [Nac96].

First, the boundary measurements need to be introduced.

4.1.3 Dirichlet-to-Neumann Map

For differential equations, Dirichlet and Neumann boundary conditions are used. These boundary conditions help to find a solution for the differential equations. In the case of EIT, both boundary conditions together can help to find the conductivity distribution.

In case of EIT, the Dirichlet boundary condition imposes a potential distribution on the spatial boundary of the domain, Ω

$$u(z) = g(z), \quad z \in \partial\Omega \tag{4.8}$$

where $g(z)$ is an arbitrary function that imposes a potential distribution.

The Neumann boundary condition imposes a current density on the boundary of Ω. It can be stated as

$$\sigma(z)\frac{\partial u}{\partial \boldsymbol{n}}(z) = \boldsymbol{J}(z), \quad z \in \partial\Omega, \tag{4.9}$$

where $\boldsymbol{n}$ is the outward normal vector of the boundary of Ω.

Both boundary conditions can be mapped to one another. The corresponding Neumann boundary conditions can be computed given all the Dirichlet boundary conditions. In the case of EIT, this works because impedance measurements are carried out (the Dirichlet and Neumann boundary conditions are measured at the same time). A known current (Neumann boundary conditions) is injected into the domain, and at the same time, the potentials on the electrodes can be measured. Thus, the mapping between the Dirichlet and Neumann boundary conditions can be computed. This is formerly known as the Dirichlet-to-Neumann (DtN) map $\boldsymbol{\Lambda}_\sigma$. For a given conductivity $\boldsymbol{\sigma}$ in the domain, it is formally stated as:

$$\boldsymbol{\Lambda}_\sigma : g \rightarrow \sigma \frac{\partial u}{\partial \boldsymbol{n}}\bigg|_{\partial\Omega} \tag{4.10}$$

This mapping is dependet solely on the conductivity distribution inside the domain Ω and thus, from this mapping the conductivity distribution can be computed.

4.1.4 On the D-Bar Equation

The boundary measurements need to be linked to the solution of the modified Schrödinger equation (4.7), which in turn gives the conductivity distribution $\boldsymbol{\sigma}$. This is done by solving the name-giving D-Bar equation of the whole algorithm. Next to equation (4.7) $\mu(z,k)$ must also fulfill the D-Bar equation. This is expressed as[4]

$$\overline{\boldsymbol{\partial}}_k \mu(z,k) = \frac{1}{4\pi\bar{k}} \boldsymbol{t}(k) e_{-z} \overline{\boldsymbol{\partial}(z,k)}, \tag{4.11}$$

where $\overline{\boldsymbol{\partial}}_k$ is the D-Bar operator defined in Equation (4.5) applied to k, e_{-z} is a short form for $e_{-z} = e^{j(kz+\bar{k}\bar{z})}$ and $\boldsymbol{t}(k)$ is the scattering transform[5]. The scattering transform is a transformation that decomposes a signal into nonlinear modes called solutions. As opposed to the normal linear Fourier transform, the frequency spectrum is a complex one. This means that the

[4] The definition of the D-Bar equation is directly given as its deduction would involve yet another approach to involving Fadeev-Green functions, which is too far out of the scope of the thesis. The interested reader is referred to the literature like "Linear and Non-linear inverse problems" [MS12].

[5] This is also sometimes called the non-linear Fourier transform. The main difference between the linear Fourier transform is that waves in the non-linear Fourier transform can be considered as a process to solve non-linear differential equations. However, due to the complexity of such equations, there is no standard procedure to solve every such differential equation with it. Instead, for each problem, the procedure has to be tailored to the problem. A practical example of such a non-linear differential equation would be the determination of the exact solution of the pendulum equation.

coefficients are spread not just in $\mathbb{R}$ but in $\mathbb{C}$. These coefficients are named k throughout this work. Nevertheless, there is still an intuitive interpretation of the coefficients k. When looking at the absolute value of k, higher magnitude components can be regarded as high-frequency components representing rapid, sharp signal changes in the final recosntruction space. The formula for the scattering transform is given by

$$\boldsymbol{t}(k) = \int_{\partial\Omega} e^{j\overline{k}\overline{z}}(\boldsymbol{\Lambda}_\sigma - \boldsymbol{\Lambda}_1)\Psi(z,k)\,ds, \tag{4.12}$$

where $\boldsymbol{\Lambda}_\sigma$ is the DtN map for a given domain and $\boldsymbol{\Lambda}_1$ is the DtN map for a constant domain. The subtraction of $\boldsymbol{\Lambda}_1$ in the scattering transform equation (4.12) has 3 purposes. First, it ensures the D-Bar equation (4.11) is well-posed and solvable. Secondly, it ensures that the scattering transforms equation (4.12) decays for large $|k|$, again ensuring the function is well-defined. If this term disappears, high-frequency singularities can pose a problem. So, the subtraction acts as a smoothing operator, removing singularities and leaving only information relevant to solve for the conductivity $\boldsymbol{\sigma}$.

4.1.5 Retrieving the Conductivity

With the help of the scattering transform $\boldsymbol{t}(k)$, the D-Bar equation (4.11) can then be solved to recover $\mu(z,k)$. The relationship between $\boldsymbol{\sigma}(z)$ and $\mu(z,k)$ is given through the limit of k to 0 $\boldsymbol{\sigma}(z) = \lim_{k\to 0}|\mu(z,k)|^2$. For the real calculation, $\mu(z,k=0)$ is used. This has two reasons, first of all, this makes the calculation easier, as the limit does need to be evaluated. Secondly, $|k|$ can be interpreted as behaving like a real-valued frequency ω. Setting $k=0$ can then be viewed as retrieving the low-frequency part of $\boldsymbol{\sigma}(z)$. As in EIT the injected current is comparatively low, this approximation is close to reality.

4.1.6 Recap of the D-Bar Algorithm

To recap, the Laplace equation was converted into the time-independent Schrödinger equation, which in turn gives a new potential $\tilde{u}$, where the actual electric potential and the conductivity distribution are both present. However, solving this needs further processing. With some modifications, a modified version of the Schrödinger equation arises $(-\boldsymbol{\Delta} - 4\overline{\boldsymbol{\partial}}jk + q(z))\mu(z,k) = 0$. With the help of the non-linear Fourier transform (scattering transform), the potential $\mu(z,k)$ and, thus, $\boldsymbol{\sigma}$ can be retrieved.

4.2 Numerical Implementation

The numerical implementation of the D-Bar algorithm necessitates the execution of several intricate processes in order to ensure the generation of accurate and stable results. This section outlines the key processes that are required for the algorithm's execution and the design choices made in its implementation. Initially, the Dirichlet-to-Neumann map is computed, which involves the handeling of current injection patterns and measured voltages. Following this, the scattering transform is calculated using an exponential approximation in order to manage computational costs. The subsequent stage entails the resolution of the D-Bar equation, which is expressed in integral form and necessitates meticulous attention to numerical instabilities. Ultimately, the complex conductivities are reconstructed from the solution of the D-Bar equation. Each of these steps is of paramount importance for the successful application of the D-Bar algorithm in practical scenarios.

4.2.1 Dirichlet to Neumann Map

The first step of the D-Bar algorithm involves the computation of the DtN map. For a system with N electrodes, there are $N-1$ unique linear independent current injection patterns, given that the potential is directly measured on each electrode.

For the calculation of the DtN map, the used current patterns must be linearly independent. Since in the real world, the potential is only known on discrete places on the boundary (the electrodes), the DtN map is approximated through the matrix $\boldsymbol{L}_\sigma$, which is of size $N-1 \times N-1$. To enhance numerical stability, the Neumann-to-Dirchlet (NtD) map $\boldsymbol{R}_\sigma$ is computed first, which acn then be transformed to form the desired DtN map.

For this, at first, the matrix $\vec{\boldsymbol{J}}$ of current injection patterns is needed. The columns represent the different current injections and the rows, the injected current on each electrode. This then results in a $N \times N-1$ matrix. In the literature concerning the D-Bar algorithm, trigonometric current patterns are used. They were described in section 2.1.3.

Another important quantity for the NtD or DtN map is the matrix of measured voltages $\boldsymbol{U}$. It has the same dimension as $\vec{\boldsymbol{J}}$ and thus also the same physical interpretation. Each column is a specific realization of one injection scheme, while each row represents the measured potential on each electrode. For computational purposes and convention, each column of $\boldsymbol{U}$ must sum up to zero $\sum_{n=1}^{N} u_{n,m} = 0$. This effectively moves the reference potential to somewhere inside the domain. The calculation of the NtD map can be performed

through

$$\boldsymbol{R}_\sigma = \frac{1}{A}\vec{\boldsymbol{J}}^T\boldsymbol{U}, \tag{4.13}$$

where A is the surface area of the electrodes, and ^{T} represents the matrix transpose [MM09]. To finally get the desired DtN matrix $\boldsymbol{L}_\sigma$, $\boldsymbol{R}_\sigma$ has to be transformed. This transformation can be computed through an inversion of $\boldsymbol{R}_\sigma$:

$$\boldsymbol{L}_\sigma = \boldsymbol{R}_\sigma^{-1}. \tag{4.14}$$

The homogenous DtN map $\boldsymbol{L}_1$ can be calculated, e.g., through simulation data by setting the background conductivity to 1. $\boldsymbol{L}_\sigma$ and $\boldsymbol{L}_1$ are the discrete approximations of $\boldsymbol{\Lambda}_\sigma$ and $\boldsymbol{\Lambda}_1$ in equation (4.12).

4.2.2 Calculation of the Scattering Transform

The next step in the D-Bar algorithm is to calculate the numerical approximation to the scattering transform. Here the so-called exponential approximation is used, which replaces $\Psi(z,k)$ by e^{jkz} as $\Psi(z,k) \sim e^{jkz}, \|z\| \to \infty$ [DM14]. This is one of the least expensive options in terms of computational cost. With this approximation, equation (4.12) becomes $\boldsymbol{t}^{exp}(k) = \int_{\partial\Omega} e^{j\bar{k}\bar{z}}(\Lambda_\sigma - \Lambda_1)e^{jkz}ds$. Both functions e^{jkz} and $e^{j\bar{k}\bar{z}}$ need to be expressed in terms of linear combinations of the applied current patterns. This is a change of basis known from linear algebra. The coefficients are for e^{jkz} are $\boldsymbol{c}(k) = [c_1(k), ..., c_N(k)]^T$ and for $e^{j\bar{k}\bar{z}}$ they are $\boldsymbol{d}(k) = [d_1(k), ..., d_N(k)]^T$. The coefficients are calculated through,

$$\boldsymbol{c}(k) \;=\; \vec{\boldsymbol{J}}^T e^{ik\boldsymbol{z}_{el}} \; and \; \boldsymbol{d}(k) = \vec{\boldsymbol{J}}^T e^{i\bar{k}\bar{\boldsymbol{z}}_{el}},$$

where $\boldsymbol{z}_{el}$ denotes the vector of the electrode positions. The exponential approximation of the scattering transform can then be expressed as

$$\boldsymbol{t}^{exp}(k) \;\approx \sum_{i=1}^{N-1}\sum_{j=1}^{N-1} c_j(k)d_i(k)\big(\boldsymbol{L}_\sigma(i,j) \;-\; \boldsymbol{L}_1(i,j)\big) \tag{4.15}$$

$$= \boldsymbol{d}^{\mathsf{T}}(k)\Big(\big(\boldsymbol{L}_\sigma \;-\; \boldsymbol{L}_1\big)\boldsymbol{c}(k)\Big). \tag{4.16}$$

Still missing in the explanation is the complex-valued frequency-like parameter k. As mentioned in section 2.3.2, the solution to the EIT problem does not depend continuously on the input data (large changes in the conductivity distribution only lead to small changes in the measurement data). This effect leads to instabilities in $\boldsymbol{t}^{exp}(k)$ as $|k|$ becomes larger. Thus, some filtering is

needed to make the next steps computable. This is done through the definition of a cut-off value of $|k| < R$. In the literature, R is therefore referred to as the "truncation radius". $\boldsymbol{t}^{exp}(k)$ is only evaluated for all $|k|$ in this truncation radius. This is denoted as $\boldsymbol{t}_R^{exp}(k)$. As explained in the mathematical outline of the algorithm in section 4.1, k is important for the construction of the solution to the time-independent Schrödinger equation. For calculations involving k, a grid needs to be constructed. To make the calculation steps that follow after the calculation of $\boldsymbol{t}^{exp}$ easier, the layout of this grid has to be chosen wisely. This is because later there is a singularity in $k = 0$. Thus, in this work, the approach by Mueller and Siltanen presented in chapter 15 of their book "Linear and Nonlinear Inverse Problems with Practical Applications" is used for the construction of the k-grid [MS12]. In this approach, a k-grid is built, this matrix is $\vec{\boldsymbol{K}}$ and has a shape of $P \times P = 2^p \times 2^p$ and its contents are complex. The calculation of the values inside $\vec{\boldsymbol{K}}$ depend on the chosen truncation radius R. A vector $\boldsymbol{k}_{help} = [-R, -R + \frac{2R}{M-1}, ..., R - \frac{2R}{M-1}, R]$ is used to define each entry in $\vec{\boldsymbol{K}}$. The grid is then constructed through

$$\vec{\boldsymbol{K}} = \boldsymbol{k}_{help} \times \boldsymbol{k}_{help}$$

where $\times$ is defined as $\boldsymbol{a} \times \boldsymbol{b} = \{a + jb \,|\, a \in \boldsymbol{a} \, and \, b \in \boldsymbol{b}\}$.

An example calculation for this can be seen in Figure 4.1. The point $\vec{\boldsymbol{K}}_{(1,1)}$ has the value $-R + jR$ and $\vec{\boldsymbol{K}}_{(8,8)}$ has the value $R - jR$.

4.2.3 Solving the D-Bar Equation

Equipped with $\vec{\boldsymbol{K}}$ and $\boldsymbol{t}^{exp}(k)$, $\mu(k, z)$ can be solved. The D-Bar equation (4.11) can also be formulated in its integral form, which is written as

$$\mu(z,k) = 1 + \frac{1}{(2\pi)^2} \int_{\mathbb{R}^2} \frac{\boldsymbol{t}(k)}{(s-k)\bar{k}} e_{-z} \overline{\mu}(z,k) \, dk_1 dk_2 \ .$$

This form can be interpreted as the convolution of equation (4.11) and the Greens's function $G_{\overline{\boldsymbol{\partial}}}$ of the D-Bar operator. Thus, a computational solution for $\mu(z, k)$ can be formulated as

$$\mu(z,k) = 1 + G_{\bar{\boldsymbol{\partial}}} * (T(z,k)\overline{\mu(z,k)}), \tag{4.17}$$

$$\text{with } T(k,z) = \frac{\boldsymbol{t}_R^{exp}(k)}{4\pi\bar{k}} e_{-z}(k), \tag{4.18}$$

$$\text{and } G_{\bar{\boldsymbol{\partial}}} = \frac{1}{\pi k} \ . \tag{4.19}$$

In the analytical case, k must be evaluated on the whole complex number plane. However, since there are the mentioned numerical instabilities, only

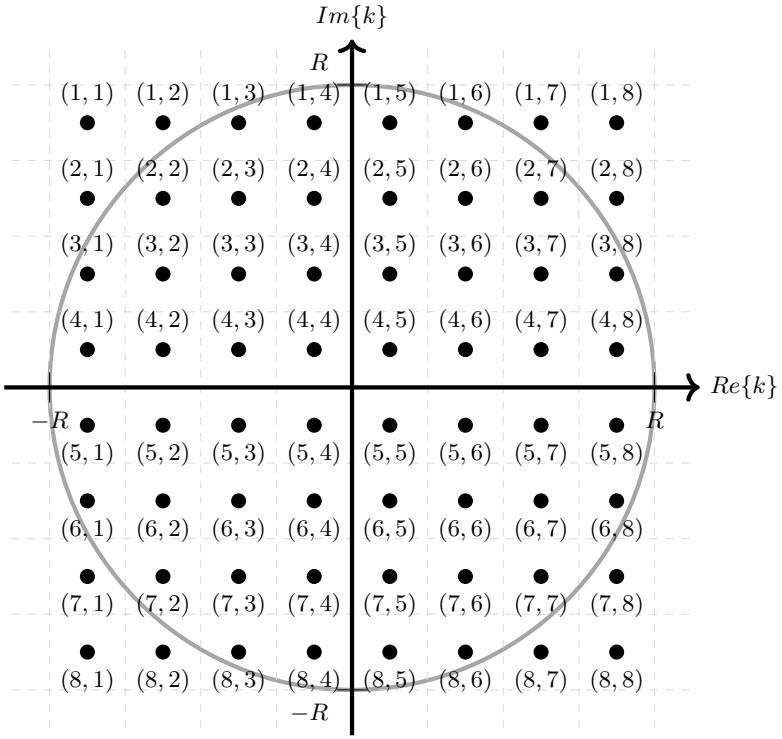


Figure 4.1: Example of $\vec{\boldsymbol{K}}$ for $p = 3$. This results in a 8×8 grid. The values at the points correspond to the indices in $\vec{\boldsymbol{K}}$. The coordinate system of the complex numbers is given as a reference. The gray circle in the background is the truncation radius of R.

values for $|k| < R$ are considered. This means that the whole plane for k is not needed and the Fast Fourier Transform (FFT) trick introduced by Mueller and Siltanen [MS12] can be performed to evaluate the convolution with the help of the linear Fourier transform[6]. To achieve this, yet another grid of values for k needs to be defined. This grid is slightly larger, to ensure that $\mu(z,k)$ is periodic and the application of the linear Fourier transform is valid. The grid is defined as $\boldsymbol{Q}$ and is computed through

$$\boldsymbol{Q} = \boldsymbol{q}_{help} \times \boldsymbol{q}_{help}, \tag{4.20}$$

with $\boldsymbol{q}_{help} = [-2R-3\epsilon, -2R-3\epsilon+\frac{4R+3\epsilon}{2^p}, ..., 2R+3\epsilon-\frac{4R+3\epsilon}{2^p}, 2R+3\epsilon]$ $(\epsilon > 0)$. The parameter 2^p ensures that the grid size is compatible with the fast Fourier transform. This makes $\boldsymbol{Q}$ of shape $2^p \times 2^p$. Throughout this work, $\epsilon = R/6$ and $p = 6$ are used. The resulting grid looks like

$$\boldsymbol{Q} = \begin{bmatrix} -2R-3\epsilon+j(2R+3\epsilon) & \dots & 2R+3\epsilon+j(3R+3\epsilon) \\ \vdots & \ddots & \vdots \\ -2R-3\epsilon-j(3R+3\epsilon) & \dots & 2R+3\epsilon-j(3R+3\epsilon) \end{bmatrix}.$$

It is important to note that the origin is again not part of the grid to avoid the singularities of equations (4.18) and (4.19). Evaluating equation (4.19) on every point of $\boldsymbol{Q}$ and simply plugging this into equation (4.17) does not work, due to the fact, that the FFT expects periodic functions. The result of equation (4.19) has to be made periodic. This is done through a weighting function $\eta(k)$, which is defined as

$$\eta(k) = \begin{cases} 1 & |k| < 2R+\epsilon \\ (2R+3\epsilon-|k|)/(2\epsilon) & 2R+\epsilon \leq |k|. \\ 0 & 2R+3\epsilon < |k| \end{cases}$$

The periodic version of $G_{\bar{\boldsymbol{\partial}}}$ is defined as $\widetilde{G_{\bar{\boldsymbol{\partial}}}} = G_{\bar{\boldsymbol{\partial}}}\eta$, which is then subsequently evaluated on every grid point of $\boldsymbol{Q}$ leading to the matrix $\widetilde{\boldsymbol{G}}_{\bar{\boldsymbol{\partial}}}$. $T(z,k)$ is evaluated at every point of $\vec{\boldsymbol{K}}$ leading to $\boldsymbol{T}_{temp(z,k)}$[7]. Since $\boldsymbol{Q}$ is larger than $\vec{\boldsymbol{K}}$, the dimensions have to be matched together. This is achieved by padding 0 to the borders of $\boldsymbol{T}_{temp}$, which lead to $\boldsymbol{T}$. Now $\widetilde{G_{\bar{\boldsymbol{\partial}}}}$ and $\boldsymbol{T}$ have the same dimensions

[6] The Fourier transform here is purely for evaluation of the convolution and not in any way related to the non-linear Fourier transform $\boldsymbol{t}(k)$.

[7] As the first part of equation (4.18) is independent of z, it can be computed once and then stored for every evaluation of $\boldsymbol{T}_{temp}$ of a specific z.

for the numerical evaluation of equation (4.17). The D-Bar equation can then be written in matrix form as

$$\boldsymbol{\mu} = \boldsymbol{I} + h^2 IFFT(FFT(\widetilde{\boldsymbol{G}}_{\tilde{\delta}}) \odot FFT(\boldsymbol{T}\overline{\boldsymbol{\mu}})) \tag{4.21}$$

$$\leftrightarrow$$

$$\boldsymbol{I} = \boldsymbol{I}\boldsymbol{\mu} - P(\boldsymbol{T}\overline{\boldsymbol{\mu}}) \tag{4.22}$$

with

$$P(\boldsymbol{T}\overline{\boldsymbol{\mu}}) = h^2 IFFT(FFT(\widetilde{\boldsymbol{G}}_{\tilde{\delta}}) \odot FFT(\boldsymbol{T}\overline{\boldsymbol{\mu}})), \tag{4.23}$$

here h is the spacing of the $\vec{\boldsymbol{K}}$- or $\boldsymbol{Q}$-grid,$\boldsymbol{I}$ denotes the identity matrix and $\odot$ stands for the elementwise multiplication. Equation (4.22) almost resembles a linear equation. However, it is only linear in its real part, as $\boldsymbol{\mu}$ appears once in its normal and once in its complex conjugated form. This requires the usage of a matrix-free solver like e.g., GMRES. To deal with this, the real- and imaginary-part of $\boldsymbol{q}$ have to be detached from one another. The matrix $\boldsymbol{q}$ is a matrix of $\mathcal{C}^{2^p \times 2^p}$, which is transformed for GMRES into a vector of $\mathcal{R}^{2 \cdot 2^{p+1}}$. The first 2^{p+1} entries are the real-valued parts and the second 2^{p+1} entries are the imaginary parts. After GMRES has solved the resulting equations, the system $\boldsymbol{\mu}$ is again a matrix.

4.2.4 Reconstruction of Conductivities

To finally retrieve the conductivity at any point z in the domain $\boldsymbol{\Omega}$, $\sigma(z) = |\mu(z, k \to 0)|^2$ is used. Since $\boldsymbol{\mu}$ does not directly contain $k = 0$, the value has to be e.g. interpolated from the four nearest neighboring points. The formula arises from the Schrödinger equation (4.1). The mathematical explanation for the fact that the evaluation takes place as $k \to 0$ is that the solution to the D-Bar equation was constructed precisely to be valid for $k \to 0$. A more intuitive explanation is that small values of $|k|$ are more stable and thus the numerical process of retrieving the conductivity is more stable.

4.2.5 Summary

The D-Bar algorithm is a powerful tool for reconstructing complex conductivity distributions within a domain from boundary measurements. Here, the major contribution was how to implement this approach numerically robust from different techniques. The work was divided into several critical stages, each contributing to the overall goal of accurate and stable conductivity reconstruction. To aid the user in the udnerstanding of the D-Bar algorithm, a

pseudo code version of the D-Bar algorithm is provided in this work in the Appendix A.2. A version of the D-Bar algorithm used in this work was submitted to the EIDORS project and is availble for seemles integration into the whole EIDORS framework [R$^+$23].

Key stages of the D-Bar Algorithm

Computation of the Dirichlet to Neumann (DtN) Map The first step has been to calculate the DtN map, which is essential for relating the boundary voltages to the injected currents. This can be achieved by first calculating the NtD map and then inverting it to obtain the DtN map. The use of trigonometric current patterns ensures linear independence and numerical stability.

Scattering Transform Calculation The scattering transform is computed using an exponential approximation to manage the computational cost. This transform is essential to convert the boundary data into a form suitable for solving the D-Bar equation. The approximation involves expressing the exponential functions in terms of linear combinations of the applied current patterns.

Solving the D-Bar Equation The D-Bar equation is solved in its integral form, which can be interpreted as a convolution with the Green's function of the D-Bar operator. Numerical instabilities are addressed by truncating the complex plane and using a grid-based approach for the computations. The FFT haS been employed to efficiently evaluate the convolution.

Reconstruction of complex Conductivities The final step is to reconstruct the conductivity distribution from the solution of the D-Bar equation. This is done by interpolating the solution as $k \to 0$ to ensure numerical stability. The reconstructed conductivity provides insight into the internal structure of the domain under investigation.

These subsequent steps are visualised in the figure 4.2.

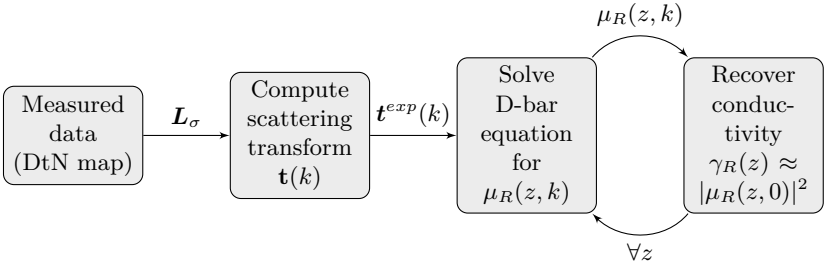


Figure 4.2: Visualization of the key steps of the D-Bar algorithm.

4.3 Computational aspects in the real World

This section examines practical computational aspects of implementing the D-Bar algorithm for EIT. It considers current injection patterns, particularly trigonometric patterns, which are known for their superior reconstruction quality but which pose hardware challenges. In most applications, therefore, the use of adjacent current patterns is necessary. It also addresses the assumption of a circular domain, which is often violated in real-world applications. A correction matrix is introduced to adapt the NtD map for deformed domains, ensuring more accurate reconstructions. Furthermore, the issues that arise when conducting 2- and 3-probe measurements due to the uncertainty of contact impedance and the limitations of the hardware are adressed. A strategy that utilizes only 4-probe measurements, employing variational regularization to simulate a full set of measurements and form the necessary matrices for the D-Bar reconstruction is proposed. This approach ensures robust and accurate conductivity reconstructions, circumventing the limitations of 2- and 3-probe measurements.

4.3.1 Current Injection Pattern

In EIT the impedance measurements can be carried out in several ways. This has already been pointed out in section 2.1.3.

In the literature of the D-Bar algorithm, trigonometric current injection patterns have been widely used. It has been shown that indeed these patterns offer great advantages in terms of reconstruction quality [AGM11]. This is due to the fact that these patterns excite the domain in vastly different ways, as it offers low (low m) and high (high m) spatial varying currents (recall figure 2.3 as an example for a high m). This leads to vastly different current flows in the

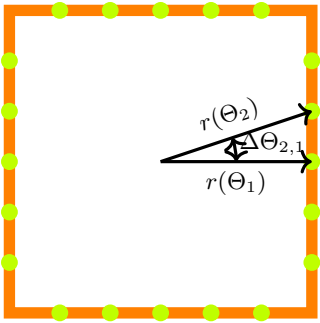


Figure 4.3: Visualization of the finite element model with the position of the electrodes in cyan and the boundary of the domain in blue. Θ_1 and Θ_2 are the position angles of the first and second electrode, while $r(\Theta_1)$ and $r(\Theta_1)$ are the position in terms of distance to the center of the first and second electrode. For the calculation of the derivative in equation (4.24), the angle difference $\Delta\Theta_{2,1}$ is needed.

domain and thus different extractions of information about the conductivity distribution. From a mathematical point of view, this can be seen through the relatively low condition numbers of both the current injection matrix $\vec{\boldsymbol{J}}$ and the Jacobian. However, there is one major drawback in terms of real-world applications. The hardware design requirements are very complex, as the hardware needs to be able to inject a defined current through all electrodes at the same time. Thus, to be compatible with the vast majority of EIT devices or multichannel impedance measurement systems, other injection patterns should be chosen. The most common choice in practical applications is the adjacent current pattern. This can be used for stimulation. However, in the standard approach, there are N adjacent stimulations. As mentioned in section 4.2, there exists only $N-1$ linear independent current patterns. Thus, the N^{th} current pattern can be expressed as a linear combination of the previous ones. To alleviate this problem, the N^{th} stimulation is simply discarded for the calculation of $\vec{\boldsymbol{J}}$.

4.3.2 Non-circular Domain

The common approaches for the D-Bar algorithm assume the domain to be a unit circle. This is due to the fact that it makes it easier to solve the necessary equations. In reality, however, this assumption is often violated. To overcome this, Herrera et al. developed a linear correction term to better capture such

a deformed domain [HVML14]. An illustrative example of a deformed domain can be seen in Figure 4.3. Instead of a circle, the domain is a square with equidistantly placed electrodes along each of the faces. Along each face, 5 electrodes are placed. These are marked as light green circles. To incorporate the changes, equation (4.13) needs to be modified. A matrix $\boldsymbol{S}$ is introduced, which scales each entry of $\vec{\boldsymbol{J}}$ to make the NtD map $\boldsymbol{R}_\sigma$ better adapted to the deformed domain. Each entry of the correction matrix $\boldsymbol{S}$ is calculated as

$$s_n^m = \sqrt{r^2(\Theta_n) + \frac{r(\Theta_n) - r(\Theta_{n-1})^2}{\Delta\Theta_{n,n-1}}} \cdot \Delta\Theta_{n,n-1} \approx \sqrt{r^2(\Theta_n) + \frac{\partial r(\Theta_n)^2}{\partial\Theta_n}} \cdot d\Theta, \tag{4.24}$$

$r(\theta_n)$ with the radius (distance from model center to electrode) of the model at the electrode angle Θ_n. Here, Θ_n describes the electrode position in terms of its angle. The correction term basically makes the numerical integral of the NtD more accurate, as the continuous form of the NtD map involves a boundary integral of the whole domain. Finally, with $[\boldsymbol{S}]_{n,m} = s_n^m$ the correction matrix $\boldsymbol{S}$ can be assembled. s_n^m is independent of m, as can be seen from equation (4.24). The reason for this is that the geometry is not subject to change from one stimulation to the next. The results are then formed into a vector that is repeated M times to form the $N \times M$ matrix $\boldsymbol{U}$. So the modified equation for the NtD map can be calculated through

$$\boldsymbol{R}_{\sigma,corrected} = \frac{1}{A}(\vec{\boldsymbol{J}} \odot \boldsymbol{S})^T \boldsymbol{U}, \tag{4.25}$$

, again, $\odot$ denotes the element-wise multiplication as introduced earlier in equation (4.21).

4.3.3 The 2-probe Measurement Problem

For the calculation of the DtN map Λ_σ, the knowledge of $\boldsymbol{U}$ is required. This in turn has the potential of every electrode for each injection pattern in it. This involves 4-, 3- and 2-probe measurements. As mentioned in section 2.2.3, 2-probe measurements are very problematic because of the unknown contact impedance. Also, 3-probe measurements are at least partially problematic. This in turn potentially makes all the potentials in $\boldsymbol{U}$ apart from the 4-probe measurements highly problematic, as the EIT reconstruction is very sensitive to changes in the measured potential. Even when these problematic measurements would be perfect, there are still hardware limitations. The commercially available EIT device Pulmovista® 500 from Draeger e.g. can only perform 4-probe measurements. Thus, a strategy to overcome these issues needs to be developed.

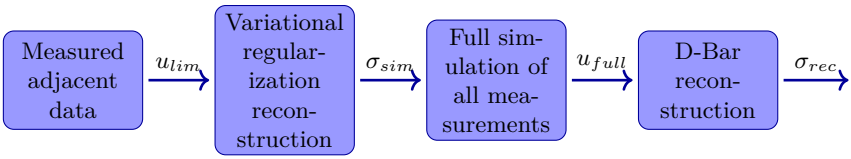


Figure 4.4: Visualization of the key steps of the 2- and 3-probe measurement simulation algorithm.

Solution Strategy for 4-probe D-Bar Reconstructions

In order to overcome the limitations of using two- and three-probe measurements in the D-Bar algorithm, a strategy that makes use of only four-probe measurements is proposed (an outline of the key steps is given in figure 4.4):

1. **Acquisition of Adjacent 4-Probe Measurements**
   Firstly, four-probe measurements are taken in proximity to the EIT device. This is a crucial step, as it avoids the issues associated with unknown contact impedance and hardware limitations that prevent the use of two- and three-probe measurements.

2. **Initial Conductivity Reconstruction using Variational Regularization**
   The acquired four-probe measurements are then utilized to reconstruct an initial conductivity distribution via a variational regularization algorithm, such as the Gauss-Newton method. The primary objective of this stage is not to achieve an accurate reconstruction but to capture the physical properties of the voltage measurements. This can be linked to spline interpolation, where the focus is on representing the underlying function rather than the specific coefficients.

3. **Simulation of a full Set of Measurements**
   A full set of measurements is simulated using the initial conductivity distribution obtained from variational regularization. This step generates the voltages that would be expected if the reconstructed conductivity distribution were accurate. By doing so, the problematic two- and three-probe measurements are effectively bypassed, as they are not required in the simulation.

4. **Formation of Matrices $\vec{J}$ and U**
   The simulated measurements are then utilized to form the matrices $\vec{J}$ and U. As mentioned before, the matrix $\vec{J}$ has dimensions $\mathbb{R}^{N\times(N-1)}$, where

each row represents the current at a given electrode and each column represents a specific current injection pattern. The matrix $\boldsymbol{U}$ also has dimensions $\mathbb{R}^{N\times(N-1)}$, where each row represents the potential at an electrode, and each column represents the potentials given the current injection in the corresponding column of $\vec{\boldsymbol{J}}$.

5. **D-Bar Reconstruction**
   Finally, the D-Bar algorithm is applied using the matrices $\vec{\boldsymbol{J}}$ and $\boldsymbol{U}$ to reconstruct the conductivity distribution. The D-Bar algorithm involves computing the DtN map $\boldsymbol{L}_\sigma$, the scattering transform, solving the D-Bar equation, and recovering the conductivity values. This method ensures that the reconstruction is robust and less sensitive to the issues associated with 2- and 3-probe measurements.

4.4 Time-independent D-Bar (absolute)

Due to the DtN difference term in the equation (4.16) ($\boldsymbol{L}_\sigma - \boldsymbol{L}_1$), per default the D-Bar algorithm can be used as a time-dependent reconstruction technique. If it is used that way, $\boldsymbol{L}_1$ is the reference measurement, e.g., a homogenous tank, while $\boldsymbol{L}_\sigma$ is the measurement of the data at a certain time point.

To overcome this limitation and extend the usability of the D-Bar algorithm to the time-dependent case, there is a way to construct $\boldsymbol{L}_1$ purely from the inhomogeneous measurements $\boldsymbol{L}_\sigma$. In the last section, a technique for the D-Bar algorithm only using 4-probe measurements was introduced. This approach can be used to construct a way to make a time-independent D-Bar algorithm possible.

The second step of the previously described reconstruction pipeline was "*Initial Conductivity Reconstruction using Variational Regularization*". To reiterate, this step was solely used to create a voltage measurement distribution that is very close to the original measurements. The outcome of this is an FEM model with a conductivity distribution $\boldsymbol{\sigma}_{sim}$. This distribution can be used to craft a homogenous measurement set that is very close to the inhomogeneous one, but still allows the visual inspection of the underlying inhomogeneous reconstruction $\boldsymbol{\sigma}_{rec}$.

This process works as follows:

- Just like in the previously mentioned scheme, a reconstruction $\boldsymbol{\sigma}_{sim}$ based on the inhomogeneous measurements $\boldsymbol{u}_{inh}$ is performed. From this the median conductivity σ_{median} is extracted. This is in turn used as the conductivity for the entire FEM model. From this, a full set of measurements $\boldsymbol{u}_{full,sim}$ is simulated. This can then be used to construct the DtN map $\boldsymbol{L}_1$.

- For the construction of $\boldsymbol{L}_\sigma$, the measurements $\boldsymbol{u}_{inh}$ can be used directly (if also the 2- and 3-probe measurements are present) or the approach described previously needs to be used.
- This then gives a true time-dependent D-Bar reconstruction, as the difference term of equation (4.16) is still present but solely dependent on the inhomogeneous voltage.

4.5 Time-independent D-Bar (frequency-differential)

An alternative approach to utilizing the D-Bar algorithm in a time-independent manner is the application of the frequency-dependent conductivity of tissues. As outlined in chapter 2 and referenced in section 2.2.2, tissues exhibit a frequency-dependent increase in conductivity. For EIT, of particular interest is the β-dispersion given the frequency range of 50 kHz to 1 MHz. In this range, the conductivity increases due to the capacitive effects of cell membranes. This increase is visible in the real part of the admittance (the conductance).

This frequency-dependent behavior can be leveraged to visualize the conductivity difference between two frequencies using the D-Bar algorithm. For this purpose, the equation for the nonlinear Fourier transform, equation (4.16), is of interest. In particular, the difference term between the inhomogeneous and the homogeneous conductivity Dirichlet-to-Neumann (DtN) map, denoted by $\boldsymbol{L}_\sigma - \boldsymbol{L}_1$, is of crucial importance.

To implement this, it is not necessary to modify the D-Bar algorithm itself. Only the data collection strategy requires adjustment. $\boldsymbol{L}_\sigma$ is collected at a high frequency, and $\boldsymbol{L}_1$ is collected at a low frequency. Subsequently, the reconstruction is conducted in accordance with the standard procedure.

This approach results in a discrepancy in the conductivity distribution in terms of frequency. By comparing the reconstructions at different frequencies, it is possible to gain valuable insights into the frequency-dependent properties of the tissues. This method can enhance the contrast and provide additional diagnostic information, particularly in medical imaging applications where frequency-dependent conductivity variations are significant.

4.6 Fusion of EIT and other Modalities

EIT is characterized by low spatial resolution compared to other modalities such as Computed Tomography (CT), ultrasound, or radar. To address this limitation, a fusion of additional information into the reconstruction process could be beneficial. The intermediate state of the D-Bar algorithm provides an opportunity for such data fusion.

This fusion can be accomplished in the non-linear Fourier domain, represented by $\boldsymbol{t}(k)$. In this domain, high values of $|k|$ can be interpreted as high-spatial-frequency changes of σ in the final reconstruction, while lower values of $|k|$ correspond to low-changing features of σ.

As an example the EIT data is fused with radar data. As a twist, the radar data only provides spatial information along the x-axis.

In a fusion process, the complementary strengths of EIT and radar could be leveraged as follows:

1. EIT data is utilized for low $|k|$ values, capturing the overall conductivity structure.

2. Radar data, with its higher spatial resolution, is incorporated for higher $|k|$ values, providing finer details.

This fusion method would combine the deep penetration capabilities of EIT with the high-resolution information from radar. This could be beneficial to improve tissue differentiation as for example in tumor screening applications. In the subsequent sections, the fusion process will be described in detail, along with the simulation setups for both EIT and radar, and the reconstruction methods used to generate the final fused image.

4.6.1 Fusion in the Scattering Transform

The fusion process makes use of the scattering transform, denoted by $\boldsymbol{t}(k)$, which plays a pivotal role in the D-Bar algorithm. As mentioned before, for EIT applications, the calculation of $\boldsymbol{t}(k)$ is typically truncated to a radius R in the complex k-plane. This truncation is necessary for the following reasons:

1. It is inadvisable to employ values of $\boldsymbol{t}(k)$ for $|k| > R$ in the reconstruction of EIT data, as this may result in numerical instabilities.

2. The limited spatial resolution of EIT results in the unreliable capture of high-spatial-frequency information, corresponding to large values of $|k|$.

However, the fusion process allows for the incorporation of supplementary high-resolution data from sources such as radar imaging into the scattering transform. This is accomplished by extending the range of k-values utilized in the reconstruction, as illustrated in Figure 4.5.

The fusion process divides the k-space into three regions:

1. For values of k that satisfy $|k| \leq R_1$. The data obtained from EIT is used exclusively, providing information about the conducitvity distribution ar low-frequencies.

2. For k vlaues between $R_1 < |k| \leq R_2$, the process continues as follows: Radar data is incorporated to contribute high-frequency details that enhance spatial resolution.

3. For radius of k greater than $|k| > R_2$: Values are set to zero to maintain numerical stability.

This approach is formalized in the following equation, which represents the fused scattering transform:

$$\boldsymbol{t}^{fusion}(k) = \begin{cases} \boldsymbol{t}_{R_1}^{EIT}(k), & |k| \leq R_1 \\ \boldsymbol{t}_{R_2}^{radar}(k), & R_1 < |k| \leq R_2 \\ 0, & R_2 < |k| \end{cases}. \tag{4.26}$$

where $\boldsymbol{t}_{R_1}^{EIT}(k)$ represents the EIT scattering transform truncated at R_1, and $\boldsymbol{t}_{R_2}^{radar}(k)$ represents the radar-derived scattering transform extending to R_2.

This fusion method leverages the respective advantages of both modalities, namely:

- EIT provides deeper tissue penetration and overall conductivity structure.

- Radar contributes higher spatial resolution for finer details.

The resulting fused scattering transform $\boldsymbol{t}^{fusion}(k)$ is then used in the standard D-Bar algorithm for the final reconstruction, potentially improving the overall quality and resolution of the image. This method combines the advantages of EIT, which provides deeper penetration compared to radar, with the advantages of radar, which provides higher spatial resolution. The fused $\boldsymbol{t}^{fusion}(k)$ is then normally used in the D-Bar algorithm for the final reconstruction, exploiting the strengths of both modalities to improve the overall quality of the reconstruction.

4.6.2 EIT Simulation Setup for the Fusion

One possible motivation for fusion is to better visualize tumors in the female breast. Here, using radar as an additional information for EIT might improve the resolution of EIT. However, relying on radar alone may not be ideal because fat attenuates radar signals. The general setup without tumor inclusions for this study is the same as the model shown in Figure 4.6. The electrodes were placed in the cyan colored areas. To mimic the female breast as described by Prati et al. [PMK+20], also a 2mm layer of skin was added. The inside of the breast was modelled as adipose tissue. The dual-purpose electrodes placed on

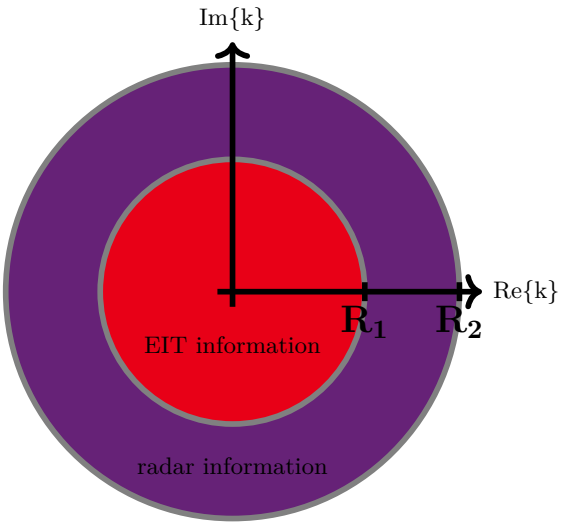


Figure 4.5: Visualization of the merging in the k-space. The purple area represents the k-space that is filled with $\boldsymbol{t}^{radar}(k)$, while the red area is filled with $\boldsymbol{t}^{\boldsymbol{EIT}}(k)$. Values outside $|k| <= R_2$ are zero.

the top and bottom of figure 4.6 were designed by Nguyen et al. [NMK+21]. The radar antennas were designed as a two-layera board, which had desired reflection capabilities in the range of 10 GHz to 30 GHz for pure radar purposes, while also allowing impedance measurements. This is because the antennas have a part on the top layer that can be used to make direct contact with a medium and then make EIT measurements.

4.6.3 Radar Simulation Setup

The radar component of the fusion process was simulated based on the setup described by Prati et al. [PMK+20]. This simulation was designed to complement the EIT data and provide high-resolution information for the fusion process. The key elements of the radar simulation setup are as follows:

1. **Antenna Design:**
    - Patch antennas: Square-shaped with edge length $l_{patch} = 3\,\text{mm}$
    - Substrate: RO4350B with dielectric constant $\epsilon_r = 3.55$ @ 10 GHz

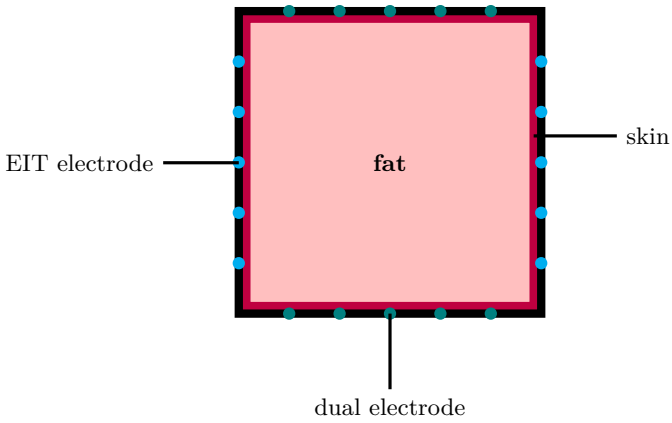


Figure 4.6: Structure of the FEM model that was used. The dual-use EIT electrodes/radar antennas are at the bottom and top. On the right and on the left, there are the ordinary EIT electrodes. The skin is colored red. Fat, represented by the pink areas, is assumed to be present in the remaining breast volume. The size of the model is 100 mm × 100 mm. This is similar to Prati et al. [PMK+20]. Graphic adpated from Rixen et al. [RLM+23].

- Excitation: Coaxial probe matched to 50 Ω input impedance

2. **Antenna Placement:**
   - Positioned at the top (receivers) and bottom (transmitters) of the simulation domain Ω
   - Limited to top and bottom to simulate a practical circuit board implementation
3. **Excitation Signal:**
   - Pulse excitation with sawtooth signal
   - Up-chirp time: 433 µs
   - Down-chirp time: 100 µs
   - Inter-chirp waiting time: 100 µs
4. **Tissue Modeling:**
   - Skin: 2 mm thickness, complex dielectric properties from Gabriel database [GLG96]

- Breast fat and tumor: Dielectric properties from Martellosio et al. [MPB+16], high fat subset

The simulation was conducted using CST Microwave Studio 2019, a specialized electromagnetic simulation software. This configuration permits the realistic simulation of radar signal propagation through breast tissue, thereby providing supplementary high-resolution data in conjunction with the EIT simulation.

It is important to note that although this simulation employs fixed antenna positions, real-world applications would necessitate adaptable positioning due to the inherent variations in breast size. The simulation design represents a compromise between practicality and the necessity for consistent data collection. The inclusion of EIT electrodes on the sides provides flexibility for different breast sizes.

4.6.4 Radar Reconstruction

The radar reconstruction process involves two main simulation stages: a reference simulation without tumors and a simulation with tumor inclusions. This process aims to detect and localize potential tumors based on the differences between these simulations.

Reference Simulation

Initially, a reference simulation was conducted without any tumor inclusions:

- Each transmission antenna emitted a pulse signal through the tumor-free medium.
- Receivers at the top captured these signals.
- Reference signals were denoted as $\boldsymbol{h}^0_{a,b} = [h^0_1, h^0_2, ..., h^0_T]$, where:
  - a: index of the transmitting antenna
  - b: index of the receiving antenna
  - T: length of the signal

Inclusion Simulation

Subsequently, a simulation was performed with tumor inclusions:

- In this explanation example, one tumor inclusion was investigated.
- Inclusion signals were denoted as $\boldsymbol{h}_{a,b} = [h_1, h_2, ..., h_T]$, using the same notation as in the reference case.

Reconstruction Algorithm

The reconstruction process follows these steps:

1. Calculate the root-mean-square deviation (MSE) for each transmitter-receiver pair (a, b):

$$RMSD_{a,b} = \sqrt{\frac{1}{T}\sum_{t=1}^{T}(h^0_{a,b}(t) - h_{a,b}(t))^2} \tag{4.27}$$

2. Define vector $RMSD_a = [RMSD_{a,1}, ..., RMSD_{a,B}]$, where B is the number of receivers.

3. Compute the mean of each $RMSD_a$ vector, denoted as $\overline{\boldsymbol{RMSD}}_a$.

4. Filter $RMSD$ values:

$$RMSD^{final}_{a,b} = \begin{cases} RMSD_{a,b} & RMSD_{a,b} > \overline{\boldsymbol{RMSD}}_a \\ 0 & otherwise \end{cases} \tag{4.28}$$

5. Calculate cumulative $RMSD_{a,cum}$ for each receiver position:

$$RMSD_{a,\,cum} = \sum_{b=1}^{B} RMSD^{final}_{a,b} \tag{4.29}$$

6. Estimate tumor position from the resulting curve (Figure 4.7):
   - Construct an envelope of the RMSD curve by interpolating between local maxima.
   - Estimate tumor position by subtracting the envelope from the RMSD curve.

This tumor position estimate serves as a priori information for the D-Bar algorithm, enhancing the overall reconstruction process.

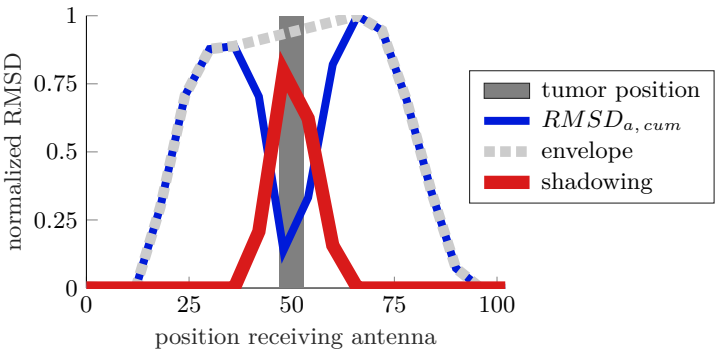


Figure 4.7: Reconstruction of two tumors using the reconstruction algorithm described. The RMSD curve can be seen. The gray dashed line is the envelope that aids in the calculation of the estimated tumor position, which is the red line - adapted from [PMK+20]. The position of the tumor along the y-axis is 27.5 mm and it has a diameter of 8 mm.

4.7 Summary

This chapter provides an in-depth exploration of the D-Bar algorithm, a direct method for solving the inverse problem in EIT. The D-Bar algorithm is unique in its approach, transforming the Laplace equation into a time-independent Schrödinger equation, which encapsulates the conductivity distribution within a new potential. This transformation allows for the direct computation of the conductivity distribution from boundary measurements of voltages and currents. The chapter begins with a detailed mathematical outline of the D-Bar algorithm. The transformation from the Laplace to the Schrödinger equation was explained, along with the utilization of CGO solutions to resolve it. The DtN map was introduced as a pivotal link between boundary measurements and the internal conductivity distribution. The scattering transform, a nonlinear Fourier transform, was then computed from the DtN map, enabling solving of the modified Schrödinger equation and the subsequent recovery of the conductivity distribution.

Practical considerations for implementing the D-Bar algorithm were discussed, including the handling of non-circular domains and the incorporation of data from other imaging modalities to improve reconstruction quality. The numerical implementation involves computing the DtN map, calculating the scattering transform, solving the D-Bar equation, and reconstructing the con-

ductivity distribution. The chapter also addressed the challenges of real-world applications, such as the complexity of hardware design for current injection patterns and the need for corrections in non-circular domains.

A significant proportion of the chapter was devoted to the numerical implementation of the D-Bar algorithm. This included the calculation of the DtN map, the computation of the scattering transform using the exponential approximation, and the solution of the D-Bar equation using matrix-free solvers such as GMRES. The reconstruction of the conductivity distribution was achieved by evaluating the potential function at specific points.

The chapter also examined the fusion of EIT with radar data to enhance the spatial resolution of the reconstructions. The combination of the strengths of both modalities allows the D-Bar algorithm to leverage the deeper penetration of EIT and the higher spatial resolution of radar. This fusion is performed in the nonlinear Fourier domain, where the scattering transform is truncated to include information from both EIT and radar. In summary, this chapter provides a comprehensive overview of the D-Bar algorithm, from its mathematical foundations to its practical implementation and enhancements through data fusion.

The D-Bar algorithm offers a robust and efficient method for EIT, capable of handling practical challenges and improving reconstruction quality through the integration of additional imaging modalities. The detailed explanations and practical considerations presented in this chapter equip the reader with a deep understanding of the D-Bar algorithm and its applications in EIT.

5 Experimental Validation

This chapter presents a comparative analysis of the ANN and the D-Bar algorithm for reconstructing conductivity distributions in EIT. The focus is on evaluating the performance, robustness, and accuracy of these methods under various experimental conditions and noise levels. The ANN has demonstrated significant potential in EIT due to its ability to learn complex patterns within data. The chapter begins with exploring the performance of the ANN in reconstructing conductivity distributions, using metrics such as the AR, PE, and RNG. The ANN algorithm demonstrates greater variability in shape, but greater accuracy and consistency in determining object positions. It also maintains higher quality reconstructions at various SNR, indicating robustness to noise.

The D-Bar algorithm, a well-established theoretical method in EIT, transforms boundary measurements into a conductivity distribution. This chapter evaluates the D-Bar algorithm's performance, particularly focusing on its robustness in the presence of contact impedance and noise. The proposed four-probe D-Bar technique, which excludes measurements from current-carrying electrodes, enhances reconstruction quality. Comparisons between the direct D-Bar algorithm and the proposed method show minimal differences in initial reconstructions, but notable improvements in handling contact impedance.

The chapter illustrates the effectiveness of both the ANN and D-Bar algorithms in reconstructing conductivity distributions through simulations and tank measurements. Furthermore, the integration of a priori data and the impact of contact impedance are also discussed, providing a comprehensive overview of the strengths and limitations of each method in practical EIT applications.

5.1 Artificial Neural Network

The following section presents a comparative analysis of two reconstruction algorithms, GN and ANN, employing a variety of metrics. The potential of these algorithms is assessed through experiments involving tank and pig measurements, with particular emphasis on aspects such as accuracy, noise robustness, and artifact reduction. The results are presented in a quantitative manner in order to highlight the relative strengths and weaknesses of each method.

5.1.1 Random Data

An ANN can only perform as good as the data which it has seen during training. It might be the case that the ANN only retrieves reconstructions seen in the

training data set. In a medical scenario, this can be quite dangerous, as this might lead to false diagnostic conclusions. Thus, at first, random input data should be funneled into the ANN. The output then should not resemble a clear shape. It should be interpretable by a human, that the shown reconstruction is gathered from unuseful data. The random data was chosen such, that the mean and the *std* are aligned with real-world data gathered from pigs in laboratory trials. This resulted in a mean of $8.27{\cdot}10^{-3}$ V and a *std* of $1.26{\cdot}10^{-2}$ V, as shown in Figure 5.1. In the first row, the random inputs of the ANN can be seen. In the second row, the resulting conductivity distribution can be observed. Although the output conductivity distribution is not completely random, the output does not present a close resemblance of an anatomical conductivity distribution. Thus, it probably would be correctly classified as unuseful output data.

5.1.2 Unseen Training Data

A second sanity check whether the ANN has successfully learned the behavior of the underlying relation between the input voltages and the conductivity distribution is to feed yet unseen data, generated from the same strategy is the training data (validation data), into the ANN. This can be observed in Figure 5.2[1]. The top row shows, yet unseen data generated from the same strategy as the training data, the center row represents the ANN prediction and the bottom row visualizes the pixelwise error in the prediction.

The ANN is capable of giving useful predictions of the conductivity distribution. The reconstruction, however, is blurry. This is due to the fact, that EIT has a limited resolution. This results in a high error on the edges of the conductivity targets. If the output of the ANN had been very close to the target conductivity, it would indicate that the ANN would hallucinate the sharp features. This would give a hint, that the ANN has been overfitted. The ANN is even able to predict small spatial features like in the samples 4, 5 or 7. In 6 another effect can be observed, the reconstruction quality degrades the further the conductivity enclosure is near the center of the tank. This is also expected, as the influence of the center to the boundary measurements is less compared to near the electrodes.

[1] GN reconstructions are not shown at this stage, as the presneted results are only a second sanity check whether the ANN is able to recosntruct EIT images at all. In subsequent steps GN, was used for comparison.

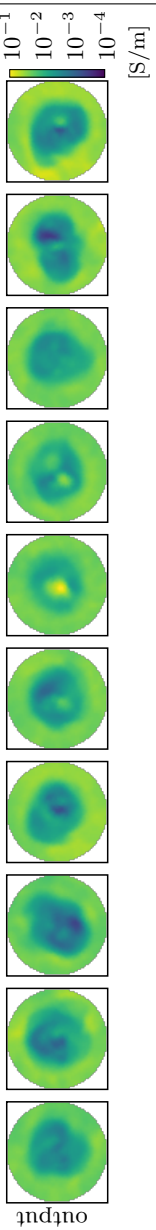


Figure 5.1: ANN predictions for random input data.

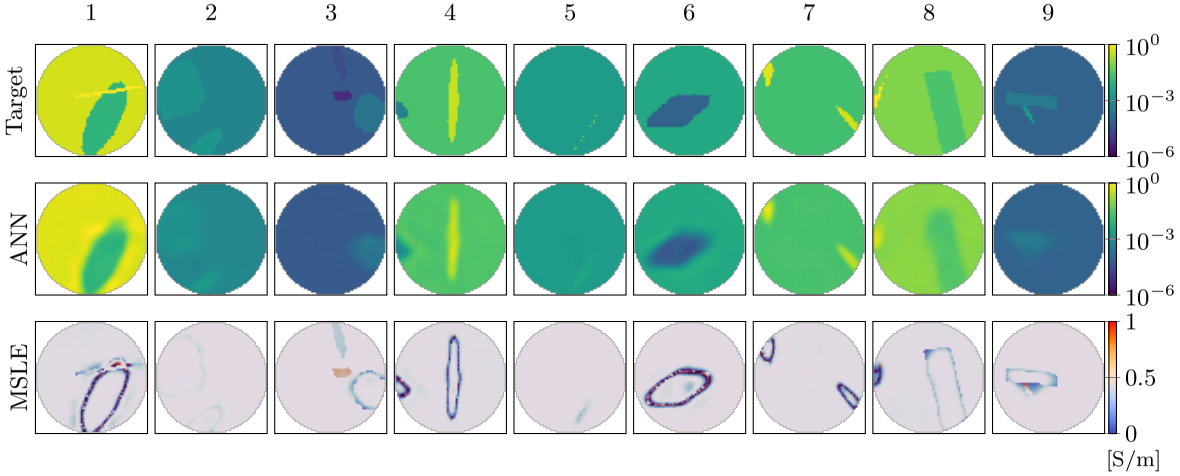


Figure 5.2: Output of the ANN on the validation dataset. The very top row represents the desired conductivity distribution, the middle row shows the predicted output of the ANN. In the very bottom row the pixelwise MSLE is presented.

5.1.3 Simulated Tank Data

The first two tests give a general overview that the ANN is able to make useful predictions. However, of more interest is the quantification of the reconstruction compared to a commonly used algorithm such as GN. To do this, a target was simulated in a circular tank. It was moved from the center to the outer part of the tank. The size of the target was chosen to be about the size of a cucumber in a 29 cm diameter tank. The simulation setup was chosen to ensure comparability between the stimulation results and the tank measurements. No noise was added to the simulations in this step. Figures of merit for these results are given in table 5.1. The visual reconstructions are given in Figure 5.3

Table 5.1: GREIT fom for the simulated FEM tank data. Given are the *mean* $\pm$ *std*.

Algorithm/Metric	**AR**	**PE**	**RNG**
GN	0.069 ± 0.0069	2.7 ± 1.1	0.11 ± 0.0094
ANN	0.066 ± 0.0046	5.6 ± 4.0	0.14 ± 0.019

- **AR**, see equation (2.3.5)
  The *std* of the AR is larger for the GN algorithm than for the ANN. However, it is important to note that the *std* is an order of magnitude lower than the mean. This observation is visually confirmed by the reconstructions shown in Figure 5.3. The AR remains approximately the same for both reconstructions.

- **PE**, see equation (2.3.5)
  For the PE, the GN algorithm has a lower mean and *std* compared to the ANN model. Specifically, the mean PE for GN is half that of ANN, while the *std* is a quarter.

- **RNG**, see equation (2.3.5)
  The RNG for the GN algorithm is also lower compared to the ANN model. This can be seen in the images, where the RNG for the ANN is larger due to the larger differences in size of the artifacts outside the $\boldsymbol{m}$ mask.

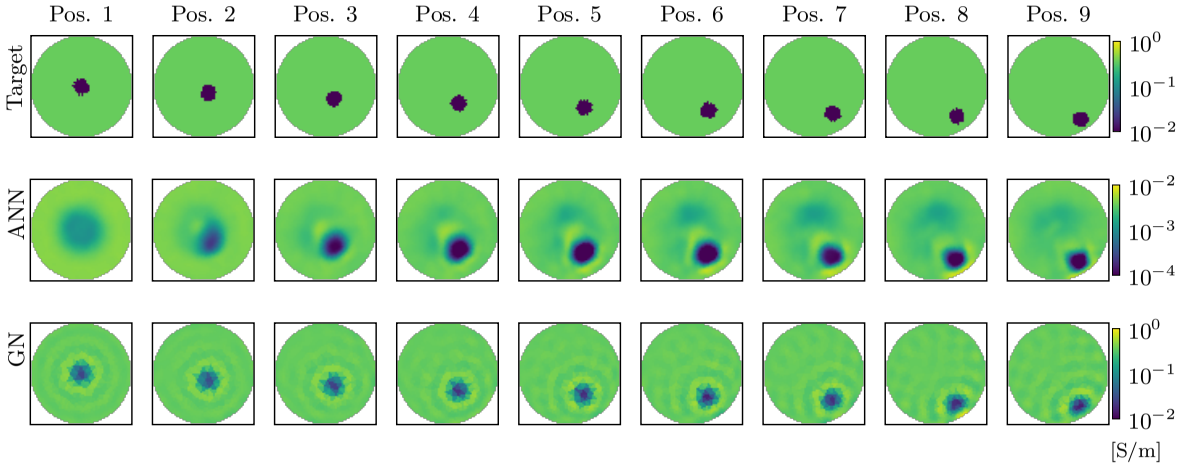


Figure 5.3: Illustration of ANN (**middle**) and GN (**bottom**) reconstructions of FEM that mimic the position of the tank pickle data without any noise. The ground truth target positions are given at the (**top**).

5.1.4 Noise Performance

The noise performance of the ANN will now be compared with GN. A target was positioned near the boundary of the FEM domain and the measurements were simulated. These were subsequently fed into the ANN and GN. Figure 5.4 shows the results. The reconstructions obtained by ANN are more robust to noise than those obtained by GN. At an SNR of 100, the GN reconstruction is barely visible, while the ANN reconstruction remains clearly discernible. This indicates that the ANN can maintain a higher quality reconstruction in the presence of noise. At an SNR of 25, the ANN reconstruction starts to degrade and becomes less visible. Ringing artefacts outside the target increase compared to the higher SNR reconstructions. At even lower SNR values, the reconstruction of the circular target itself is deformed by the ANN. However, it is still significantly better than GN. The artefacts are more pronounced and the target is not visible at all in the GN reconstruction.

5.1.5 Tank Measurements

As shown in Figure 5.5, the pickle was moved from the center to an electrode. This movement was carefully controlled to ensure accurate measurements and to observe the effect of the displacement on the reconstruction algorithms.

The reconstruction using the GN algorithm shows a more diffuse boundary, indicating that the algorithm may have limitations in precisely defining the edges of the object. This diffuse boundary suggests that the GN algorithm may be averaging conductivity values over a larger area, resulting in a less sharp characterization of the edges of the pickles (which is a spatial low pass property). In contrast, the ANN algorithm characterizes a clearer boundary, suggesting that it is more effective at capturing the precise location and shape of the pickle. This clearer boundary is probably due to the ANN's ability to learn complex patterns and relationships within the data, allowing it to reconstruct a single object's shape more accurately.

Table 5.2: Figures of merit for the tank experiment. The left number in each cell is the *mean* of the metric, while the right number is its *std*.

Algorithm/Metric	**AR**	**PE**	**RNG**
GN	0.1 ± 0.0056	11 ± 5.7	0.1 ± 0.0045
ANN	0.14 ± 0.0086	7.1 ± 2.9	0.08 ± 0.0054

The background noise in the GN algorithm's reconstruction is characterized by numerous small perturbations due to the algorithm's sensitivity to small

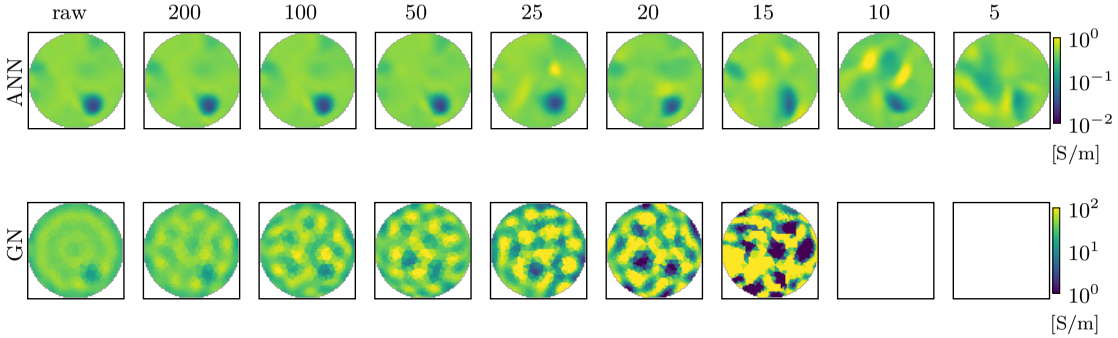


Figure 5.4: Evaluation of the noise performance of ANN (**top**) compared with GN (**bottom**). The columns represent different noise levels (values printed above each column, with "raw" meaning no noise) added with the EIDORS function `add_noise`. The target position is equal to position 6 in Figure 5.3.

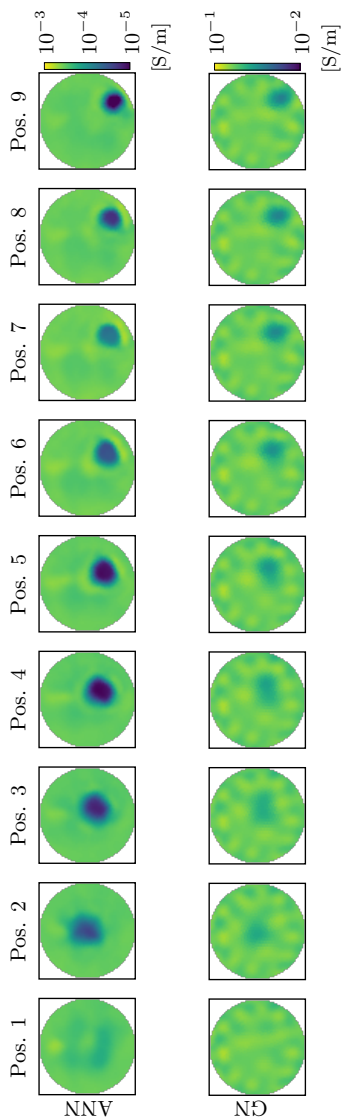


Figure 5.5: Illustration of ANN and GN reconstructions on the pickle measurements of the tank dataset. The empty measurement was not used in both reconstructions, and is given only for a better view of the reconstruction artifacts. 1 is the position of the center pickle, while 9 is the outer most pickle.

variations in the data. These disturbances can obscure the true signal and make it difficult to interpret the results. On the other hand, the background of the ANN algorithm has fewer disturbances, with one prominent disturbance at the top and another surrounding the conductivity envelope. This reduction in background noise suggests that the ANN algorithm is better at filtering out irrelevant information and focusing on the significant features of the data. The presence of the two perturbations in the ANN background may indicate specific areas where the algorithm's performance could be further improved.

These qualitative observations are supported quantitatively by the performance figures listed in table 5.2. The *mean* and *std* of the AR of the ANN algorithm are higher than those of the GN algorithm, as can be visually confirmed in Figure 5.5. This is due to the fact that the fom are calculated for each reconstruction. The overall values of GN are closer together, which results in a slightly higher AR values.

Conversely, the PE and its *std* are lower for the ANN algorithm. Specifically, the *mean* PE of the ANN algorithm is about 35% lower than that of the GN algorithm, and the *std* of the PE is about 50% lower. This significant reduction in the PE and its *std* suggests that the ANN algorithm may be more accurate and consistent in determining the position of the object.

5.1.6 Pig Measurements

For the experimental data, only a qualitative analysis is provided, as this has been a preliminary investigation on experimental test data. The results are shown in figure 5.6. On the left, a CT measurement is shown to better evaluate the results. In the middle, the mean reconstruction over 20 seconds of mechanical ventilation is shown. An artefact in the reconstruction can be seen at the top. The two lungs are visible, but appear smaller than their original size. The heart, located between the lungs and the artefact, corresponds to the position in the CT image. The *std* image on the right confirms the findings. The artefact remains in the same position as the *std* at this location is close to zero. A high *std* is observed at the position of the heart, and the same is true for the lungs. The shape of the *std* image for the lungs more closely resembles the general shape of the lungs.

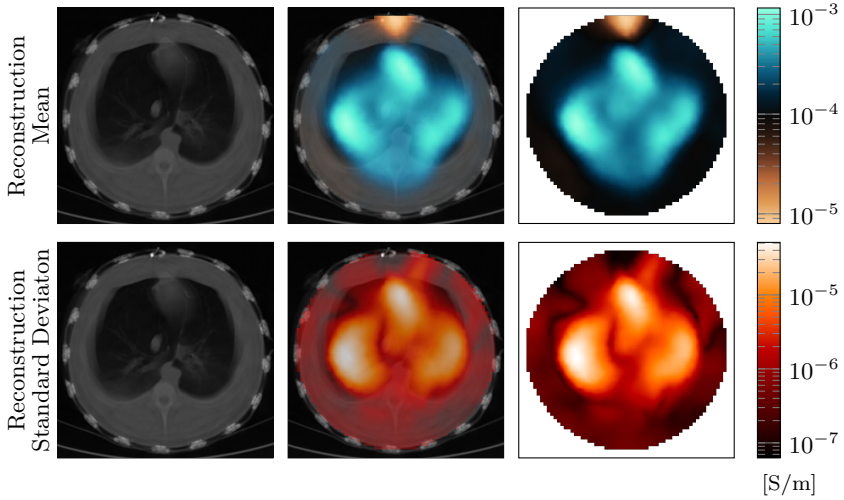


Figure 5.6: Comparison of ANN reconstruction with CT images. The top row compares shows the mean absolute conductivity reconstruction over the span of 20 seconds, the lower row shows the *std* over the same time span. The very left column shows the CT image, the middle column shows the reconstructions layered a top of the CT image and the very right column shows soley the image without any distraction from the CT image.

5.2 D-Bar under 4-probe Measurements

5.2.1 Simulation without Contact Impedance

In order to simulate the adjacent measurements, a circular two-dimensional tank with 16 electrodes was created using EIDORS. Seven targets were then placed in the tank, distributed equally from the center to the outer boundary. This setup was designed to replicate the actual tank measurements. The empty tank and each target were simulated using the adjacent-adjacent pattern to obtain 208 voltage measurements. Subsequently, the aforementioned measurements were input into the GN algorithm to determine the simulated conductivity values, which were denoted as $\sigma_{sim,\,i}$. Each of these conductivity values was then used to simulate the full set of measurements, which were denoted as $u_{full,\,i}$. These full sets of measurements were then utilized to create the DtN maps, which were employed to recover the conductivity distribution through the D-Bar algorithm.

Figure 5.7: Simulation of the proposed reconstruction technique without contact impedance. The first row is the position of the actual target. The second row is the reconstruction from measurements, including measurements on current-carrying electrodes. The last row is the reconstruction using the proposed technique.

The results of the reconstructions for the simulation without additional contact impedance are shown in Figure 5.7. This figure is divided into three distinct rows, each representing different stages and methods of reconstruction. The top row shows the ground truth position of the target, which serves as a reference for evaluating the accuracy of the reconstruction methods. This ground truth is essential for understanding the deviations and accuracy of subsequent reconstructions. The middle row shows the direct reconstruction obtained using the D-Bar algorithm. This algorithm uses measurements from current-carrying electrodes, which are an integral part of the reconstruction process. The use of live electrodes ensures that the data has more information, resulting in a more accurate reconstruction. The bottom row shows the reconstruction using only measurements from non-current electrodes. These measurements are then processed by the proposed method within the framework of the D-Bar algorithm. This approach is innovative as it attempts to reconstruct the conductivity distribution using a subset of the available data, specifically excluding the direct influence of live electrodes. This method is particularly useful in scenarios where measurements from current-carrying electrodes are either unavailable or unreliable. A comparison of the two reconstruction techniques shows that the differences are very small. The minima and maxima in both reconstructions are very close, indicating that the proposed method is almost as effective as the direct D-bar algorithm. Specifically, the minimum value in the reconstructed conductivity distribution differs by about 4% between the two methods. This small variation suggests that although the proposed method is highly accurate, there is a small degree of deviation that could be attributed to the exclusion of current carrying electrode measurements. Furthermore, the maximum value in the reconstructions differs by only 0.1%. This negligible difference highlights the robustness of the proposed method in accurately capturing conductivity peaks. The ability to maintain such close maxima values indicates that the proposed method can effectively reconstruct the essential features of the conductivity distribution.

5.2.2 Simulation with Contact Impedance

The simulation including the contact impedance was conducted the same way as in the case of the no contact-impedance. The only difference was that a contact impedance of $7\,\Omega$ was added to each electrode (higher values resluted in a rapidly degrading reconstruction quality, which did not yield any meaningfull results to analyze). The voltage measurement on current driven electrodes are then expected to be too high, which in turn can have a profound negative impact on the reconstructions. The results for the added simulated contact impedance can be seen in Figure 5.8. This figure provides a detailed compari-

Figure 5.8: Simulation of the proposed reconstruction technique with a simulated contact impedance of 7. The first row is the position of the actual target. The second row is the reconstruction from measurements, including measurements on current-carrying electrodes. The last row is the reconstruction using the proposed technique.

son of the reconstructions obtained using the direct D-Bar algorithm and the proposed method using measurements from non-current-carrying electrodes. In the first four reconstructions, the images produced by both techniques appear quite similar, indicating that the presence of contact impedance does not significantly affect the initial reconstructions. However, as the reconstructions progress, notable differences begin to emerge. In particular, the reconstructions obtained using the direct D-Bar algorithm show a compression effect perpendicular to the domain boundary. This compression becomes more pronounced as the target moves closer to the boundary. This phenomenon can be attributed to the sensitivity of the D-Bar method to boundary conditions and the influence of the contact impedance on the measurements. Another significant observation is the change in the distance between the maximum and minimum values in the reconstructed conductivity distributions. In the presence of contact impedance, the difference between these values is reduced to only 0.2%. This is in stark contrast to the case without contact impedance, where the difference was 25%. This reduction suggests that the contact impedance has a homogenizing effect on the reconstructed values, potentially smoothing out the variations in conductivity. The proposed reconstruction pipeline, which relies solely on measurements from non-current-carrying electrodes, does not exhibit the truncation effect observed in the direct D-bar reconstructions. This suggests that the proposed method is more robust to the presence of contact impedance. However, it is noted that the difference between the maximum and minimum values begins to shrink slightly, indicating a slight loss in the dynamic range of the reconstructed values.

5.2.3 Tank Measurements without Contact Impedance

The Sciospec EIT 32 medical version by Sciospec Scientific Instruments GmbH, Bennewitz, was used for all tank measurements. Although this device is capable of connecting 32 electrodes to the tank, only 16 electrodes were used. This choice reflects the most common settings found in real-world applications and literature studies, ensuring that the results are comparable and relevant. A carrot immersed in salt water was used as the target. The carrot was positioned identically to the simulation setup, initially placed in the center of the tank and then moved in six incremental steps towards the boundary. This systematic movement allowed a comprehensive analysis of the reconstruction algorithms under varying conditions. The Sciospec EIT 32 instrument is capable of collecting voltages from live electrodes. However, in order to test the proposed algorithm, the voltages from the current-carrying electrodes were deliberately excluded from the measurements. This exclusion was necessary in order to evaluate the performance of the proposed method, which relies solely

on data from the non-current-carrying electrodes. The collected data were then processed using the proposed algorithm. To provide a comparative analysis, the results obtained from the proposed algorithm were compared with those obtained from the D-bar reconstruction, which included measurements from the current-carrying electrodes. However, in order to make this comparison, the potential at each electrode had to be calculated from the adjacent measurements[2]. The potentials on the electrodes were collected through

$$w_i = \begin{cases} \frac{1}{i} \Big/ \sum_{j=1}^{N-1} \frac{1}{j} & \text{for direct path} \\ \frac{1}{N-i} \Big/ \sum_{j=1}^{N-1} \frac{1}{j} & \text{for indirect path} \end{cases}, \tag{5.1}$$

$$V_i^k = \frac{1}{2} \left[\sum_{j=1}^{i-1} w_j \Delta V_j^k + (-1) \sum_{j=i}^{N-1} w_j \Delta V_j^k \right], \tag{5.2}$$

$$V_i^k \leftarrow V_i^k - \frac{1}{N} \sum_{j=1}^{N} V_j^k, \tag{5.3}$$

where V_i^k denotes the potential on the electrode i for the k^{th} current stimulation. This method was chosen because it is less susceptible to noise, thus ensuring more accurate potential calculations. The rationale behind this method is rooted in the need to mitigate the effects of noise on the measurements. By calculating the potentials from adjacent measurements, the method exploits the inherent redundancy and correlation in the data, which helps to average out the noise and improve the robustness of the reconstruction. The results of the measurements can be seen in Figure 5.9. The overall difference between the direct D-bar reconstruction technique and the proposed reconstruction method is minimal. However, specific differences can be observed in rows 6, 7 and 8. In these rows, the proposed reconstruction technique shows a larger white area in the upper right of the reconstructions The values for the reconstructed pixels deviate more from 1 in the direct reconstruction technique, where 1 represents the baseline conductivity with no change. This deviation suggests that the direct reconstruction approach has more ringing artifacts around the target, which are oscillatory distortions that can obscure the true conductivity distribution (this can be seen in Figure 5.9 as a yellow ring around the target). By contrast, the proposed reconstruction technique, which excludes measurements from current-carrying electrodes, does not exhibit these ringing artifacts, resulting in cleaner and more accurate reconstructions. This suggests that the

[2] The Sciospec device is capable of measuring the potential at the electrodes rather than the voltage difference, but we decided to stay with the adjacent-adjacent measurement mode to better compare the results with systems that measure voltage differences.

Figure 5.9: Tank measurement of a carrot in a tank without any additional contact impedance. The first row is the position of the actual target. The second row is the reconstruction made from measurements, including measurements on current carrying electrodes. The last row represents the reconstruction with the proposed technique.

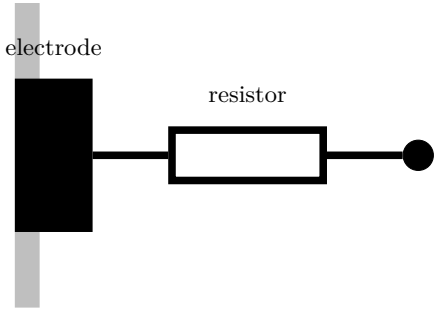


Figure 5.10: Visualization of the connection between electrode and resistor in the tank. The gray area represents the tank.

proposed method is more robust and less prone to bias than the direct D-bar reconstruction approach.

5.2.4 Tank Measurements with Contact Impedance

To increase the realism of the tank data, subsequent tank measurements were made with an additional resistor connected to each electrode. This experimental setup is illustrated in Figure 5.10. In this figure, the gray area represents the tank wall, while the thick black square represents the electrode embedded in the tank. The resistor was connected to the electrode, and then the instrument was connected to the resistor.

A wide range of values for contact impedance can be found in the literature. A common observation is that the contact impedance decreases as the measurement frequency increases. Another important factor influencing the contact impedance is the type of electrode used. Yang et al. carried out a comparative study of the resistance of different types of electrodes, including wet electrodes, semi-dry electrodes and dry electrodes, in terms of their resistance characteristics [YGZ+22]. Their results indicate that under optimal conditions, the contact impedance can be in the range of several hundred ohms (Ω). Another study by Yang et al. reports even lower contact impedance values, closer to 100 Ω [YDX+17]. Similarly, Cameron et al. observed contact impedance values in the range of hundreds of ohms under optimal conditions [CFPH23]. Based on these findings, an initial resistance value of 100 Ω was chosen for the measurements, as this resembles an optimistic value. If the direct reconstruction with the D-Bar algorithm does not work there, then higher values are even more disturbed. The measurements with an additional contact impedance of

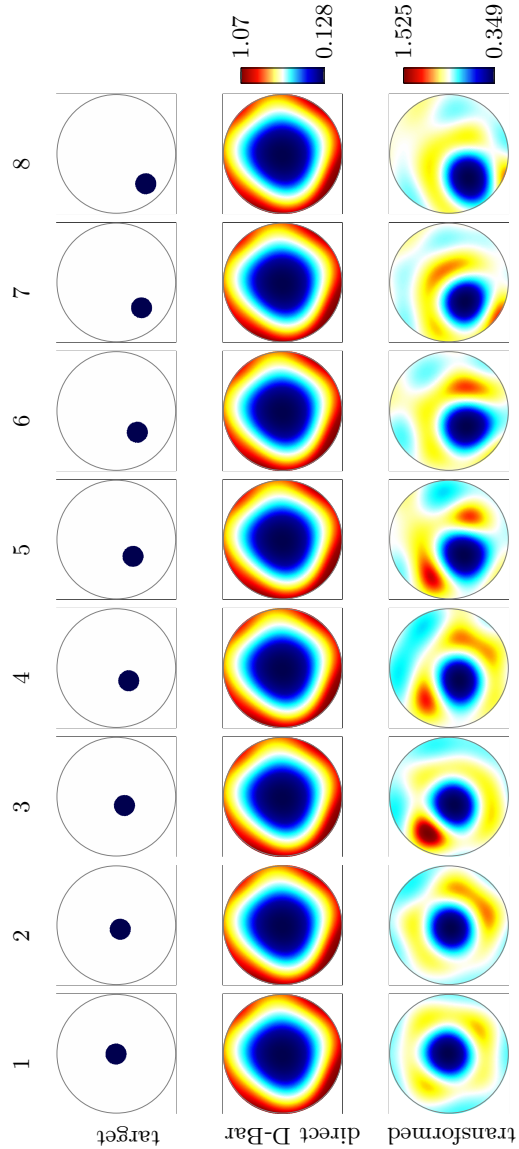


Figure 5.11: Tank measurement of a carrot in a tank with 100 Ω added to each electrode. The first row is the position of the actual target. The second row is the reconstruction from measurements, including measurements on current-carrying electrodes. The last row is the reconstruction using the proposed technique.

100 Ω are shown in Figure 5.11. In this scenario, the target is not visible in any of the direct reconstructions. Conversely, in the proposed approach, the targets remain observable as they move from the center towards the boundary. However, it is noteworthy that the ringing artifacts around the target are more pronounced compared to the case without the added contact impedance.

5.3 Time-independent D-Bar (absolute)

In order to thoroughly evaluate the described absolute D-Bar technique, data from different ANN approaches were used. This was done to demonstrate that the technique is effective not only on the Sciospec device, but also on other devices that are more widely used in the field. A Dräger EEK 2, the pre-series version of the Dräger Pulmovista 500, was used for data collection.

In the experimental setup, a carrot was incrementally moved from the center of a tank to its outer edge in nine discrete steps. Figure 5.12 shows the reconstructions obtained from the experiment. The top row shows the actual positions of the carrot, the middle row shows the absolute D-bar reconstructions, and the bottom row shows the intermediate step $\boldsymbol{\sigma} sim$ of the proposed 4-probe D-bar technique (see section 4.3.3 and Figure 4.4). This intermediate step is included to demonstrate that the proposed reconstruction scheme does not rely on an exact GN reconstruction to obtain $\boldsymbol{\sigma} sim$. Instead, this technique is designed to approximate the physical behavior of the FEM model.

The reconstructions indicate that the general position of the target is accurately captured. The movement of the carrot from the center to the edge is clearly reflected in the absolute D-bar reconstructions. However, it is observed that the size of the target appears larger in the reconstructions compared to its actual size.

It is important to note that the intermediate step $\boldsymbol{\sigma}_{sim}$ does not depend on an accurate reconstruction. The conductivity distribution itself does not seem to give useful results, which underlines the importance of the proposed technique in approximating the physical behavior rather than relying on accurate GN reconstructions. In summary, the absolute D-bar technique demonstrates a robust ability to accurately track the position of the target, even when the size of the target is severly overestimated. The intermediate step $\boldsymbol{\sigma}_{sim}$ effectively approximates the physical behavior of the FEM model, validating the effectiveness of the proposed reconstruction scheme.

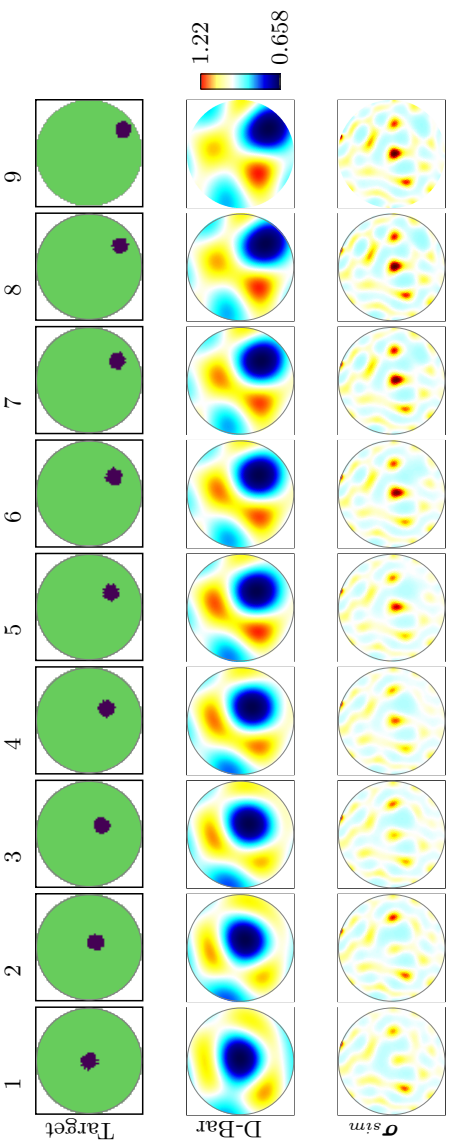


Figure 5.12: Reconstruction of the D-Bar algorithm using only four-probe measurements. In the top row the target position is given. In the middle row the D-Bar reconstruction is given and in the bottom row the intermediate result if given.

5.4 Time-independent D-Bar (frequency-differential)

The following experimental setup was used to evaluate the feasibility of the D-Bar algorithm as a frequency difference reconstruction algorithm. The same water tank and measurement configuration as described in section 5.2 was used. However, it is important to note that the measurements were made at different frequencies. Specifically, the frequency difference reconstruction was performed at $10,000$ kHz and $79,432.8kHz$. This frequency range was chosen in order to negate the frequency dependence of water, as confirmed by the study conducted by Grasso et al. in 1990 [GMT90]. In addition, it is well documented that carrots exhibit a decrease in resistance (or an increase in conductivity) in this frequency range [KHVS15]. For each frequency, voltage measurements were collected according to the scheme outlined in the section 5.2.3. In subsequent processing using the D-Bar algorithm, the high frequency component was denoted as $\boldsymbol{L}_\sigma$, while the low frequency component was denoted as $\boldsymbol{L}_1$. Given the known increase in carrot conductivity with frequency, a value greater than 1 was expected for the region containing the carrot. Thus, the frequency dependent conducitivty σ contrast was used. Figure 5.13 illustrates the reconstructions obtained using the frequency-differential D-Bar algorithm. In general, the reconstructions match the expectations. The lower bounds are close to 1, with a minimum value of 0.955, indicating minimal ringing artifacts. Ideally, a value of 1 (the neutral element in the D-Bar algorithm) would be expected. At the location of the carrot, a positive change in conductivity is expected and is indeed observed in all reconstructions. The maximum value in this region is 1.141, providing a clear contrast. The movement of the target from the center to the boundary is accurately depicted, although the steps of movement appear slightly compressed near the boundary. In addition, the overall position relative to the direction of motion is slightly off, with the target moving slightly too far to the left, resulting in an x-position that is slightly too far to the right. In summary, despite the novel use of the D-Bar algorithm for frequency difference reconstruction, the results are consistent with the expected magnitudes of conductivity. The only notable discrepancy is a minor positional drift.

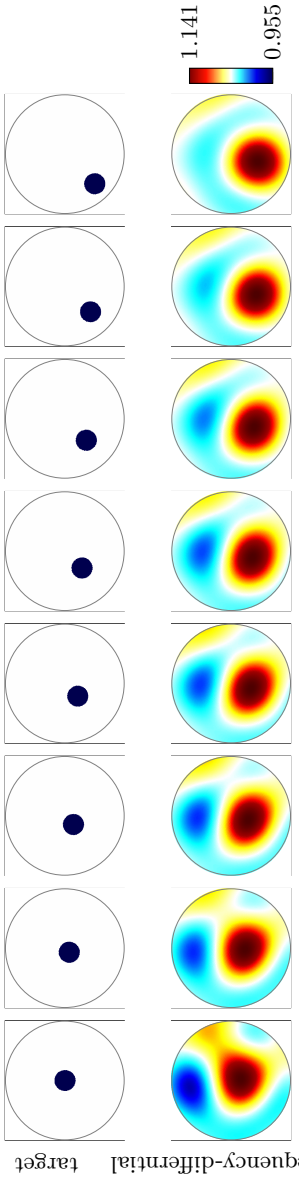


Figure 5.13: Reconstruction of the frequency differential version of the D-Bar algorithm for frequencies of 10,000 kHz and 79,432.8 kHz. In the top row, the position of the carrot is given. In the bottom row, the D-Bar reconstruction is given.

5.5 D-Bar and a-priori Data

5.5.1 Base Reconstruction

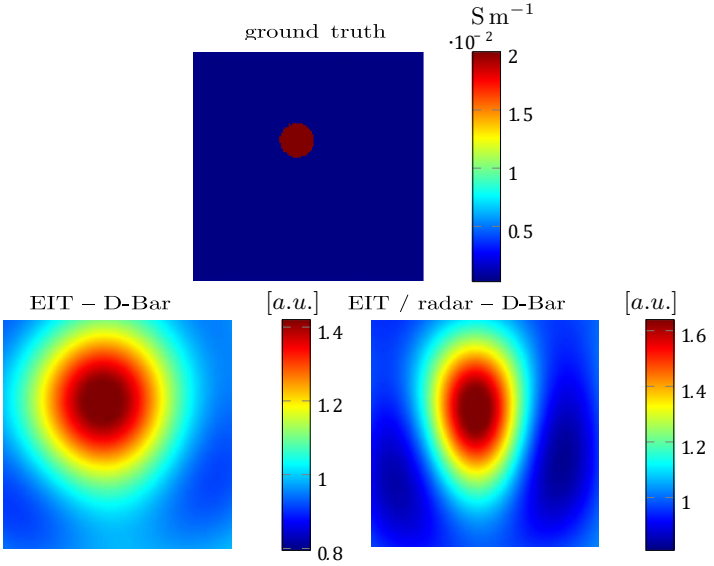


Figure 5.14: The top image depicts the ground truth of the conductivity enclosure. The bottom left image displays an EIT reconstruction with no noise added and $R_1 = 3$. It should be noted that there is no *a-priori* information present in the image. The bottom right image represents a combined reconstruction with *a-priori* information, with a truncation radius $R_2 = 4$.

First, an example of an EIT reconstruction within our quadratic domain was presented. To achieve these reconstructions, the D-Bar algorithm, as described in the Methods section, was used. The resulting reconstruction is shown in Figure 5.14, specifically in the lower left corner. It should be noted that the EIT reconstruction of the target appears larger than the actual ground truth. Throughout this work, the truncation radius was chosen empirically to better illustrate the effects of the reconstruction process. To further demonstrate the performance of reconstruction on multiple targets, an additional plot has been included in Figure 5.15, which shows two targets under the same settings. A similar characteristic of improved resolution along the x-axis is shown in this plot. The values obtained from the reconstructions fell within the range

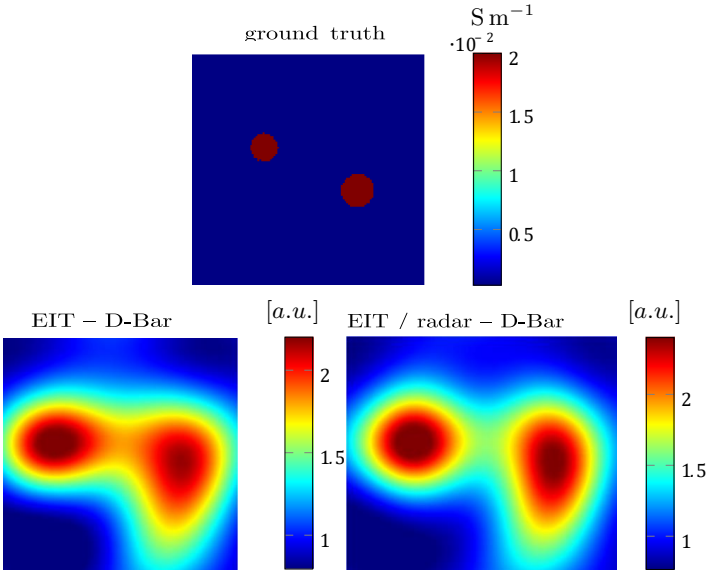


Figure 5.15: Top: Ground truth of the two conductivity enclosures. Bottom left: EIT reconstruction without added noise and $R_1 = 3$. Note: There is no *a-priori* information in the image. Bottom right: combined reconstruction with *a-priori* information and a truncation radius of $R_2 = 4$. From Rixen et al. [RLM+23].

typically reported in the literature [IMNS04], [HMA17], thus validating the approach and results.

In order to analyze the GREIT fom, the EIT and radar reconstruction were compared for an EIT truncation radius of $R_1 = 3$ without noise. The fom can be seen in Figure **??**.

When R_1 was fixed and R_2 was increased, it was observed that, initially, the results were more favorable, but after $R_2 = 4.5$, the fom exhibited a reversal of this trend, with some figures becoming less favorable (**PE** and **SD**) and others marginally more favorable. This behavior appeared anomalous, but it should be noted that the radar information was only available along the x-axis. Consequently, the greater the quantity of radar information, the more the reconstruction was narrowed down along the x-axis, while simultaneously being expanded along the y-axis. This resulted in an increase in the **PE** as the center of gravity of the quarter amplitude set was drawn to the center of the y-axis. The same held true for the **SD**, as the reconstruction is stretched along

the y-axis. The behavior of the **AR** and **RES**, however, became more favorable as more radar information was added. This can be explained as follows. As the radar information contained solely values from the k-space with $R_1 < |k|$, only the fine detail components were incorporated into the reconstructed image. Consequently, the area of the reconstruction decreased, which resulted in an increase in the aforementioned metrics. Nevertheless, the optimal value for R_2 in the experimental setup was determined to be approximately 4.0.

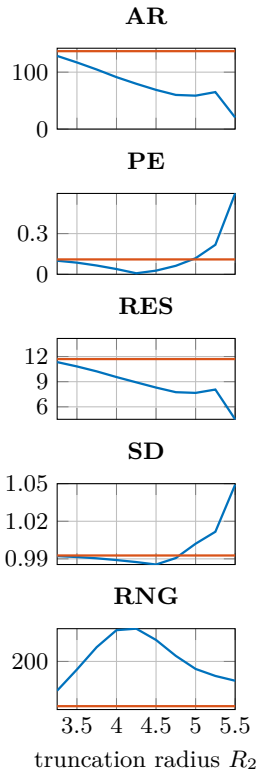
5.5.2 Reconstruction under Noise

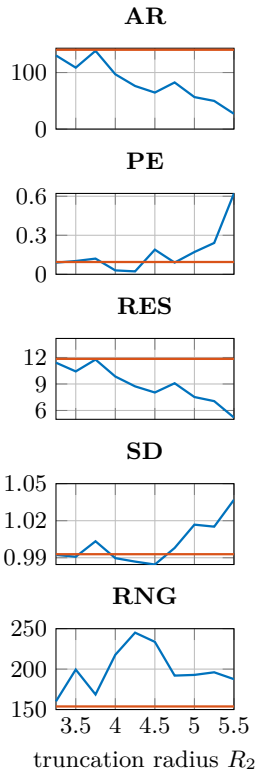
As a second reconstruction example, an EIT reconstruction was performed with a regularization parameter of $R_1 = 3$. To evaluate the robustness of the reconstruction process, a noise level of 0.75% was introduced. The results of this experiment, including the ground truth, the EIT reconstruction and the combined reconstruction with radar data, are shown in Figure 5.16. Compared to the results shown in Figure 5.14, the EIT reconstruction appears more blurred in this scenario. This blurring effect is probably due to the added noise, which affects the clarity and precision of the reconstruction. However, the combined reconstruction, which integrates radar data, shows a significant improvement. In particular, the combined reconstruction is thinner along the x-axis, indicating that the integration of radar data helps to mitigate some blurring caused by noise.

However, when 0.75% noise was added, increasing R_2 initially did not provide additional spatial information, as all the performance metrics remained in a plateau until approximately $R_2 = 4$. Subsequently, the performance metrics exhibited the same behavior as in the no-noise case.

5.5.3 Conductivity Variation

As a third example, the effect of incorporating *a-priori* information into the reconstruction process was investigated. Two separate reconstructions were performed, each using different estimates of the conductivity in the *a-priori* data. The results of these reconstructions are shown in Figure 5.17. In the first scenario, an underestimation of the conductivity with a scale factor of 0.001 was applied. The resulting reconstruction is very similar to the one shown in figure 5.14, suggesting that the underestimation does not significantly alter the quality of the reconstruction. In contrast, the second scenario involved an overestimation of the conductivity. The resulting reconstruction in this case bears a strong resemblance to the combined reconstruction shown in Figure 5.16. This similarity suggests that overestimating the conductivity in the *a-priori* data can produce results similar to those obtained by combin-


AR
100
0
PE
0.3
0
RES
12
9
6
SD
1.05
1.02
0.99
RNG
200
3.5
4
4.5
5
5.5
truncation radius R_2


AR
100
0
PE
0.6
0.3
0
RES
12
9
6
SD
1.05
1.02
0.99
RNG
250
200
150
3.5
4
4.5
5
5.5
truncation radius R_2

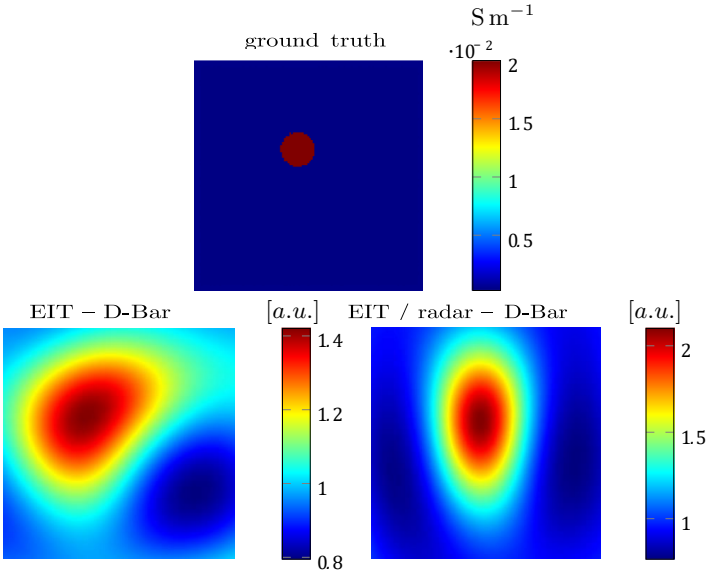


Figure 5.16: The top image depicts the ground truth of the conductivity enclosure. The bottom left image displays an EIT reconstruction with noise added at a rate of 0.75% and a $R_1 = 3$. The bottom right image presents a combination of noisy EIT data and radar data, where the truncation radii of $R_1 = 3$ and $R_2 = 4$, respectively. The noise was added to the electrode voltages as a percentage of 0.75% according to EIDORS add_noise function.

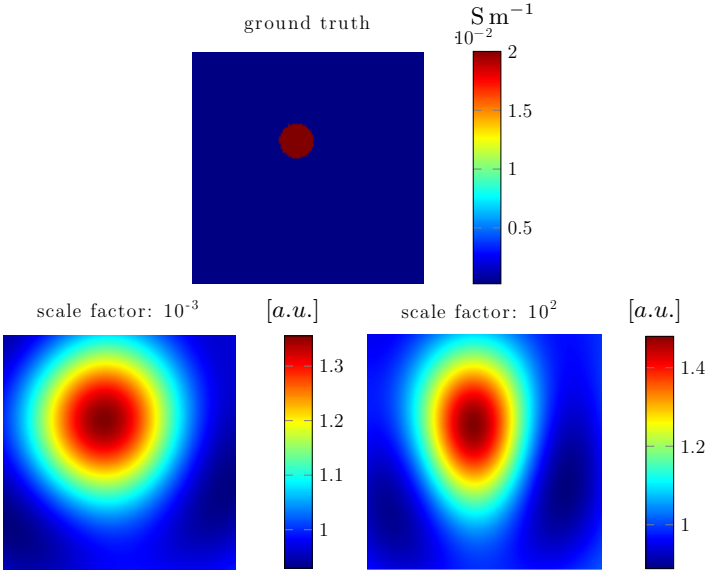


Figure 5.17: The diagram illustrates the discrepancy between the ground truth conductivity and the reconstructed conductivity. The ground truth conductivity is displayed at the top, while the reconstructed conductivity is shown at the bottom left. The reconstruction is a combined reconstruction with $R_1 = 3$ and $R_2 = 4$. It can be observed that the original conductivity of the enclosure is underestimated by a factor of 0.001. In the lower right, another combination reconstruction with $R_1 = 3$ and $R_2 = 4$ is presented. In this case, the original conductivity of the enclosure is overestimated by a factor of 100.

ing EIT with radar data, potentially improving the accuracy and detail of the reconstruction. This estimation of the conductivity is a mandatory step, as the *a-priori* radar data does not provide any meaningful magnitude of the underlying conductivity. Next, the according GREIT fom are analyzed. While the conductivity estimate of the *a-priori* radar data for the previous plots was taken from literature, the conductivity estimate for the radar was now altered to see its effect on the reconstructions. The estimated conductivity from the radar measurements was scaled by $\gamma := 0.001,\ 0.01,\ 0.1,\ 1,\ 10$. R_1 was set to 3 and R_2 was set to 4, while no noise was used. The results can be seen in Figure 5.18. The same qualitative behavior was observed for **AR**, **PE**, **RES**, and **SD**. A plateau is formed from 0.001 to 0.01, and a decrease starts for λ from 0.01 to 1. From 1 to 100, the values build a plateau and increase only slightly. For practical use, a non-linear estimation algorithm for the estimation of the *a-priori* conductivity was developed by Alsaker et al. [AM18].

Thus, it tends to be better to overestimate the conductivity of the included target. This benefit is, however, very small, which makes the process of incorporating *a-priori* data more robust.

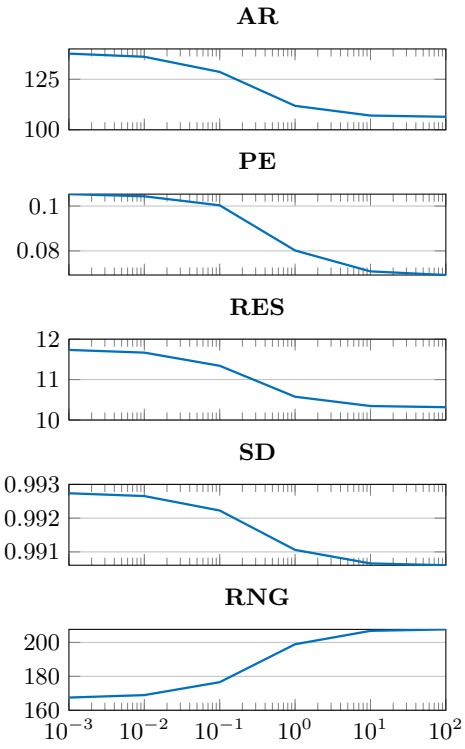


Figure 5.18: GREIT fom for the combination of EIT and radar data for $R_1 = 3$ without noise and $R_2 = 4$. The radar estimation conductivity was changed and scaled by $\gamma := \{0.001,\ 0.01,\ 0.1,\ 1,\ 10\}$. The x-axis is scaled logarithmically.

5.6 Summary

The chapter provided a comprehensive analysis of the D-Bar algorithm and its application in EIT for reconstructing conductivity distributions. It primarily evaluated the performance of the proposed 4-probe D-Bar technique against traditional methods under various experimental setups and conditions. The chapter began by comparing absolute D-Bar reconstructions with intermediate steps ($\boldsymbol{\sigma}_{sim}$), demonstrating the method's effectiveness in approximating the physical behavior of the FEM model. The absolute D-Bar technique accurately tracked the target's position but tended to overestimate its size. A significant focus was placed on the impact of contact impedance on reconstructions. The presence of contact impedance caused a compression effect perpendicular to the domain boundary and reduced the difference between maximum and minimum values in the reconstructed conductivity distributions. The proposed method, which excluded measurements from current-carrying electrodes, showed robustness against contact impedance, maintaining observable targets even when direct reconstructions failed.

The frequency-differential D-Bar algorithm was also tested, demonstrating the expected changes in conductivity at the location of the carrot with minimal ringing artifacts. Simulations without contact impedance and with added contact impedance validated the proposed method, indicating minimal differences between the direct D-Bar and the proposed method, thereby confirming the latter's effectiveness. Tank measurements with and without contact impedance further demonstrated the proposed method's ability to handle real-world conditions and maintain accurate reconstructions.

The chapter discussed the noise performance of the ANN compared to the GN algorithm, demonstrating that the ANN was more robust to noise and maintained higher quality reconstructions at various SNR levels. Furthermore, the incorporation of a-priori data into the reconstruction process was explored, indicating that overestimating the conductivity in the a-priori data could improve the accuracy and detail of the reconstruction.

Quantitative metrics (AR, PE, RNG) were provided to enable the comparison of the performance of different reconstruction techniques, thereby highlighting the strengths and weaknesses of each method. The proposed 4-probe D-Bar technique demonstrated robust performance in reconstructing conductivity distributions, particularly in the presence of contact impedance and noise. The method's ability to exclude measurements from current-carrying electrodes and still produce accurate reconstructions made it a valuable tool for EIT applications. The integration of a-priori data further enhanced the reconstruction quality, providing a comprehensive approach to solving the inverse problem in EIT.

6 Discussion

This thesis presents a discussion of the results of research conducted on the application of the D-Bar algorithm and ANNs for EIT. The primary focus of the research was on enhancing the accuracy and robustness of EIT reconstructions, particularly in scenarios where computation time is not a factor. The key findings and contributions can be summarized as follows:

6.1 Artificial Neural Networks for time-independent Reconstructions

6.1.1 Proposed ANN Architecture

The ANN architecture was specifically designed to address the non-linear and ill-posed nature of the EIT inverse problem. By leveraging the rotational symmetry of the adjacent-adjacent pattern and minimizing the number of trainable parameters, the ANN demonstrated significant potential in providing accurate time-independent reconstructions based solely on simulated FEM data.

6.1.2 Simulation Data

Extensive simulations using FEM were conducted to generate training data for the ANN. The network was trained on a variety of conductivity distributions, ensuring its ability to generalize well to different scenarios. The results indicated that the ANN could effectively handle various noise levels and hardware limitations, making it a promising tool for practical EIT applications. The ability of the ANN to generalize across different scenarios and maintain performance under varying conditions highlights its robustness and adaptability. Nevertheless, the reliance on simulated data raises questions about the ANN's performance with real-world data, which may present unforeseen challenges.

6.1.3 Performance Evaluation

The ANN was evaluated against the GN algorithm, a traditional iterative method for EIT reconstruction. The ANN demonstrated superior performance in terms of reconstruction accuracy and robustness to noise. While the GN algorithm was effective, it often produced artifacts and required extensive computational resources. In contrast, the ANN provided reconstructions with fewer artifacts and demonstrated faster evaluation times, indicating that the ANN can be a more efficient and reliable tool for EIT reconstructions, especially in scenarios where computational resources are limited. However, it is important

to note that while the ANN showed promise, its performance in real-world scenarios still needs further validation. The reliance on simulated data raises questions about the ANN's performance with real-world data, which may present unforeseen challenges. To address this, the ANN's performance was also evaluated using real-world data from a circular EIT tank and an experimental pig study. The tank data involved a saline solution and a pickle as the target, while the pig study used a clinical EIT device. The ANN demonstrated the ability to handle real-world complexities, but the results also highlighted the need for further refinement and validation. For example, the ANN was able to reconstruct the pickle's position and shape in the saline tank with a reasonable degree of accuracy. However, the reconstructions from the pig study exhibited greater variability, likely due to the more complex and less controlled environment. This variability suggests that while the ANN has potential, its robustness in diverse real-world conditions requires further investigation and improvement.

6.2 D-Bar Algorithm

6.2.1 4-Probe Measurements

The D-Bar algorithm was adapted to function with four-probe measurements, addressing the practical limitations of using two- and three-probe measurements. This adaptation involved the use of variational regularization to simulate a complete set of measurements, ensuring robust and accurate conductivity reconstructions. The results demonstrated that the D-Bar algorithm could effectively address the challenges associated with four-probe measurements, providing reliable reconstructions even in the presence of noise and hardware imperfections. This adaptation is significant as it enhances the practical applicability of the D-Bar algorithm in real-world scenarios. However, the complexity of implementing four-probe measurements in practice should not be underestimated. The process begins with acquiring adjacent four-probe measurements, which are then used to reconstruct an initial conductivity distribution via variational regularization. This initial distribution is not intended to be very accurate but to replicate the physical properties of the voltage measurements. This distribution is then used to simulate a full set of measurements, thereby circumventing the problematic two- and three-probe measurements. The simulated measurements are used to create the matrices necessary for the D-Bar reconstruction, which is then applied to achieve the final conductivity distribution. While this method ensures robust and accurate reconstructions, it requires sophisticated hardware capable of precise current injection and voltage measurement across multiple electrodes, which increases the complexity

and cost. Despite these challenges, the four-probe D-Bar algorithm offers a significant improvement in the robustness and accuracy of conductivity reconstructions, rendering it a valuable tool for real-world applications of EIT.

6.2.2 Absolute D-Bar

The feasibility of using the D-Bar algorithm as an absolute (time-independent) reconstruction technique was investigated. The construction of the DtN map from inhomogeneous measurements enabled the extension of the D-Bar algorithm to handle time-independent scenarios. This approach demonstrated the algorithm's versatility and potential for applications where dynamic changes are overall or irrelevant. The capacity to handle time-independent scenarios broadens the scope of the D-Bar algorithm in various medical and industrial applications. However, the assumption of small dynamic changes may restrict its applicability in more dynamic environments. The method entails the utilization of variational regularization to simulate a comprehensive set of measurements, thereby ensuring the generation of robust and accurate conductivity reconstructions. This adaptation is significant as it enhances the practical applicability of the D-Bar algorithm in real-world scenarios, providing reliable reconstructions even in the presence of noise and hardware imperfections. Nevertheless, the complexity of implementing this technique in practice should not be underestimated, as it requires sophisticated hardware capable of precise current injection and voltage measurement across multiple electrodes simultaneously.

6.2.3 Frequency-Differential Reconstruction

The D-Bar algorithm was also evaluated as a frequency differential reconstruction technique. By leveraging the frequency-dependent conductivity of tissues, the algorithm provided additional diagnostic information and enhanced contrast. This method involved comparing reconstructions at different frequencies, offering valuable insights into the frequency-dependent properties of tissues. This capability is particularly useful in medical diagnostics, where different tissue types exhibit distinct frequency-dependent behaviors. For example, tissues typically exhibit a frequency-dependent increase in conductivity, particularly in the β-dispersion range, due to the capacitive effects of cell membranes. By collecting the DtN map at both high and low frequencies, the D-Bar algorithm can visualize the conductivity differences between these frequencies, thus enhancing the contrast and providing additional diagnostic information. Nevertheless, the practical implementation of frequency differential reconstruction necessitates careful consideration of the frequency range and the associated hardware capabilities, as well as the necessity to address potential errors resulting from

modeling inaccuracies, noise, and hardware imperfections.

6.2.4 A-Priori Data Integration

The integration of a-priori data into the D-Bar algorithm was investigated with the objective of improving reconstruction quality. By incorporating additional information from other imaging modalities, such as radar data as an illustrative example, the algorithm demonstrated improved spatial resolution and reconstruction accuracy. This hybrid approach leveraged the strengths of both EIT and radar, making it a viable option for complex conductivity distributions. The integration of a-priori data represents a significant advancement in the field of EIT, as it allows for more accurate and detailed reconstructions. However, the dependency on additional data sources may complicate the overall system and increase the cost and complexity of the setup. The process involves using radar data to enhance the intermediate state of the D-Bar algorithm, which provides the ability to fuse additional data into the reconstruction. This method combines the advantages of EIT, which provides deeper penetration, with the higher spatial resolution of radar, resulting in a fused non-linear Fourier or scattering transform that significantly improves the quality of the final reconstruction. Despite these benefits, the practical implementation of this approach requires sophisticated hardware and careful calibration to ensure the accuracy and reliability of the integrated data sources. In conclusion, the research has demonstrated that both the ANN and the D-Bar algorithm have significant potential for improving EIT reconstructions. The ANN represents a robust and efficient alternative to traditional methods, capable of capturing complex nonlinear relationships and reducing noise susceptibility. It has shown promising results in various evaluations, including simulated data, noisy FEM data, tank data, and real pig data. Conversely, the D-Bar algorithm represents a versatile and powerful tool for direct reconstruction, particularly when enhanced with additional data and adapted for practical measurement techniques. The D-Bar algorithm's adaptations for four-probe measurements, time-independent reconstruction, frequency differential reconstruction, and integration of a-priori data have demonstrated the ability to enhance its robustness, accuracy, and practical applicability. These advancements address various challenges, including noise, hardware limitations, and the need for high spatial resolution. However, further validation with real-world patient data is required. The research underscores the transformative potential of these advanced algorithms in the field of EIT, paving the way for more accurate and reliable diagnostic tools in medical and industrial applications.

7 Conclusion and Outlook

Building on the insights gained from this research, several promising avenues for future development in EIT emerge. The constributions of this thesis to both ANN and D-Bar approaches have demonstrated significant potential for improving EIT reconstructions, particularly in scenarios where time is not a critical factor. However, as with any evolving technology, there remain challenges to overcome and opportunities to explore. The following sections present key areas for future research and development, each aimed at further enhancing the capabilities and applicability of EIT in both medical and industrial settings. These future directions leverage the strengths of the methods discussed earlier while addressing their current limitations, potentially opening new frontiers in non-invasive imaging and monitoring.

Fusion of other Modalities with EIT through ANNs

The fusion of other imaging modalities with EIT through ANNs represents a promising approach to enhance the spatial resolution and diagnostic capabilities of EIT. This fusion can be achieved at different levels, including early fusion (input-level), late fusion (decision-level), or intermediate fusion (feature-level). The process involves combining data from EIT with complementary modalities such as ultrasound, radar, MRI, or CT. ANNs can be designed to learn the optimal way to integrate these diverse data sources, leveraging the strengths of each modality while compensating for their individual limitations. Challenges include dealing with different spatial and temporal resolutions, aligning data from different modalities, and designing network architectures that can effectively process and combine multimodal inputs. Successful implementation could lead to more accurate and detailed reconstructions, potentially improving diagnostic accuracy in various medical applications.

ANN and 3D Imaging

The application of ANNs to three-dimensional EIT imaging presents both opportunities and challenges. The primary challenge lies in the increased dimensionality and complexity of three-dimensional data compared to two-dimensional reconstructions. The input representations for three-dimensional data require careful consideration, with potential options including voxel-based representations, point clouds, or multi-slice approaches. ANN architectures for 3D reconstruction may incorporate 3D convolutional layers, graph neural networks, or transformer-based models to effectively process spatial information in three dimensions. The increased computational demands of 3D reconstruction

necessitate efficient network designs and possibly the use of hardware acceleration. Despite these challenges, ANNs for 3D EIT have the potential to provide more comprehensive and accurate visualizations of complex anatomical structures, thereby improving diagnostic capabilities in applications like lung imaging or brain monitoring.

Frequency-differential EIT with D-Bar Optimization

Optimizing the D-Bar algorithm for frequency-differential EIT offers a pathway to improve reconstruction quality and stability. The traditional D-Bar method, which uses a circular scattering transform, can be adapted to incorporate frequency-differential data. This adaptation may involve modifying the scattering transform to account for measurements at multiple frequencies. Exploring alternative filter shapes beyond the circular one could potentially improve stability and resolution. The challenge lies in finding filter shapes that balance numerical stability with the ability to capture fine details in the reconstruction. Additionally, developing improved approximations for calculating the scattering transform in the frequency-differential case could enhance computational efficiency and accuracy. This optimized approach could lead to more robust reconstructions that better utilize the rich information provided by multi-frequency measurements.

Another way of is to incorporate complex valued measurement information into the reconstruction. This approach would leverage the capacitive nature of body cells and their frequency dependend ϵ-values. Next to the increased computational complexity a challenge in this approach is to get accurate measurements in the voltage phase a long the a broad frequency spectrum.

Uncertainty Estimation

Incorporating uncertainty estimation into EIT reconstruction is crucial for providing clinicians with reliable information for decision-making. This necessitates the quantification and visualization of the uncertainty inherent in the reconstructed images, which is of particular importance given the ill-posed nature of the EIT inverse problem. For ANNs, techniques such as Monte Carlo dropout, ensemble methods, or Bayesian neural networks can be employed to estimate uncertainty. In the context of D-Bar reconstructions, statistical approaches or perturbation methods might be used to assess the sensitivity of the reconstruction to measurement errors or model assumptions. One approach to visualizing uncertainty is to color-code reconstructed images or provide confidence intervals for conductivity values. Effective uncertainty estimation not

only improves the interpretability of EIT images but also helps to identify areas where the reconstruction might be less reliable, guiding further investigation or data collection.

Domain Shape aside from circular for ANN and D-Bar

Extending ANN and D-Bar methods to non-circular domain shapes is an important step towards more realistic and versatile EIT applications. Many real-world scenarios involve non-circular geometries, such as cross-sections of the human body. In order to extend ANNs to non-circular domain shapes, it is necessary to train on a diverse set of domain shapes and potentially incorporate shape information as an additional input. Techniques such as spatial transformer networks or deformable convolutions might be employed to handle varying geometries. In order to adapt the D-Bar algorithm to non-circular domains, it is necessary to modify the scattering transform and the D-Bar equation to account for the specific geometry. This could include developing new basis functions or coordinate transformations suitable for arbitrary shapes. Successfully addressing this challenge would greatly expand the applicability of EIT to a wider range of anatomical structures and industrial applications.

Validation on Animal and clinical Trials for the Algorithms

The trials should encompass a diverse range of subjects and conditions to assess the algorithms' robustness and generalizability. The key aspects to evaluate include image quality, diagnostic accuracy, reproducibility, and clinical relevance of the reconstructions. Comparison with established imaging modalities and current clinical standards is crucial. Additionally, the trials should address practical considerations such as ease of use, real-time performance, and integration with existing clinical workflows. Regulatory requirements and ethical considerations must be carefully navigated. Successful clinical validation would not only demonstrate the suitability of these advanced EIT algorithms but also pave the way for their adoption in routine clinical practice. This could potentially lead to improvements in patient care in areas such as lung monitoring, breast cancer detection, or neurological assessments.

This investigation of EIT has revealed promising advancements in both ANN and D-Bar approaches. However, challenges remain in areas such as 3D reconstruction and non-circular domains. As the field progresses, key priorities have been identified, including uncertainty estimation, the integration of multimodal imaging, and the conduction of rigorous clinical validation. Despite remaining challenges, it is anticipated that continued research and interdisciplinary

collaboration will facilitate the expansion of EIT capabilities and applications, potentially enhancing its role in both medical diagnostics and industrial monitoring.

A Appendix

A.1 D-Bar

$$
\begin{aligned}
-\boldsymbol{\Delta}\Psi(z,k) + q(z)\Psi(z,k) &= 0 \\
-\boldsymbol{\Delta}\mu(z,k)e^{jkz} + q(z)\mu(z,k)e^{jkz} &= 0 \\
-4\partial\overline{\partial}\mu(z,k)e^{jkz} + q(z)\mu(z,k)e^{jkz} &= 0 \\
-4\partial(\overline{\partial}\mu(z,k)e^{jkz} + q(z)\mu(z,k)e^{jkz} &= 0 \\
-4(\overline{\partial}\mu(z,k)jke^{jkz} + \partial\overline{\partial}\mu(z,k)e^{jkz}) + q(z)\mu(z,k)e^{jkz} &= 0 \\
e^{jkz}(-4\overline{\partial}\mu(z,k)jk - 4\partial\overline{\partial}\mu(z,k) + q(z)\mu(z,k)) &= 0 \\
-4\overline{\partial}\mu(z,k)jk - 4\partial\overline{\partial}\mu(z,k) + q(z)\mu(z,k) &= 0 \\
(-4\overline{\partial}jk - 4\partial\overline{\partial} + q(z)\mu(z,k))\mu(z,k) &= 0 \\
(-\boldsymbol{\Delta} - 4\overline{\partial}jk + q(z))\mu(z,k) &= 0 \qquad \text{(A.1)}
\end{aligned}
$$

A.2 The D-Bar Algorithm in pseudo Code

Input: Boundary voltages V, injected currents $\vec{\boldsymbol{J}}$
Output: Reconstructed conductivity map σ_{recon}
Step 1: Data Preparation & DtN Map
Compute DtN map $L_\sigma \leftarrow \text{DtN}(V, I, fmdl)$;
Step 2: Compute Scattering Transform
Define parameters $R \leftarrow 3.0$, $M \leftarrow 2^5$, $s \leftarrow 0.25$;
Compute grid spacing $h \leftarrow \frac{2R}{M-1}$;
Generate meshgrid $(K_x, K_y) \leftarrow \text{meshgrid}([-R : h : R])$;
Form complex grid $Q \leftarrow K_x + i\,K_y$;
Initialize $t^{\text{exp}} \leftarrow 0_{M\times M}$;
Mask indices $K_{\text{mask}} \leftarrow \{|Q| < R\}$;
Compute scattering $t^{\text{exp}}[K_{\text{mask}}] \leftarrow (\vec{\boldsymbol{J}}^T e^{i\bar{k}\bar{\boldsymbol{z}}_{el}})^T((\boldsymbol{L}_\sigma - \boldsymbol{L}_1)\vec{\boldsymbol{J}}^T e^{ik\boldsymbol{z}_{el}})$;
Compute Green's function $\bar{G} \leftarrow (\pi\bar{Q})^{-1}$ and smooth with radius R, factor s;
Precompute $\bar{G}_{\text{fft}} \leftarrow \text{FFT2}(\text{fftshift}(\bar{G}))$;
Step 3: Solve D–Bar Equation
Data: Reconstruction points Z, t^{exp}, $\bar{G}_{\text{fft}}$
Initialize $\mu_{\text{final}} \leftarrow \mathbf{1}_{|Z|}$;
foreach $z \in Z$ **do**
$T_R \leftarrow t^{\text{exp}} \odot \exp\big(-i\,(Q\,z + \bar{Q}\,\bar{z})\big)$;
Form RHS vector $b \leftarrow [\mathbf{1}_{|K_{\text{mask}}|};\, \mathbf{0}_{|K_{\text{mask}}|}]$;
Solve $(I + P)\mu = b$ via GMRES:
$\mu \leftarrow \text{GMRES}(\text{dbar_op}, b, T_R, \bar{G}_{\text{fft}})$;
Scatter μ onto grid: $\mu_{\text{grid}}[K_{\text{mask}}] \leftarrow \text{Re}(\mu) + i\ \text{Im}(\mu)$;
Interpolate at origin: $\mu_{\text{final}}[z] \leftarrow \mu_{\text{grid}}(0)$;
end
Step 4: Recover Conductivity
$\sigma_{\text{recon}} \leftarrow |\mu_{\text{final}}|^2$;
return σ_{recon};

Algorithm 1: D–Bar Reconstruction

A.3 The D-Bar Algorithm through the eye of Systems Engineering

System Model and Transfer Function Characterization

From a systems engineering perspective, the D-bar algorithm approaches EIT as a complex system identification problem. In this approach, an unknown distributed parameter system is characterized using only input-output measurements at the boundary. This approach is a paradigm shift from traditional optimization-based methods because it offers a direct reconstruction technique that uses complex analysis and nonlinear frequency domain processing.

The human body or the object under investigation can be conceptualized as a complex distributed parameter system, wherein the conductivity, $\sigma(x)$, represents the local system parameters at every spatial location, x. Unlike conventional lumped parameter systems with discrete components, this is a continuous medium in which electromagnetic properties vary smoothly throughout the spatial domain. The system's complete behavior is encapsulated by its DN map, which functions analogously to a transfer function in linear systems theory.

The DN map establishes a direct relationship between voltage patterns applied to boundary electrodes (Dirichlet boundary conditions) as inputs and current patterns measured at the same electrodes (Neumann boundary conditions) as outputs. The DN map Λ_σ essentially constitutes a multi-input, multi-output (MIMO) transfer function that encapsulates the internal medium's entire electromagnetic behavior as observed from boundary measurements. The mathematical elegance of this formulation lies in its ability to characterize the system's entire response without requiring knowledge of the internal conductivity distribution.

Nonlinear Frequency Domain Analysis via Scattering Transform

The core innovation of the D-bar method is treating the reconstruction as a nonlinear frequency-domain problem via the scattering transform, $t(k)$, which is a nonlinear analogue of the classical Fourier transform. The complex frequency parameter k plays a role similar to $j\omega$ in linear systems, and $t(k)$ provides a frequency-domain representation of internal conductivity variations. This transformation converts spatial domain conductivity variations into frequency domain scattering coefficients, enabling a more sophisticated analysis of the medium's spectral properties.

Each complex frequency k corresponds to a different "probing mode" that interrogates the medium. The scattering transform $t(k)$ quantifies how much

each frequency component is scattered or reflected by the conductivity variations. This interpretation provides intuitive insight into the reconstruction process: different frequency components reveal different spatial scales of the conductivity distribution. This is similar to how different frequencies in conventional Fourier analysis reveal different temporal characteristics of signals.

Complex Geometric Optics Solutions as System Excitation

The CGO solutions, denoted by the symbol $\psi(x, k)$, serve as specialized excitation signals for system identification. They function as carefully constructed complex exponentials that uniformly penetrate the entire domain while maintaining well-defined propagation characteristics. These solutions are mathematically precise constructs, not arbitrary test signals, that allow for the separation of incident and scattered components. This enables a robust analysis of the medium's response.

Each CGO solution represents a complex wave that propagates through the medium with a wave vector k. The medium's inhomogeneities scatter this wave in a manner that encodes information about the medium's internal structure. The mathematical formulation ensures these solutions satisfy the Schrödinger equation, $-(-\Delta+q)\psi = 0$, while exhibiting the necessary asymptotic behavior for reconstruction.

System Identification via Boundary Integral Equations

The fundamental challenge in computing CGO solutions is the paradox that we need these solutions to compute the scattering transform, but the solutions depend on the unknown conductivity that we are trying to determine. The D-bar method resolves this issue with an elegant boundary integral equation (BIE) approach that performs boundary system identification using only the measured DN map.

The BIE for the CGO solutions takes the form:

$$\psi(z, k) = e^{ikz} - \int_{\partial\Omega} G_k(z - \zeta)(\Lambda_\sigma - \Lambda_1)\psi(\zeta, k)\, ds$$

. This self-consistency equation expresses the boundary values of the CGO solutions as functions of the solutions themselves and the measured boundary data. This transforms the problem into a linear algebra system for each frequency k. This approach is analogous to output-only system identification, in which system characteristics are determined from boundary measurements alone, without requiring knowledge of the internal field.

Inverse Filtering and Reconstruction Process

Once the scattering transform, t(k), is obtained, the D-bar equation performs inverse filtering to recover the conductivity in the spatial domain. This process functions like an inverse Fourier transform. The D-bar equation is expressed as follows: $\frac{\partial}{\partial \bar{k}}\mu(z,k) = \frac{1}{4\pi k}t(k)e^{-ik(z-\bar{z})}\overline{\mu(z,k)}$, converts frequency-domain scattering data back to spatial-domain conductivity information.

The reconstruction process operates on a point-by-point basis. The algorithm solves for conductivity at each spatial location independently through the relationship $\sigma(z) = |\lim_{|k|\to\infty}\mu(z,k)|^2$. This direct reconstruction approach avoids the local minimum problems inherent in iterative optimization methods and provides computational advantages for real-time applications.

Regularization as Spectral Noise Filtering

Like many inverse problems, EIT reconstruction is severely ill-posed, meaning small measurement errors can cause large reconstruction errors. The standard regularization approach uses frequency-domain filtering, which highlights the high-frequency components of $t(k)$ that are most sensitive to noise. A sharp cutoff filter is applied such that $t(k) = 0$ for $|k| > R$, where R is the cutoff radius and a carefully chosen parameter.

This filtering strategy acts as a low-pass filter in the scattering transform domain, creating the classic engineering tradeoff between noise rejection and spatial resolution. A smaller cutoff radius R provides better noise immunity but lower resolution, while a larger R achieves higher resolution at the cost of increased noise sensitivity. Compared to iterative methods, this regularization approach provides predictable noise behavior and stable reconstruction characteristics.

Implementation Pipeline and Computational Considerations

The D-bar algorithm uses a four-stage signal processing pipeline to systematically transform boundary measurements into conductivity reconstructions. During the data acquisition stage, the DN map Λ_σ, denoted by the symbol σ, is computed from the electrode measurements using matrix operations on the measured voltage and current data. The system identification stage solves boundary integral equations to find CGO solutions on the boundary. This stage typically employs iterative methods, such as GMRES, for linear systems.

The transform stage computes the scattering transform $t(k)$ within the specified frequency band $|k| \leq R$ via numerical integration of the frequency domain. Finally, the inverse filtering stage solves the D-bar equation to recover the conductivity, $\sigma(x)$, at each spatial point by solving integral equations.

A.4 Peer-reviewed Journal Articles

1. **J. Rixen**, B. Eliasson, B. Hentze, T. Muders, C. Putensen, S. Leonhardt, and C. Ngo: "A Rotational Invariant Neural Network for Electrical Impedance Tomography Imaging without Reference Voltage: RF-REIM-NET". *Diagnostics*, 12:777, 2022.

2. S. Lyra, **J. Rixen**, K. Heimann, S. Karthik, and J. Jayaraj: "Camera fusion for real-time temperature monitoring of neonates using deep learning". *Medical & Biological Engineering & Computing*, 2022:2561-9, 2022.

3. L. Korn, S. Dual, **J. Rixen**, M. Meboldt, S. Leonhardt, and T. Schmitz-Rode: "Dual-Modality Volume Measurement Integrated on a Ventricular Assist Device". *IEEE Transactions on Biomedical Engineering*, 2022:3115019, 2022.

4. **J. Rixen**, N. Blass, S. Lyra, and S. Leonhardt: "The D-Bar Algorithm Fusing Electrical Impedance Tomography with A Priori Radar Data: A Hands-On Analysis". *Algorithms*, 16:43, 2023.

5. F. Voss, N. Brechmann, S. Lyra, **J. Rixen**, and S. Leonhardt: "Multimodal body part segmentation of infants using deep learning". *BioMedical Engineering OnLine*, 22:28, 2023.

6. S. Lyra, A. Mustafa, **J. Rixen**, S. Borik, M. Lueken, and S. Leonhardt: "Conditional Generative Adversarial Networks for Data Augmentation of a Neonatal Image Dataset". *Sensors*, 23:20999, 2023.

7. **J. Rixen**, N. Blass, S. Lyra, and S. Leonhardt: "Comparison of Machine Learning Classifiers for the Detection of Breast Cancer in an Electrical Impedance Tomography Setup". *Algorithms*, 16:517, 2023.

A.5 Conference Proceedings

1. **J. Rixen**, B. Hentze: "Neural Network to improve Electrical Impedance Tomography Reconstructions using the GREIT Algorithm". *24th International Student Conference on Electrical Engineering.* Prague, Czech Republic, 2020.

2. Duy Hai Nguyen, Jochen Moll, Viktor Krozer, Vittorio Memmolo, **Jöran Rixen**, and Gernot Zimmer: "Elliptical monopole antenna design for the

early breast cancer imaging at high frequencies". *15th European Conference on Antennas and Propagation (EuCAP)*. Online, 2021.

3. **J. Rixen**, S. Leonhardt and C. Ngo: "A systematic analysis of an a priori D-Bar EIT algorithm using the GREIT figures of merit". *21st International Conference on Biomedical Applications of Electrical Impedance Tomography (EIT 2021)*. Online, 2021.

4. **J. Rixen**, B. Hentze, S. Leonhardt and C. Hoog-Antink: "Reconstruction Improvement of Electrical Impedance Tomography, through a Convolutional Neural Network". *IUPESM World Congress on Medical Physics and Biomedical Engineering*. Singapore, 2022.

5. **J. Rixen**, N. Blass, S. Lyra, and S. Leonhardt: "Comparison of Machine Learning classifiers for the detection of breast cancer in an Electrical Impedance Tomography setup". *23rd International Conference on Biomedical Applications of Electrical Impedance Tomography*. Aachen, Germany, 2023.

6. **J. Rixen**, B. Eliasson, S. Lyra, and S. Leonhardt: "Shape analysis of training data for neural networks in Electrical Impedance Tomography". *45th Annual International Conference of the IEEE Engineering in Medicine and Biology Society*. Sydney, Australia, 2023.

A.6 Supervised Student Theses

1. D. Lyubomirov: *Deep learning for reconstruction in electrical impedance tomography.* Master's thesis, 2020.

2. J. Keup: *Entwicklung eines Algorithmus zur automatischen Bestimmung von Mess- und Einspeisemustern in der Elektrischen Impedanz Tomographie.* Master's thesis, 2020.

3. M. Semmler: *Erstellung eines physischen Brustgewebephantoms.* Bachelor's thesis, 2020.

4. N. Khatib: *Creation Of A Physical Breast Tissue Phantom.* Bachelor's thesis, 2020.

5. E. Ponjavic: *Comparison of Conventional Electrodes and Distributed Electrode Arrays for Electrical Impedance Tomography.* Bachelor's thesis, 2021.

6. N. Blass: *Vergleich von Machine Learning Algorithmen für das Aufspüren von Brustkrebs in der elektrischen Impedanz Tomographie.* Bachelor's thesis, 2021.

7. M. I. Lerma Garro: *Creation of a physical breast tissue phantom for cancer with electrical impedance tomography.* Master's thesis, 2021.

8. J. Müller: *Algorithm-based improvement of spatial resolution in electrical impedance tomography.* Master's thesis, 2021.

9. B. Eliasson: *Machine-Learning-reconstruction- algorithms for reconstruction in electrical impedance-tomography.* Master's thesis, 2021.

10. X. Lu: *Comparison of different hyper-parameter selection algorithms for frequency differential EIT.* Master's thesis, 2021.

11. K. Alde: *Verbesserung eines Machine-Learning- Rekonstruktionsverfahrens für die Elektrische Impedanz-Tomographie.* Master's thesis, 2022.

12. N. Kumar: *A deep learning approach for the complex D-bar algorithm for the electrical impedance tomography.* Master's thesis, 2022.

13. F. Dahms: *Neural Networks in Electrical Impedance Tomography: An Analysis of Noise.* Bachelor's thesis, 2022.

14. N. Meyer: *Analyse von Trainingsdaten für künstliche Neuronale Netze in der Elektrischen Impedanz Tomographie.* Bachelor's thesis, 2022.

15. A. Shariati Qalehnou (Jannatabadi): *Aufbau eines neuronalen Netzes für die frequenzdifferentielle elektrische Impedanztomographie.* Master's thesis, 2023.

16. N. Blass: *Development of a Real-Time Pipeline for Deep Learning-Based Vital Signs Extraction in Preterm Infants.* Master's thesis, 2023.

Bibliography

[AAB+09] A. Adler, J. H. Arnold, R. Bayford, A. Borsic, B. Brown, P. Dixon, T. J. Faes, I. Frerichs, H. Gagnon, Y. Gärber, *et al.*: "Greit: a unified approach to 2d linear eit reconstruction of lung images". *Physiological measurement*, 30(6):S35, 2009.

[AAB+15] M. Abadi, A. Agarwal, P. Barham, E. Brevdo, Z. Chen, C. Citro, G. S. Corrado, A. Davis, J. Dean, M. Devin, S. Ghemawat, I. Goodfellow, A. Harp, G. Irving, M. Isard, Y. Jia, R. Jozefowicz, L. Kaiser, M. Kudlur, J. Levenberg, D. Mané, R. Monga, S. Moore, D. Murray, C. Olah, M. Schuster, J. Shlens, B. Steiner, I. Sutskever, K. Talwar, P. Tucker, V. Vanhoucke, V. Vasudevan, F. Viégas, O. Vinyals, P. Warden, M. Wattenberg, M. Wicke, Y. Yu, and X. Zheng: "TensorFlow: Large-scale machine learning on heterogeneous systems", 2015. Software available from tensorflow.org.
URL `https://www.tensorflow.org/`

[AC14] C. Araújo and W. Celes: "Quadrilateral mesh generation with deferred constraint insertion". *Procedia Engineering*, 82:88–100, 2014.

[AGM11] A. Adler, P. O. Gaggero, and Y. Maimaitijiang: "Adjacent stimulation and measurement patterns considered harmful". *Physiological measurement*, 32(7):731, 2011.

[AL06] A. Adler and W. R. Lionheart: "Uses and abuses of eidors: an extensible software base for eit". *Physiological measurement*, 27(5):S25, 2006.

[AM18] M. Alsaker and J. L. Mueller: "Use of an optimized spatial prior in d-bar reconstructions of eit tank data". *Inverse Problems & Imaging*, 12(4):883, 2018.

[ARP+23] K. Ain, O. N. Rahma, A. P. Putra, N. Syavinas, D. Darmawan, and H. Sohal: "Bone fracture detection using electrical impedance tomography based on stemlab red pitaya". *Indonesian Journal of Electrical Engineering and Computer Science*, 32(1):150–159, 2023.

[ATY+18] M. Z. Alom, T. M. Taha, C. Yakopcic, S. Westberg, P. Sidike, M. S. Nasrin, B. C. Van Esesn, A. A. S. Awwal, and V. K.

Asari: "The history began from alexnet: A comprehensive survey on deep learning approaches". *arXiv preprint arXiv:1803.01164*, 2018.

[BCJ+17] A. Boyle, M. Crabb, M. Jehl, W. Lionheart, and A. Adler: "Methods for calculating the electrode position jacobian for impedance imaging". *Physiological measurement*, 38(3):555, 2017.

[BGAL09] A. Borsic, B. M. Graham, A. Adler, and W. R. Lionheart: "In vivo impedance imaging with total variation regularization". *IEEE transactions on medical imaging*, 29(1):44–54, 2009.

[Boy16] A. J. S. Boyle: *Geophysical applications of electrical impedance tomography*. Ph.D. thesis, Carleton University, 2016.

[BSF94] Y. Bengio, P. Simard, and P. Frasconi: "Learning long-term dependencies with gradient descent is difficult". *IEEE transactions on neural networks*, 5(2):157–166, 1994.

[Cal80] A. P. Calderón: "On an inverse boundary value problem". *Seminar on Numerical Analysis and its Applications to Continuum Physics*, 65–73. Sociedade Brasileira de Matemática, Rio de Janeiro, 1980.

[CC41] K. S. Cole and R. H. Cole: "Dispersion and absorption in dielectrics i. alternating current characteristics". *The Journal of chemical physics*, 9(4):341–351, 1941.

[CFG+19] A. Carrier, F. Fischanger, J. Gance, G. Cocchiararo, G. Morelli, and M. Lupi: "Deep electrical resistivity tomography for the prospection of low-to medium-enthalpy geothermal resources". *Geophysical journal international*, 219(3):2056–2072, 2019.

[CFPH23] C. J. Cameron, B. C. Fortune, C. G. Pretty, and M. P. Hayes: "Electrode-skin impedance model parameter estimation in the frequency-domain". *Biomedical Signal Processing and Control*, 63:102202, 2023.

[CHS+21] C.-C. Chang, Z.-Y. Huang, S.-F. Shih, Y. Luo, A. Ko, Q. Cui, J. Sumner, S. Cavallero, S. Das, W. Gao, *et al.*: "Electrical impedance tomography for non-invasive identification of fatty liver infiltrate in overweight individuals". *Scientific reports*, 11(1):19859, 2021.

[CLSR+19] D. D. Corona-Lopez, S. Sommer, S. A. Rolfe, F. Podd, and B. D. Grieve: "Electrical impedance tomography as a tool for phenotyping plant roots". *Plant methods*, 15:1–15, 2019.

[Dan22] S. Danilov: "On the resolution of triangular meshes". *Journal of Advances in Modeling Earth Systems*, 14(10):e2022MS003177, 2022.

[DBD+21] C. Dang, C. Bellis, M. Darnajou, G. Ricciardi, S. Mylvaganam, and S. Bourennane: "Practical comparisons of eit excitation protocols with applications in high-contrast imaging". *Measurement Science and Technology*, 32(8):085110, 2021.

[DM14] M. Dodd and J. L. Mueller: "A real-time d-bar algorithm for 2-d electrical impedance tomography data". *Inverse problems and imaging (Springfield, Mo.)*, 8(4):1013, 2014.

[DRMS08] D. Dean, T. Ramanathan, D. Machado, and R. Sundararajan: "Electrical impedance spectroscopy study of biological tissues". *Journal of electrostatics*, 66(3-4):165–177, 2008.

[EKN+17] A. Esteva, B. Kuprel, R. A. Novoa, J. Ko, S. M. Swetter, H. M. Blau, and S. Thrun: "Dermatologist-level classification of skin cancer with deep neural networks". *Nature*, 542(7639):115 – 118, 2017.

[FR97] A. Frangi and J. Rosell: "A theoretical analysis of noise in electrical impedance tomographic images". *Proceedings of the 19th Annual International Conference of the IEEE Engineering in Medicine and Biology Society.'Magnificent Milestones and Emerging Opportunities in Medical Engineering'(Cat. No. 97CH36136)*, vol. 1, 433–436. IEEE, 1997.

[GAD+18] N. Goren, J. Avery, T. Dowrick, E. Mackle, A. Witkowska-Wrobel, D. Werring, and D. Holder: "Multi-frequency electrical impedance tomography and neuroimaging data in stroke patients". *Scientific data*, 5(1):1–10, 2018.

[GLG96] S. Gabriel, R. Lau, and C. Gabriel: "The dielectric properties of biological tissues: Iii. parametric models for the dielectric spectrum of tissues". *Physics in medicine & biology*, 41(11):2271, 1996.

[GMT90] F. Grasso, F. Musumeci, and A. Triglia: "Impedance spectroscopy of pure water in the 0.01 hz to 100 khz range". *Il Nuovo Cimento D*, 12:1117–1130, 1990.

[HA22] D. Holder and A. Adler: "Electrical impedance tomography: methods, history and applications". *Taylor & Francis eBooks DRM Free Collection*, 2022.

[Had02] J. Hadamard: "Sur les problèmes aux dérivées partielles et leur signification physique". *Princeton University Bulletin*, 49–52, 1902.

[HH18] S. J. Hamilton and A. Hauptmann: "Deep d-bar: Real-time electrical impedance tomography imaging with deep neural networks". *IEEE transactions on medical imaging*, 37(10):2367–2377, 2018.

[HLY19] D. Hu, K. Lu, and Y. Yang: "Image reconstruction for electrical impedance tomography based on spatial invariant feature maps and convolutional neural network". *2019 IEEE International Conference on Imaging Systems and Techniques (IST)*, 1–6. IEEE, 2019.

[HMA17] S. J. Hamilton, J. L. Mueller, and M. Alsaker: "Incorporating a spatial prior into nonlinear d-bar eit imaging for complex admittivities". *IEEE Transactions on Medical Imaging*, 36(2):457–466, 2017.

[HT13] B. Haberman and D. Tataru: "Uniqueness in calderón's problem with lipschitz conductivities". *Duke Math. J.*, 162(3):497–516, 2013.

[HVML14] C. N. Herrera, M. F. Vallejo, J. L. Mueller, and R. G. Lima: "Direct 2-d reconstructions of conductivity and permittivity from eit data on a human chest". *IEEE transactions on medical imaging*, 34(1):267–274, 2014.

[HW59] D. H. Hubel and T. N. Wiesel: "Receptive fields of single neurones in the cat's striate cortex". *The Journal of physiology*, 148(3):574 – 591, 1959.

[HW78] R. P. Henderson and J. G. Webster: "An impedance camera for spatially specific measurements of the thorax". *IEEE Transactions on Biomedical Engineering*, (3):250–254, 1978.

[HZRS15a] K. He, X. Zhang, S. Ren, and J. Sun: "Delving deep into rectifiers: Surpassing human-level performance on imagenet classification". 1026 – 1034, 2015.

[HZRS15b] K. He, X. Zhang, S. Ren, and J. Sun: "Delving deep into rectifiers: Surpassing human-level performance on imagenet classification". *arXiv preprint arXiv:1502.01852*, 2015.

[IGBY05] I. Ismail, J. Gamio, S. A. Bukhari, and W. Yang: "Tomography for multi-phase flow measurement in the oil industry". *Flow measurement and instrumentation*, 16(2-3):145–155, 2005.

[IMNS04] D. Isaacson, J. L. Mueller, J. C. Newell, and S. Siltanen: "Reconstructions of chest phantoms by the d-bar method for electrical impedance tomography". *IEEE Transactions on Medical Imaging*, 23(7):821–828, 2004.

[Ino18] H. Inoue: "Data augmentation by pairing samples for images classification". *arXiv preprint arXiv:1801.02929*, 2018.

[KB14a] D. P. Kingma and J. Ba: "Adam: A method for stochastic optimization". *arXiv preprint arXiv:1412.6980*, 2014.

[KB14b] D. P. Kingma and J. Ba: "Adam: A method for stochastic optimization". *arXiv preprint arXiv:1412.6980*, 2014.

[KHH+22] X.-Y. Ke, W. Hou, Q. Huang, X. Hou, X.-Y. Bao, W.-X. Kong, C.-X. Li, Y.-Q. Qiu, S.-Y. Hu, and L.-H. Dong: "Advances in electrical impedance tomography-based brain imaging". *Military Medical Research*, 9(1):10, 2022.

[KHVS15] Á. Kertész, Z. Hlavacova, E. Vozáry, and L. Staronova: "Relationship between moisture content and electrical impedance of carrot slices during drying". *International Agrophysics*, 29(1), 2015.

[KKSV00] J. P. Kaipio, V. Kolehmainen, E. Somersalo, and M. Vauhkonen: "Statistical inversion and monte carlo sampling methods in electrical impedance tomography". *Inverse problems*, 16(5):1487, 2000.

[KR17] G. Kłosowski and T. Rymarczyk: "Using neural networks and deep learning algorithms in electrical impedance tomography". *Informatyka, Automatyka, Pomiary w Gospodarce i Ochronie Środowiska*, 7(3):99–102, 2017.

[KVKK97] V. Kolehmainen, M. Vauhkonen, P. Karjalainen, and J. Kaipio: "Assessment of errors in static electrical impedance tomography with adjacent and trigonometric current patterns". *Physiological measurement*, 18(4):289, 1997.

[Lar07] J. Larsson: "Electromagnetics from a quasistatic perspective". *American Journal of Physics*, 75(3):230–239, 2007.

[LBBH98] Y. LeCun, L. Bottou, Y. Bengio, and P. Haffner: "Gradient-based learning applied to document recognition". *Proceedings of the IEEE*, 86(11):2278 – 2324, 1998.

[LCS+18] D. Leonhäuser, C. Castelar, T. Schlebusch, M. Rohm, R. Rupp, S. Leonhardt, M. Walter, and J. O. Grosse: "Evaluation of electrical impedance tomography for determination of urinary bladder volume: comparison with standard ultrasound methods in healthy volunteers". *Biomedical engineering online*, 17:1–13, 2018.

[Leh18] G. Lehner: *Elektromagnetische Feldtheorie*. Springer Berlin Heidelberg, 9th ed., 2018.

[Lo14] D. S. Lo: *Finite element mesh generation*. CRC press, 2014.

[MGGM18] M. Mallach, M. Gevers, P. Gebhardt, and T. Musch: "Fast and precise soft-field electromagnetic tomography systems for multiphase flow imaging". *Energies*, 11(5):1199, 2018.

[MM09] E. K. Murphy and J. L. Mueller: "Effect of domain shape modeling and measurement errors on the 2-d d-bar method for eit". *IEEE transactions on medical imaging*, 28(10):1576–1584, 2009.

[MP43] W. S. McCulloch and W. Pitts: "A logical calculus of the ideas immanent in nervous activity". *The bulletin of mathematical biophysics*, 5(4):115 – 133, 1943.

[MPB+16] A. Martellosio, M. Pasian, M. Bozzi, L. Perregrini, A. Mazzanti, F. Svelto, P. E. Summers, G. Renne, L. Preda, and M. Bellomi: "Dielectric properties characterization from 0.5 to 50 ghz of breast cancer tissues". *IEEE Transactions on Microwave Theory and Techniques*, 65(3):998–1011, 2016.

[MS12] J. L. Mueller and S. Siltanen: *Linear and nonlinear inverse problems with practical applications*. SIAM, 2012.

[Nac96] A. I. Nachman: "Global uniqueness for a two-dimensional inverse boundary value problem". *Annals of Mathematics*, 143(1):71–96, 1996.

[NMK+21] D. H. Nguyen, J. Moll, V. Krozer, V. Memmolo, J. Rixenz, and G. Zimmer: "Elliptical monopole antenna design for the early breast cancer imaging at high frequencies". *2021 15th European Conference on Antennas and Propagation (EuCAP)*, 1–4. IEEE, 2021.

[NW90] D. Nguyen and B. Widrow: "Improving the learning speed of 2-layer neural networks by choosing initial values of the adaptive weights". *Neural Networks, 1990., 1990 IJCNN International Joint Conference on*, 21–26. IEEE, 1990.

[ÖK18] Ö. Özgün and M. Kuzuoğlu: *MATLAB-based finite element programming in electromagnetic modeling*. CRC Press, 2018.

[PAM+23] F. Pennati, A. Angelucci, L. Morelli, S. Bardini, E. Barzanti, F. Cavallini, A. Conelli, G. Di Federico, C. Paganelli, and A. Aliverti: "Electrical impedance tomography: from the traditional design to the novel frontier of wearables". *Sensors*, 23(3):1182, 2023.

[PD84] T. Porter and T. Duff: "Compositing digital images". *Proceedings of the 11th annual conference on Computer graphics and interactive techniques*, 253–259, 1984.

[PMK+20] M. V. Prati, J. Moll, C. Kexel, D. H. Nguyen, A. Santra, A. Aliverti, V. Krozer, and V. Issakov: "Breast cancer imaging using a 24 ghz ultra-wideband mimo fmcw radar: System considerations and first imaging results". *2020 14th European Conference on Antennas and Propagation (EuCAP)*, 1–5. IEEE, 2020.

[R+23] J. Rixen *et al.*: "EIDORS: D-bar algorithm implementation for electrical impedance tomography". `https://eidors3d.sourceforge.net/doc/index.html?eidors/solvers/inverse/inv_solve_d_bar.html`, 2023. Accessed June 12, 2025.

[REH+22] J. Rixen, B. Eliasson, B. Hentze, T. Muders, C. Putensen, S. Leonhardt, and C. Ngo: "A rotational invariant neural network for electrical impedance tomography imaging without reference voltage: Rf-reim-net". *Diagnostics*, 12(4):777, 2022.

[RGMK+22] Z. Rezanejad Gatabi, M. Mirhoseini, N. Khajeali, I. Rezanezhad Gatabi, M. Dabbaghianamiri, and S. Dorri: "The accuracy of electrical impedance tomography for breast cancer detection: A systematic review and meta-analysis". *The Breast Journal*, 2022(1):8565490, 2022.

[RLM+23] J. Rixen, S. Leonhardt, J. Moll, D. H. Nguyen, and C. Ngo: "The d-bar algorithm fusing electrical impedance tomography with a priori radar data: A hands-on analysis". *Algorithms*, 16(1):43, 2023.

[Sch97] J. Sch"oberl: "Netgen an advancing front 2d/3d-mesh generator based on abstract rules". *Computing and visualization in science*, 1(1):41–52, 1997.

[SHK+14] N. Srivastava, G. Hinton, A. Krizhevsky, I. Sutskever, and R. Salakhutdinov: "Dropout: A simple way to prevent neural networks from overfitting". *Journal of Machine Learning 15*, 2014.

[SJAH91] G. Scott, M. Joy, R. Armstrong, and R. Henkelman: "Measurement of nonuniform current density by magnetic resonance". *IEEE transactions on medical imaging*, 10(3):362–374, 1991.

[SNLW14] T. Schlebusch, S. Nienke, S. Leonhardt, and M. Walter: "Bladder volume estimation from electrical impedance tomography". *Physiological measurement*, 35(9):1813, 2014.

[SSS+17] D. Silver, J. Schrittwieser, K. Simonyan, I. Antonoglou, A. Huang, A. Guez, T. Hubert, L. Baker, M. Lai, A. Bolton, *et al.*: "Mastering the game of go without human knowledge". *Nature*, 550(7676):354, 2017.

[SU87] J. Sylvester and G. Uhlmann: "A global uniqueness theorem for an inverse boundary value problem". *Annals of mathematics*, 153–169, 1987.

[SWW+21] Y. Shi, Y. Wu, M. Wang, Z. Tian, X. Kong, and X. He: "Sparse image reconstruction of intracerebral hemorrhage with electrical impedance tomography". *Journal of Medical Imaging*, 8(1):014501–014501, 2021.

[TC19] V. Tomicic and R. Cornejo: "Lung monitoring with electrical impedance tomography: technical considerations and clinical applications". *Journal of thoracic disease*, 11(7):3122, 2019.

[VVK+98] M. Vauhkonen, D. Vadász, P. A. Karjalainen, E. Somersalo, and J. P. Kaipio: "Tikhonov regularization and prior information in electrical impedance tomography". *IEEE transactions on medical imaging*, 17(2):285–293, 1998.

[YC00] J. Y. Yam and T. W. Chow: "A weight initialization method for improving training speed in feedforward neural network". *Neurocomputing*, 30(1-4):219 – 232, 2000.

[YDX+17] L. Yang, M. Dai, C. Xu, G. Zhang, W. Li, F. Fu, X. Shi, and X. Dong: "The frequency spectral properties of electrode-skin contact impedance on human head and its frequency-dependent effects on frequency-difference eit in stroke detection from 10hz to 1mhz". *PLoS ONE*, 12, 2017.

[YGZ+22] L. Yang, L. Gan, Z. Zhang, Z. Zhang, H. Yang, Y. Zhang, and J. Wu: "Insight into the contact impedance between the electrode and the skin surface for electrophysical recordings". *ACS Omega*, 7(14):13906–13912, 2022.

[YWT87] T. J. Yorkey, J. G. Webster, and W. J. Tompkins: "Comparing reconstruction algorithms for electrical impedance tomography". *IEEE Transactions on Biomedical Engineering*, (11):843–852, 1987.

[ZCDLP17] H. Zhang, M. Cisse, Y. N. Dauphin, and D. Lopez-Paz: "mixup: Beyond empirical risk minimization". *arXiv preprint arXiv:1710.09412*, 2017.

[ZMC+22] S. Zhao, Y. Miao, R. Chai, J. Zhao, Y. Bai, Z. Wei, and S. Ren: "High-precision electrical impedance tomography for electrical conductivity of metallic materials". *Advances in Materials Science and Engineering*, 2022(1):3611691, 2022.